A method for measuring the 12C(p,n)12N cross section

Msc. Physics Thesis

by Floris Drent

First examiner:
Peter Dendooven
Second examiner:
Emiel van der Graaf

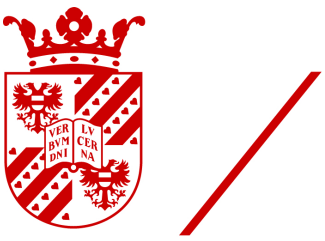

university of groningen

Rijksuniversiteit Groningen
The Netherlands
August 2021

Abstract

This master thesis is about the detection of ^{12}N in graphite through gamma spectroscopy focused on emitted gammas of 4.4 MeV. The graphite of 5.4 mm thick was irradiated with a pencil proton beam of 90 MeV. The goal of this work is to provide a start to the development of in-vivo dose verification for proton therapy at PARTREC, Groningen. The next step will be the measurement of the cross section of the reaction ^{12}C(p,n)^{12}N at high proton energies. This thesis suggests improvements for the detector setup based upon the difficulties encountered during the project. This thesis also provides a starting guide to performing gamma spectroscopy, especially with a cyclotron high-energy ion beam, as performed here at PARTREC.

Special mention

First above all, an incredible thank you to the supervisor of this thesis, Peter Dendooven. This master project was never intended as a project at all, but it is his actual own research and he had to teach me all about the process happening during his work. For his mentorship and patience, I am immensely grateful. Futhermore a thank you to Harry Kiewiet and Marc-Jan van Goethem for their technical support, Emiel van der Graaf for his work as second supervisor and the support and cleaning staff at the PARTREC facility. Of course I am also grateful for my family and friends for being who they are.

Contents

Chapter 1

Introduction

1.1 Proton therapy

Proton therapy is a radiation treatment method to irradiate cancerous tumors. The method uses high energy protons emitted upon the tumor to destroy its tissue. The more conventional radiotherapy counterpart uses high energy photons, X-ray or gamma rays, to irradiate tumors. However, radiotherapy also gives the surrounding healthy tissue a significant energy dose, causing 'collatoral damage'. Proton therapy negates that problem by being able to deposit the maximum dose in one location within the patient, the dose being the amount of deposited energy per kilogram of material. This precise deposition is possible due to a phenomenon called the *Bragg peak*. See figure1.1 for a sketch of the Bragg peak. When a charged particle moves through a medium, it loses energy to the medium as it travels. The loss of energy per distance travelled of the particle is called the *stopping power*. This stopping power increases as the particle moves slower, leading to a peak in stopping power and a near-instant drop to zero as the protons stop moving. This peak is the Bragg peak. The goal of proton therapy is to aim the location of the Bragg peak for protons on the tumor tissue. This ensures that the tumor tissue obtains a destructive dose from the proton beam while the surrounding, healthy tissue is spared. This makes proton therapy ideal for irradiating tumors near vital parts of the body, for example near the brain, heart or eyes. However, a major problem currently with proton therapy is the uncertainty in the Bragg peak location, or proton beam range, inside the patient during radiation. The reasons behind this uncertainty are:

- A CT-scan is created of the patient before undergoing proton radiation. The CT-scan is converted into a radiation treatment plan. This conversion contains inaccuracies.
- The therapy takes several days with multiple radiations. The anatomical structure of the patient can shift during these days due to, for example, change in weight or shrinkage of the tumor.
- The position of the patient can be off due to the patient moving.[1]

A general error margin for the proton beam range is 2 mm plus 3.5% of the beam range in the patient. [2] So for example, a to-be-radiated tumor is 3cm deep into the body of a patient. With this general error margin, an extra proton beam range of 3 mm is taken during treatment. This could cause damage to vital tissue of the patient. Naturally, the taken error margin also depends on the treatment centre, the location of the tumor and the surrounding tissue. If this overshooting in proton beam is not applied, undershooting can occur, whereby part of the tumor tissue could be spared a destructive radiation dose.

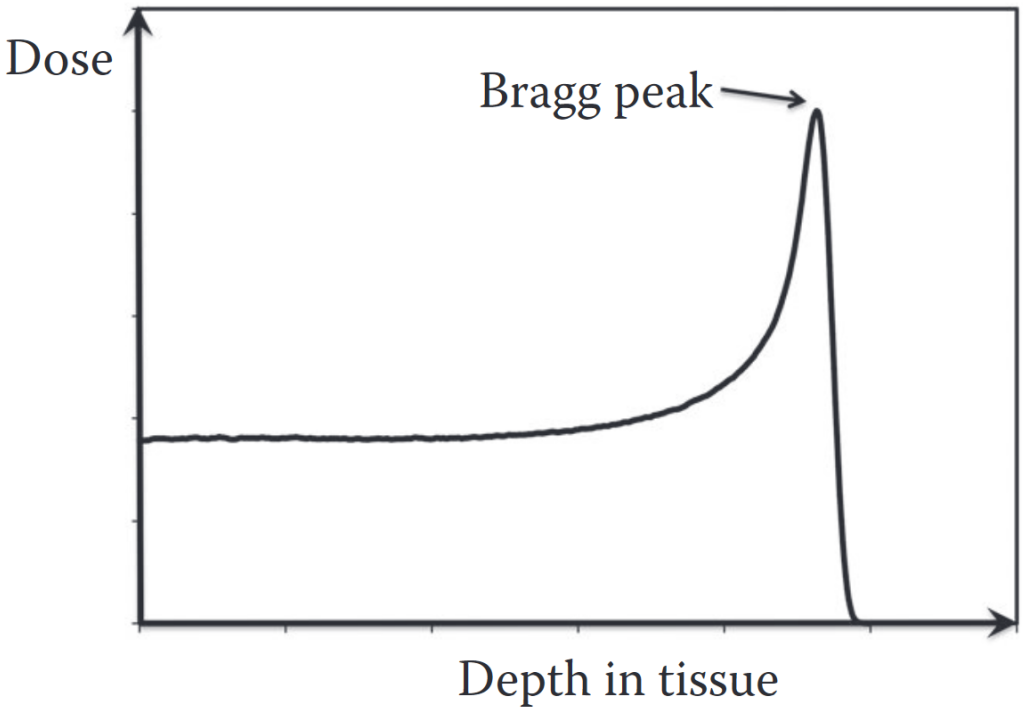

Figure 1.1: Sketch of the Bragg peak in proton therapy. The protons in a beam travel through the tissue depositing throughout their trajectory. At some point, the protons will annihilate whereby the energy deposition per unit length will increase and the Bragg peak occurs. Since the energy dose delivery before the Bragg peak is significantly smaller and behind the Bragg peak near zero, the damage is spared upon surrounding tissue. Image taken from *Proton Therapy Physics*.[3]

1.1.1 In-vivo verification using PET

A precise measurement of the Bragg peak location during radiation treatment would be of great benefit to the quality of proton therapy. If the location of the Bragg peak is known during treatment, then this could lead to more optimal radiations of tumor tissues, eventually resulting in shorter therapy sessions and more patients being able to obtain treatment. At the moment, research is being conducted on methods of in-vivo verification. [2][4] A large amount of this research involves using a PET-scanner, PET stands for *Positron Emission Tomography*, during treatment to trace the proton beam inside the body of the patient.[5] When protons move through the body, nuclear interactions produce various radioactive isotopes, some of which are positron

emitters. The most produced positron emitting isotopes are ^{15}O($\tau_{\frac{1}{2}}$=2 min), ^{11}C($\tau_{\frac{1}{2}}$=20 min), ^{30}P($\tau_{\frac{1}{2}}$=2.5 min) and ^{38g}K($\tau_{\frac{1}{2}}$=7.6 min).[6] The in-vivo verification can be performed offline, which means moving the patient right after radiation to another room with a PET-scanner. Nischwitz *et al* and Kurz *et al* provide examples of clinical tests of offline in-vivo verification with carbon ion therapy.[7][8] Within this timespan of moving the patient, a significant amount of the positron emitters can already have decayed. Also there is the phenomenon of *biological washout*. Biological washout is when the body functions pick up the radioactive isotopes and move them throughout the body. This causes blurring in the PET-scan, especially by the longer-living isotopes. In-vivo verification can also be performed online, which means a PET-scanner is available in the same room as where the radiation takes place. The benefit is that the patient can remain in place and the scan can be performed right after irradiation. However, this requires a complicated construction of implementing a PET-scanner in a radiation room which does not obstruct the proton beam. Ferrero *et al* provides a clinical test of such an online PET-scan.[9]

1.2 In-vivo verification with very short-lived isotopes

Two problems with performing in-vivo verification through PET using the above mentioned isotopes, both due to their several minute-long half lives. These two problems are:

- The long-living isotopes can build up in the irradiated area, but will also spread around due to biological washout. This will create blurring for PET imaging.
- The radioactive intensity of an isotope is inversely proportional to its half-life. Therefore, the long-living isotopes have insufficient intensities to provide the required counting statistics which is needed for real time feedback.

To counter these problems, an in-vivo PET verification using on very short-living isotopes is being developed. A very short-living isotope

will decay at the immediate location of the Bragg peak. So if the origin of the decay of this very short-living isotope is located, then the Bragg peak position is also instantly found. See figure 1.2 for a sketch of the comparison. At PARTREC, research is conducted into developing in-vivo verification based on very short-living isotopes. PARTREC (Particle Therapy Research Center) is a research facility of UMCG in Groningen, The Netherlands dedicated to the improvement of proton therapy.[10] At PARTREC, $^{12}_{7}$N is being considered as a very short-living isotope to be used in in-vivo verification. ^{12}N has the following desirable properties:

- A relatively extremely short half-life of 11 ms.
- All ^{12}N decays result in a positron emission. 1.9% of all ^{12}N decay also emits a gamma of 4.4 MeV.
- ^{12}N is produced in carbon irradiated with protons in sufficiently usable amount. ^{12}N is the dominant radioactive isotope for the first 70s of irradiation in carbon-rich adipose tissue.[6]

Ozoemelam *et al* provides an experiment performed at PARTREC of PET-based range verification of a proton beam based on ^{12}N.[11] Two modified Siemens Biograph mCT-PET-scanners imaged the PET-activity of PMMA and graphite targets. These targets were irradiated by a pencil proton beam pulses, 10 ms on/90 ms off, with an energy of 150 MeV. The found results are the standard deviations in activity range for the PMMA and graphite targets. These are 2.5 mm and 2.6 mm(1σ) for 10^8 protons per pulse and 0.9 mm and 0.8 mm(1σ) for 10^9 protons per pulse. These results are for the delivery of only one beam pulse.

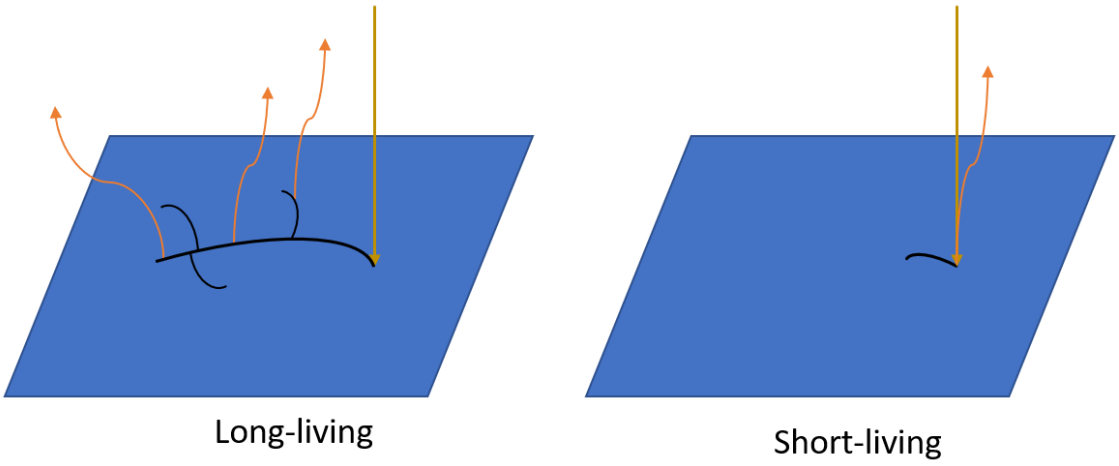

Figure 1.2: The problem with using long-living isotopes for PET imaging compared to using short-living isotopes. The golden arrow indicates the proton beam moving across a surface. The black curves represent the radioactive isotopes which are produced by the proton beam in the material. As the proton beam moves across the target area, it leaves behind a decaying trail of long-living isotopes in its path. This trail also expand due to biological washout. The in-vivo verification attempt to measure the location of the Bragg peak, the end of the proton beam, through the detection of the radiation emitted by these isotopes, indicated by the orange curved arrows. As the treatment continues, the beam moves around and the isotopes spread, the in-vivo verification of the Bragg peak location becomes difficult from the radiation. On the right is the same situation, but only with very short-living isotopes. The proton beam cannot leave a trail with very short-living isotopes, as they decay too fast. Therefore, the location of the radiation emitted by these very short-living isotopes always indicates the location of the Bragg peak.

1.2.1 Detection of ^{12}N

This thesis is aiding in the detection of ^{12}N produced in graphite through gamma spectroscopy instead of PET-imaging. The original intention of this thesis is the determination of the cross section of the production of ^{12}N in proton-irradiated graphite, also noted as ^{12}C(p,n)^{12}N, with high energy protons. The only published measurement of the ^{12}C(p,n)^{12}N cross section is from Rimmer & Fisher.[12] This measurement was performed up to a proton beam energy of 48 MeV whereby the resulting cross section values have a precision of $\pm 15\%$. The original intent of this thesis was to irradiate a graphite target of 0.5 mm thick submerged

in a movable water basin. The beam path length through water can be adjusted by moving the water basin such that the proton beam energy hitting the target can be adjusted during the experiment. The intent is to measure the production of ^{12}N at various energies and from that determine the cross sections at these energies. This would lead to an extension of measured cross section of ^{12}C(p,n)^{12}N up to 190 MeV, improving on the measurement of Rimmer & Fisher. This knowledge is needed to accurately determine the production of ^{12}N from radiation data. The measurement of ^{12}N would be performed by the detection of prompt gammas of 4.4 MeV, instead of the 511 keV gammas from positron emission and annihilation. The measurement of 4.4 MeV is chosen over 511 keV because, due to the very short half-life, the emitted positrons have a large kinetic energy. The large kinetic energy causes the location of positron annihilation to be relatively far away from the location of the decaying ^{12}N. As the graphite target has a thickness of 0.5mm, most positrons will annihiliate outside of the target. The thickness of the graphite target is small to prevent variation of proton energy inside the target, ensuring that a specific proton energy can be set. This original intention is postponed to future experiments however. This is due to difficulties encountered during the measurements of ^{12}N in a 0.5 mm graphite target submerged in the water basin. The work of this thesis was changed towards detecting ^{12}N in a 5.2 mm graphite target with a proton beam with an energy of 90 MeV. The goal was to improve on detecting ^{12}N through the measurement of 4.4 MeV gammas at the PARTREC facility. Some improvements are suggested based on experience from the irradiation of the 5.2 mm thick graphite target. These improvements are omitting the BGO-detector, pulsing the PMT of the NaI-detector and covering the NaI-detector with cadmium. These improvements were to be implemented in the final experimental session in this thesis, but due to technical difficulties regarding the cyclotron, it was no longer within the timespan of this thesis. Through manipulation of the data through an energy correction, evidence of the production of ^{12}N has been found during the second experimental session. However, confirmation can only be made when the described postponed session is performed.

Chapter 2

Theory

This chapter summarises knowledge about nuclear physics fundamental to understanding the detection of ^{12}N. The majority of the contents of this chapter is transcribed from from the book *Introductory Nuclear Physics* by K.S. Krane.[13]

2.1 Nuclear decays and radiation

2.1.1 Nuclear decay

Nuclear decay happens when an unstable atomic nucleus releases energy by emitting radiation. Nuclear decay is a completely random process when regarding a single unstable nucleus. Due to the quantum mechanical properties of the decay process, it is impossible to exactly predict when an unstable nucleus decays. Another notable property regarding time of decay is that the probability of decaying does not change with time. In contrast, almost everything else has the property that the chance of 'decaying'(breaking down, dying) increases with its age. However, for large ensembles of unstable nuclei, it is possible to determine the amount of unstable nuclei which are left over after some time period. Consider an ensemble of unstable nuclei. The rate of decays per unit of time is linearly proportional to the amount of nuclei, N. This gives:

$$-\frac{dN}{dt} = \lambda N \tag{2.1}$$

where λ is the *decay constant*. This equation is a first-order differential equation with solution for N:

$$N(t) = N_0 e^{-\lambda t} \tag{2.2}$$

where N_0 is the amount of unstable nuclei considered at the start of the time period and $N(t)$ is the amount of nuclei after time period t. Every type of ensemble of unstable nuclides has its own decay constant. Some radioactive nuclides have very large decay constants and go away within the second it is created and some radioactive materials continue to be radioactive and thus emit radiation for thousands of years.

Instead of a decay constant λ, the half-life $\tau_{\frac{1}{2}}$, is also considered due to it being a more concrete constant to imagine. The half-life of a radioactive nuclide is the time at which the amount of unstable isotopes has decreased by half. The half-life of a nuclide can be calculated by equating the decay factor $e^{-\lambda t}$ with $\frac{1}{2}$. This gives:

$$\tau_{\frac{1}{2}} = \frac{\ln(2)}{\lambda} \tag{2.3}$$

2.1.2 Types of radiation

This thesis deals with the measurement of radiation to determine the amount of ^{12}N produced after proton radiation. Therefore it is important to have a clear overview of the several types of radiation that exist and their importance in this thesis.

Alpha

Although not essential to this thesis, alpha radiation is conventionally the first type of radiation treated in literature. Alpha radiation consists of alpha particles, or in short alphas(α). These alphas are the nucleus of the $^4_2$He atom; two protons and two neutrons bound together. Alpha radiation occurs in nature when an alpha particle is emitted from an atom undergoing alpha decay. The decaying atom which ejects an alpha particle decreases in atomic number by 2 and mass number by 4. For example, the decay from the most common uranium isotope, $^{238}_{92}$U, to

an isotope of thorium is an alpha decay:

$$^{238}_{92}\mathrm{U} \rightarrow {}^{234}_{90}\mathrm{Th} + {}^{4}_{2}\mathrm{He} \tag{2.4}$$

Alpha decay occurs when the electromagnetic repulsion surpasses the strong force in the decaying nucleus in strength. The strong force, or nuclear force, is what binds the nucleons in a nucleus together. The strong force is, as the name dictates, strong, but its range is very small. In contrast, the electromagnetic force has an infinite range, but is much weaker than the strong force. This small range of the strong force makes it difficult for the strong force to stay dominant over the electromagnetic repulsion between protons and to keep nucleons bound in the large-sized nuclei. When it does happen when nucleons are out of range of the strong force, the electromagnetic repulsion takes over and an alpha particle is ejected. The reason why an alpha particle is emitted instead of loose nucleons is that the binding energy of an alpha particle is very high. This high binding energy means that the mass of an alpha particle is much lower than the mass sum of the two protons and neutrons. Therefore it is energetically favourable to emit an alpha particle than four loose nucleons.

Beta

Beta radiation consist of beta particles(β) or betas in short. Beta particles are simply either electrons or positrons, denoted respectively as β^- and β^+. The positron is the antiparticle of the electron and is therefore positively charged. Beta radiation occurs after a nucleus undergoes beta decay. This is when a neutron or a proton inside the nucleus turns into the other nucleon and emits a beta particle. A proton can turn into a neutron by emitting a positron and a neutrino. Correspondingly, a neutron can turn into a proton by emitting an electron and an antineutrino. These reactions are as follows:

$$^{1}_{1}\mathrm{p} \rightarrow {}^{1}_{0}\mathrm{n} + \beta^+ + \nu_e \tag{2.5}$$

$$^{1}_{0}\mathrm{n} \rightarrow {}^{1}_{1}\mathrm{p} + \beta^- + \bar{\nu_e} \tag{2.6}$$

Through beta decay, the atomic number of a nucleus changes without changing the mass number of the nucleus. The nucleus can then decay

towards a proton number which is more stable.

Beta radiation is used in both industry and medicine. In medicine, beta emitters are used to treat certain types of cancer or as tracer material for diagnostic methods such as *Positron Emission Tomography*(PET). Beta radiation is used in industry to test the thickness of certain flat materials. By irradiating and measuring the outgoing radiation on the other side of the material the manufacturer can see if the thickness of the material is the same everywhere in the material. Beta radiation is easy, but not as easy as alpha radiation, to shield. A centimeter or two of a material with a low atomic number, for example plexiglass, can already stop beta radiation.

Beta decay, more specifically the emission of positrons, is very important for gamma spectroscopy. Since a positron is the antiparticle of an electron, it will eventually annihilate with an electron in the environment after emission. This *positron-electron annihilation* will produce two gammas, photons, which will travel in opposite direction of each other:

$$\beta^+ + \beta^- \rightarrow 2\,\gamma(511\,\mathrm{keV}) \tag{2.7}$$

Each gamma will have an energy of 511 keV. This energy is because the complete rest mass of both the electron and positron , which is 511 keV for both betas, are converted into energy for the two produced gammas. The conservation of momentum ensures that this converted energy is evenly divided between the two gammas. The conservation of momentum is also the reason that the gammas travel in opposite direction. A gamma detector can detect one of the two produced gammas. Since this type of annihilation radiation is extremely common, the 511 keV gamma spectroscopy peak is a well-defined component for performing an energy calibration on the gamma spectrum. This means that in an energy spectrum, there will normally be this 511 keV peak present which can be used as a reference to identify the energies corresponding to the other peaks. The characteristic 511 keV energy for these gammas is what a PET scanner keeps track off during diagnostics. Also in this thesis, the 511 keV radiation due to positron annihilation will play a vital role for calibration.

Gamma

After a reaction, such as an alpha or beta decay, the nucleus can be in an excited state. This means that the nucleus still has some energy to emit until it reaches a stable state. The nucleus can reach its stable ground state by emitting this remaining energy in form of one or multiple photons. This emission of photons is called gamma radiation(γ). The ejected photons from the nucleus are called *gammas*. Gamma radiation is at the highest energy end of the electromagnetic spectrum with photon energies of about a few keV and above. The energy of gamma radiation emitted through radioactive decays ranges between a few hundred keV and a few MeV. Because of its high energy, gamma radiation is ionising radiation. This means that the impact of a gamma upon an electron bound in an atomic potential can transfer enough energy to detach this electron from its atom. The ejection of an electron through the impact of a photon is called the *photo-electric effect*, whereby the atom gets ionised as this occurs. The ejected electron carries the energy of the gamma, so if the energy of the electron is measured, the energy of the gamma can be determined. When the energy of the photons exceeds 1022 keV, the combined mass of an electron and a positron, then *pair-production* can occur. Pair-production is when a photon splits up into an electron and a positron. The produced positron will react with an electron in the environment, resulting in the previously described positron-electron annihilation. Pair-production can cause the effect of *single & double escape peaks* during gamma spectroscopy. The escape peaks will be discussed in 3.2.2. Besides the photo-electric effect and pair-production, there is another interaction between matter and gamma radiation called *Compton scattering*. Compton scattering will be discussed later separately as it plays a significant role in the measurement of gamma radiation.

The gamma decay of a nucleus in an excited state into a lower energy state can be almost instantly, also called a prompt decay. A nucleus can also stay longer in an excited state, with a half-life of about 10^{-9}s or longer. Such a state is called *metastable*. The half-life threshold of when a state is called metastable is not clearly defined. Gamma radi-

ation is impossible to be shielded from completely. However, it can be exponentially decreased by using high density materials such as lead. During the cyclotron irradiation experiments, lead blocks are available for shielding equipment and people from harmful gamma radiation.

Neutron

In much rarer situations, it can also happen that nucleons contain enough energy to overcome the binding energy of individual nucleons of about 8 MeV. As a consequence, a single neutron can be emitted from the nucleus, causing neutrons to freely fly around. This collection of free neutrons flying around is called neutron radiation. When freed neutrons have an average energy of 25 meV, corresponding with room temperature, the neutrons are called *thermal neutrons*. During proton radiation experiments, the target and surrounding material can gain enough energy to release neutrons from their nuclei. These released neutrons have a relatively large energy, but loose energy through collisions with surrounding materials, mostly the concrete housing. The slowed down neutrons will *thermalise*, turning into thermal neutron gas. The thermal neutron gas can then react with the surrounding material, creating radioactive nuclei inside the surroundings. This is called *activation* of materials, which causes an increase in background radiation which complicates measurements. Thermal neutrons can be stopped from entering the surrounding materials by using materials with large neutron-capture cross-sections, for example cadmium. Such materials are called *neutron poisons*.

2.1.3 Decay and radiation of ^{12}N

The detection of ^{12}N is done by measuring the radiation emitted when ^{12}N decays. ^{12}N is produced in the experiment by radiating ^{12}C with protons, causing the following nuclear reaction:

$$^{12}_{6}\mathrm{C} + ^{1}_{1}\mathrm{p} \rightarrow ^{12}_{7}\mathrm{N} + ^{1}_{0}\mathrm{n} \tag{2.8}$$

The short notation of equation 2.8 is:

$$^{12}\mathrm{C}(p,n)^{12}_{7}\mathrm{N} \tag{2.9}$$

After ^{12}N is produced, 100% of it decays back to ^{12}C through β^+-decay with a half-life of 11 ms. 96.17% of the β^+-decays result in the ^{12}C being in the ground state. However, a tiny fraction of the ^{12}C ends up in an excited state of ^{12}C after β^+-decay. 1.9% of the ^{12}N ends up in the first nuclear excited state of ^{12}C after β^+-decay. See figure 2.1. The first excited state of ^{12}C has an energy of 4439.8 keV, which is in this thesis rounded to 4.4 MeV. A ^{12}C nucleus in this first excited state decays into the ground state through the prompt emission of a gamma of 4.4 MeV. The 1.9% is called the *branching fraction* of ^{12}C ending up in its first excited state through the β^+-decay of ^{12}N.

As the decay of ^{12}N is through β^+-decay, a positron will be emitted. The emission of a positron will result in two 511 keV gammas through positron-electron annihilation. Ideally, the measurement of 511 keV gammas would lead to the detection of ^{12}N. Proton radiation upon graphite however also produces ^{11}C through $^{12}\mathrm{C}(p, pn)^{11}\mathrm{C}$. ^{11}C has a half-life of 20 minutes, so it builds up in the graphite during irradiation. This makes it impossible to determine if 511 keV gammas are from ^{12}N or from ^{11}C right after irradiation.

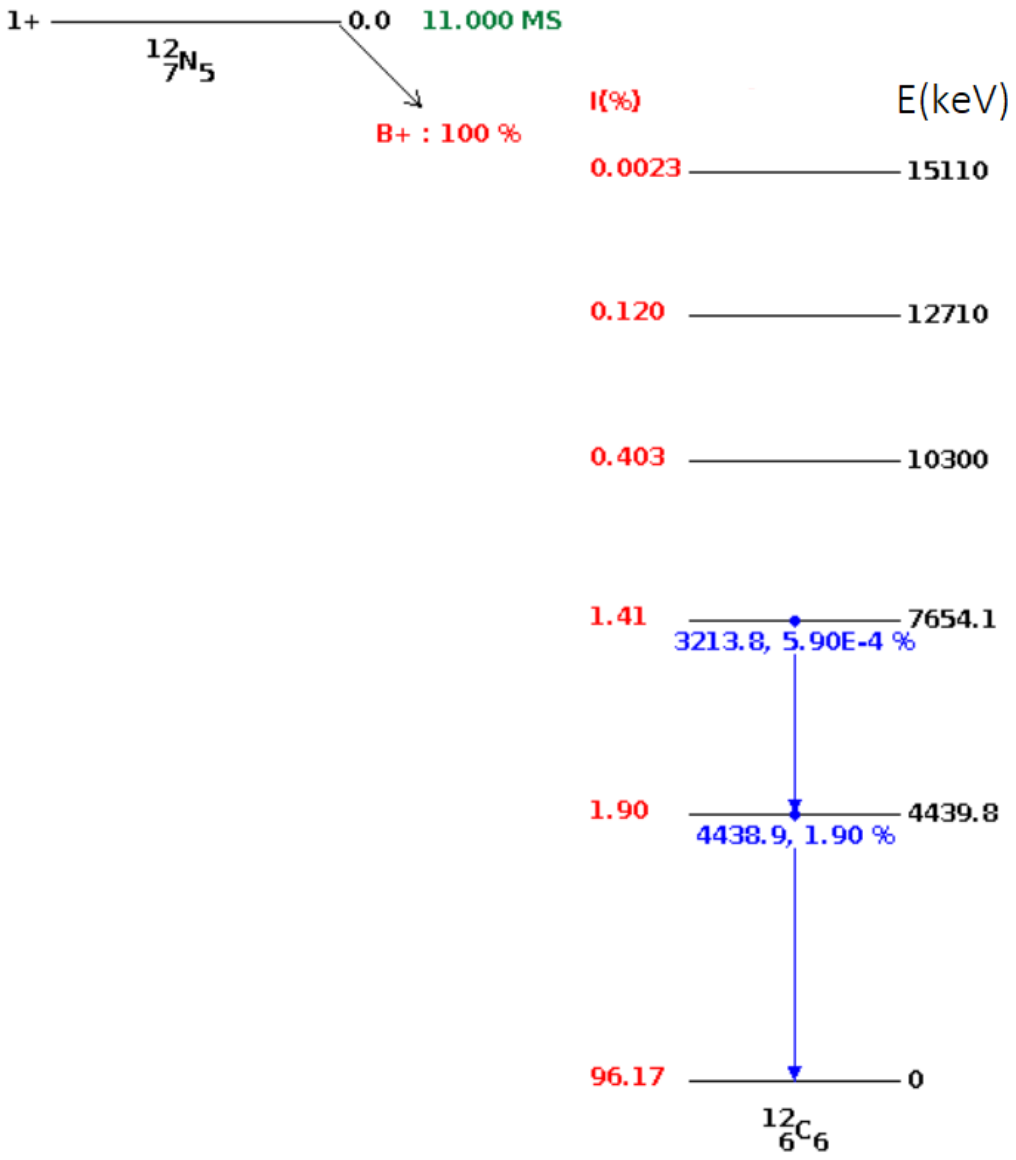

Figure 2.1: Decay scheme of ^{12}N from the NNDC.(modified) The I(%) in red indicates the branching fraction of each energy state of ^{12}C. The energy of each level is indicated by black. A 4.4 MeV gamma is emitted when the transistion from the first excitated state to the ground state occurs with the indicated intensity of 1.9%. A second possible gamma emission of 3.2 MeV is also possible through the transition of the second to the first excited state, however its intensity is too low for use.

2.1.4 Compton scattering

Compton scattering is the inelastic scattering of a photon by an electron. Inelastic means that the energy of the photon is not conserved

as the electron gains momentum from the photon. The direction of the scattered photon also changes. See figure 2.2. The scattering angle and the photon energy after scattering are related by the formula:

$$E' = \frac{E}{1 + \frac{E}{m_e c^2}(1 - cos(\theta))} \tag{2.10}$$

where

- E is the energy of the photon before scattering.
- E' is the energy of the photon after scattering.
- $m_e c^2$ is the rest mass of the electron(511 keV).
- θ is the scattering angle.

The scattered photon takes on a large, continuous range of values for energy. The gamma energy together with the atomic number of the medium determines which of the matter-gamma interactions, photo-electric, Compton or pair-production, is dominant.[20] See figure 2.3. The gamma energy range relevant for this thesis is between a few hundred keV and a few MeV. This makes Compton scattering the most dominant form of interaction between matter and gamma radiation. In summary:

- Compton scattering is dominant in the relevant energy range.
- The energy of the Compton-scattered photon can have any value within its continuous range.

These two properties give rise to the situation that Compton scattering can occur inside the detector itself. When this happens, assuming the scattered photon does not get detected, the recoil energy of the electron which the photon has scattered upon gets measured by the detector. This measurement adds distortion to the gamma spectrum called the *Compton edge*. To filter out detection events due to Compton scattering, a so-called *anti-Compton shield* surrounds the detector. The details of the Compton edge and anti-Compton shield will be discussed in 3.2.2.

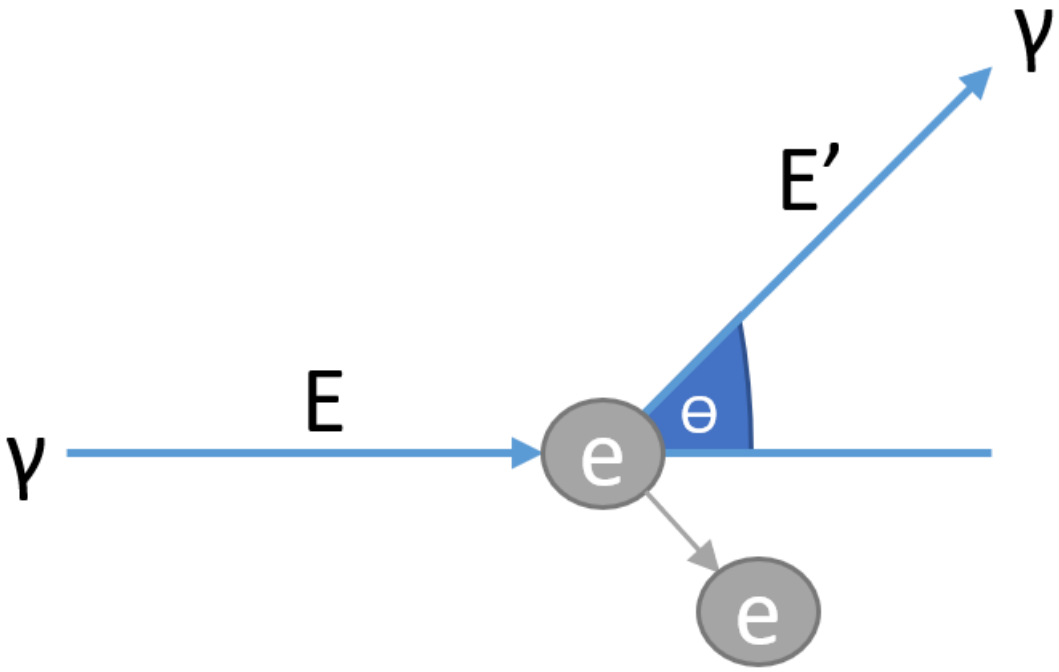

Figure 2.2: Drawing of Compton scattering. A gamma with energy E scatters with an electron and changes in direction and energy. The electron also gain momentum due to conservation of momentum. The relation between the scattering angle θ and the energy after scattering of the gamma is given in equation 2.10

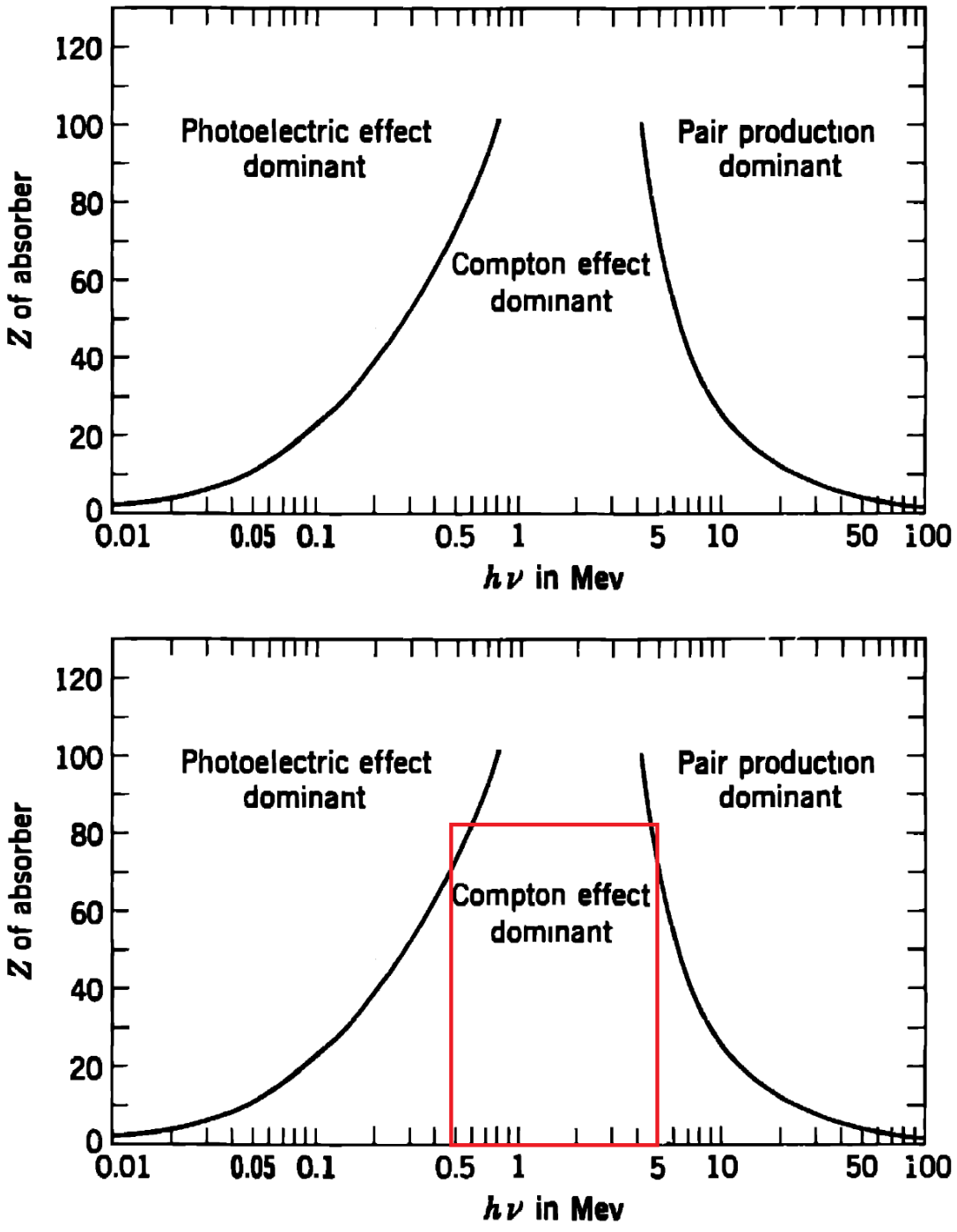

Figure 2.3: Graph taken from *The Atomic Nucleus* by R.Evans.[20](modified) The graph shows which matter-gamma interaction is dominant for which gamma energy and atomic number of the medium. The red square roughly indicates the gamma energy and atomic number relevant for this thesis, which is located in the Compton effect-dominated area.

2.2 Nuclear cross-section

Each nuclear reaction has a *cross-section*, σ. The cross-section of a nuclear reaction describes the probability of a reaction happening when the required particles meet. Assuming only one reaction can occur, in a situation whereby a medium is being irradiated by particles, the cross-section of this reaction gives information about how many of those incoming particles will undergo the reaction with nuclei in the medium. The incoming particles can also pass through the medium without undergoing any reaction. In a more complex situation, other nuclear reactions can also occur which all have their corresponding cross-section. The cross-section is needed to calculate the *reaction rate* of a certain reaction. The reaction rate is how many of a certain reaction occurs per unit of time, per unit length. The reaction rate, R, is the product of the cross-section with two other factors:

$$R = \Phi\sigma\rho \tag{2.11}$$

whereby

- Φ is the flux of the incoming particles, the amount of incoming particles per unit of time.
- ρ is the atomic density of the medium, the number of atoms per unit volume.

The product of the flux and the density states how many particles will be in proximity of each other, where the cross-section states how many of those particles will actually react with each other. Dimensional analysis shows that the cross-section is expressed in units of area. The most conventional unit for the cross-section is *barn*, b, whereby 1 barn is $10^{-28}\mathrm{m}^2$. Despite using area as unit, the cross-section is unrelated to any physical size like that of any particle. Relevant to note for this thesis is that the cross-section for nuclear reactions depends on the kinetic energy of incoming particle. See for example the cross-section of incoming neutron scattering off protons in figure 2.4. The main goal in which this thesis aids is the determination of the cross-section of the ${}^{12}_{6}\mathrm{C}(\mathrm{p,n}){}^{12}_{7}\mathrm{N}$ reaction at high energies. The cross-section of that reaction is not known accurately enough at those higher energies. The fact that

the cross section depends on the kinetic energy of the incoming protons is applied in 3.4 in order to predict the production of ^{12}N during the radiation sessions.

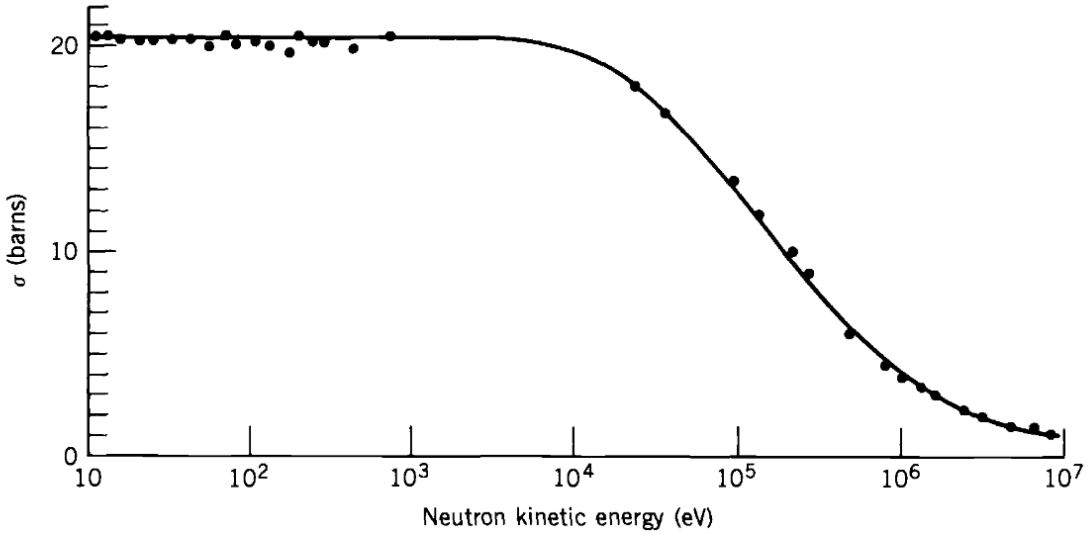

Figure 2.4: The cross-section of neutron-proton scattering at various kinetic energies of the incoming neutron. The value for the cross-section stays constant at 20 barn up to 10 keV and then starts to drop.

Chapter 3

Experiment Principle

This chapter covers the components of a gamma detector including anti-Compton shield, gamma spectroscopy, the basics of a pulsed proton beam and a prediction of the amount of produced 4.4 MeV gammas through calculation. The fundamentals of radiation detection and the detector components are transcribed from the book *Radiation Detection and Measurement* by G.F. Knoll.[14]

3.1 General gamma detector setup

Here the general components and how they work will be explained. The specifics regarding the detectors used for this thesis will be in section 4.1. A detector which is used to perform gamma spectroscopy consist of a setup of different components. This detector setup consist of a scintillator coupled to a photomultiplier tube (PMT). This PMT is connected to a data acquisition device, which is connected to the researcher's computer. This section serves as an overview of the components of a general gamma radiation detector. In short, a scintillator receives a gamma particle and gives off a signal corresponding to the energy deposition from the particle into the detector. This signal is amplified by the PMT and sent to the data acquisition device (DAQ). The detector setup also includes an anti-Compton shield which surrounds the core of the detector. The anti-Compton shield is also a detector itself which is used to filter out measurement events caused by Compton scattering. See figure 3.1 for a schematic drawing of the different components that make up the detector setup used for this

thesis. See figure 3.2 for a picture of the NaI-detector used in the first two experiments. The DAQ converts the signal to a signal which the data acquisition software on the researcher's computer can read and gives the computer the converted signal. The converted signal is then adding to the energy bracket corresponding to measured energy of the gamma. By counting these converted signals and sorting them in their respective energy brackets, one obtains a histogram which is the energy spectrum. This energy spectrum is then used for further data analysis.

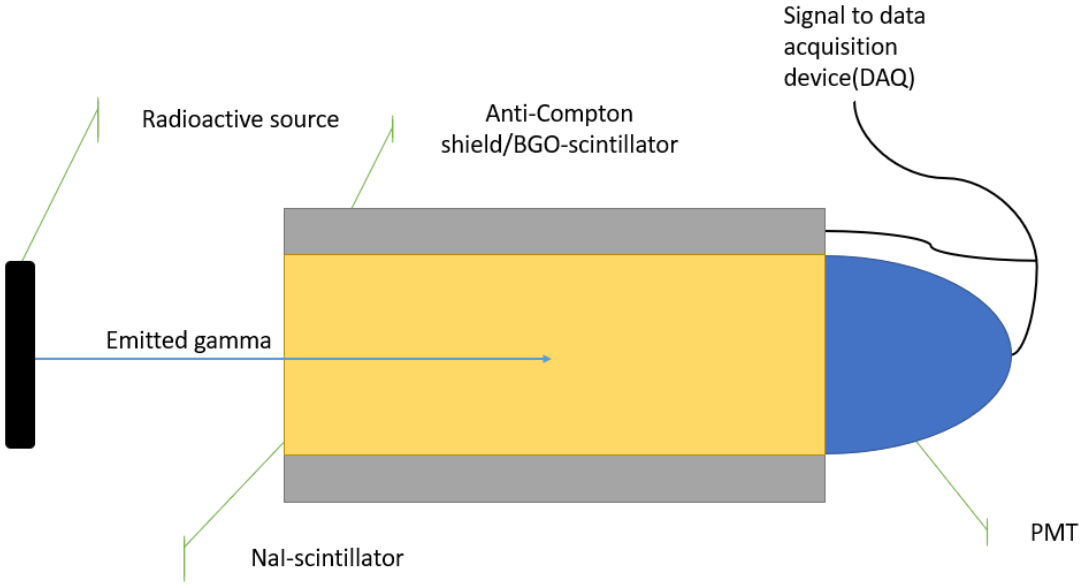

Figure 3.1: Schematic drawing of the detector setup used in this thesis. In the ideal case, the emitted gamma deposits its full energy into the NaI-scintillator. The signal which the scintillator gives off gets amplified by the PMT and transported to the DAQ.

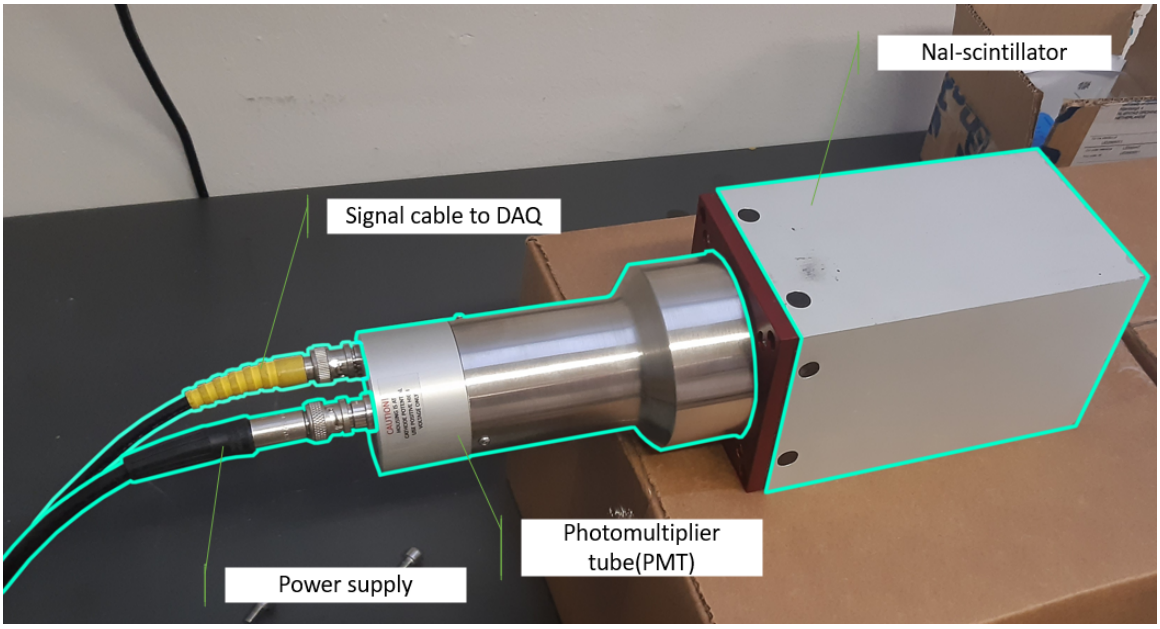

Figure 3.2: Picture of the NaI-detector used in the first two experiment sessions of this thesis. During the first two sessions, this NaI-detector was inserted in the anti-Compton shield.

3.1.1 Scintillator

A scintillator is a material which emits visible light when ionising radiation passes through it. The amount of photons which the scintillator emits is proportional to the amount of energy the incoming ionising particle deposits in the scintillator. By counting the amount of photons emitted by the scintillator during a detection event, the deposited energy of the incoming particle is known and can be noted. The scintillator is therefore the detector component at the front which produces the signal while the other component are there for signal conversion and counting. Many different types of materials can be used as a scintillator, which all have their own properties. Most of these are split up into two categories: *organic* and *inorganic*. Relative to each other, organic scintillators are used to detect beta and neutron radiation while inorganic scintillators are used for gamma spectroscopy. Organic scintillators contain large amount of hydrogen, which has a large cross section with massive particles such as betas and neutrons. In contrast, inorganic scintillators are often crystals which contain no hydrogen, but

have the high density and atomic number suitable for interactions with incoming gammas. Since this thesis is about gamma spectroscopy, only the mechanism behind inorganic scintillators is considered.

Inorganic scintillators are often crystals. In a pure crystal, electrons are either in the *valence band* or in the *conduction band*. Electrons in the valence band are energetically bound to sites in the crystal lattice. Electrons which have enough energy to be in the conduction band can move around in the crystal. An electron can be excited from the valence band to the conduction band through incoming ionising radiation such as a gamma. In a pure crystal, an electron can never energetically be between the valence band and the conduction band. Therefore this area between them is called the *forbidden band*. When an electron is excited with enough energy to bridge the forbidden band and enter the conduction band, a "hole" is leftover in the valence band. When an electron decays back into this valence hole, a photon will be emitted. However, the energy gap between the valence band and the conduction band is often so large that the emitted photon will not be in the spectrum of visible light. On top of that, the decay of an electron directly from the conduction band to the valence band is an inefficient process. The decay from the conduction band to the valence band could result in lattice vibrations, also known as phonons. To ensure that the crystal can emit visible light when subjected to ionising radiation, impurities are added to the material. These impurities are called *activators*. The addition of activators creates sites in the crystal, *luminescence centers*, where extra energy states are added within the forbidden band. These extra energy states have smaller energy separations with the valence band compared to the valence band with the conduction band. See figure 3.3 for a schematic drawing of the energy band structure of a scintillator with a luminescence center. This increases the chance of emitting a visible light photon when an electron decays into the valence band from one of these extra energy states. When ionising radiation passes through the scintillator, it can excite a number of electrons from the valence band to the conduction band and also leave behind the same number of holes in the valence band. Such holes will move towards a luminescence center and ionise it, because ionising a luminescence

center is energetically more favourable than the pure crystal sites in the material. A free electron will move throughout the crystal until it encounters an ionised luminescence center through which it will decay rapidly back into the valence band. When the activators are implemented correctly, these electrons decaying through such a center will result into the emission of photons in the visible light spectrum. The number of electrons which the incoming ionising particle excites to the conduction band is proportional to the deposited energy of the particle. By counting the number of emitted photons from the electron decaying, the energy of the incoming particle can be determined. However, the number of visible light photons is too low for measurement and digital registration. To combat this, a photomultiplier tube is connected to the scintillator.

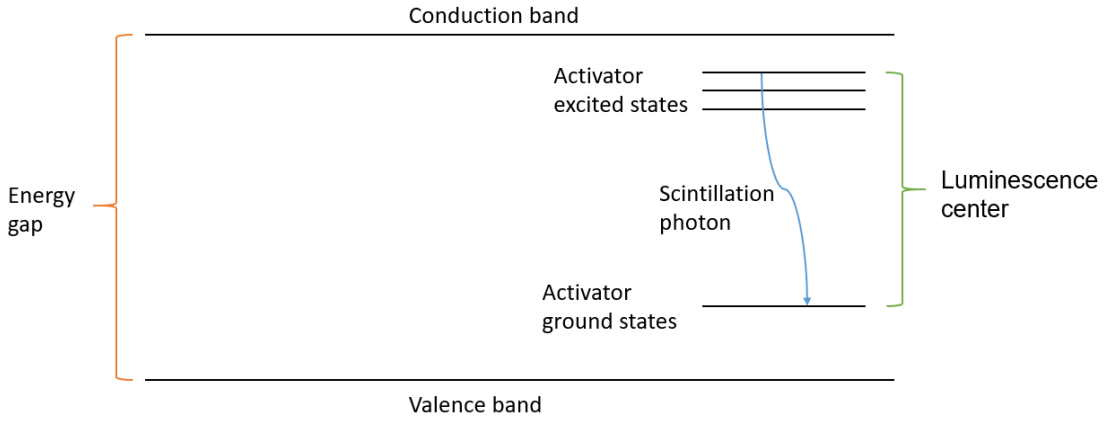

Figure 3.3: Schematic drawing of the energy band structure of a crystal scintillator with added activators, creating a luminescence center.

Of the inorganic scintillator materials, sodium-iodine(NaI) with traces of thallium(Tl) is the most used as scintillator in gamma spectroscopy. Also the gamma spectroscopy for the experiments of this thesis is performed by a NaI(Tl)-detector. Aside from NaI, bismuth germanate oxide($Bi_4\,Ge_3\,O_{12}$), shortend as BGO, is the scintillator component of the anti-Compton shield surrounding the NaI-detector.

3.1.2 Photomultiplier tube

In order to convert the weak signal of the scintillator into a readable and digital signal, a photomultiplier tube (PMT) is attached to the scintillator. A PMT is a vacuum tube with a photocathode and anode on opposite sides, creating an electric field. Within this tube, there is an *electron multiplier* consisting of multiple *dynodes*. The photocathode is placed against the scintillator. When the incident photons from the scintillator hit the photocathode, so-called photoelectrons are emitted inside the tube from the photocathode. Due to the electric field inside the tube, these emitted electrons are pulled through the electron multiplier towards the anode. When the emitted electrons enter the electron multiplier, they hit the first of several dynodes. When an electron with sufficient energy hits a dynode, the dynode will emit multiple electrons. These newly emitted electrons then hit another dynode, causing even more electrons to be emitted. See figure 3.4 for a schematic drawing of a PMT. This process repeats multiple times, creating an exponential growth of electrons in the electron multiplier. Such a multiplication of electrons will typically turn a single photoelectron from the scintillator into a cascade of 10^7-10^{10} electrons. When this tremendous amount of electrons exit the electron multiplier and enter the anode, a strong enough signal which is still proportional to the amount of scintillating photons can be transmitted towards the data acquisition system.

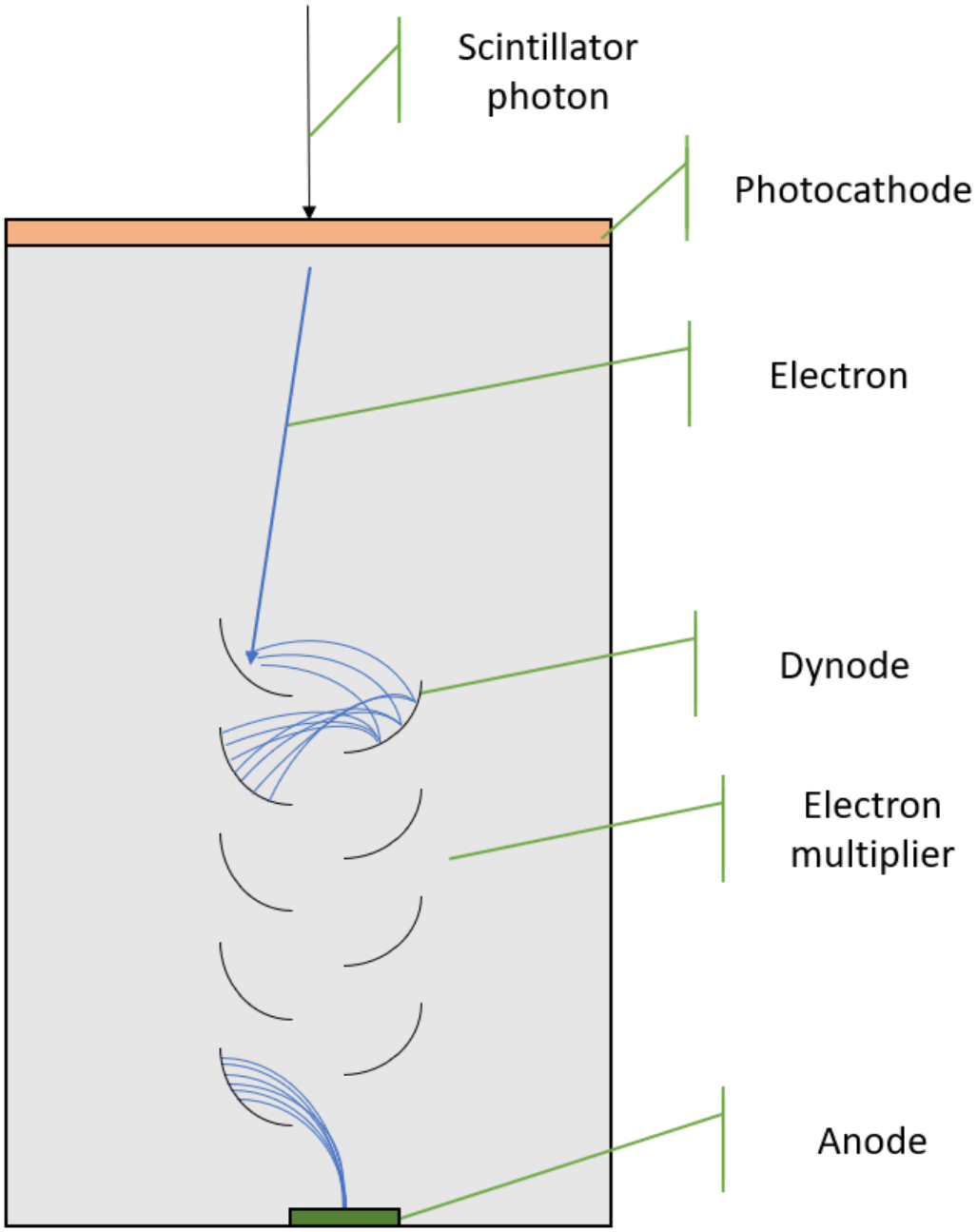

Figure 3.4: Schematic drawing of a photomultiplier tube.

3.1.3 Anti-Compton Shield

The NaI-detector is surrounded by another detector. This detector is an *anti-Compton shield* with BGO as its scintillation material. The anti-Compton shield is there to detect which measured events are the result from Compton scattering inside the NaI-detector. These measured events from Compton scattered photons can then be filtered out from the results. Compton scattering occurs when an incoming photon gets scattered off an electron. This changes the direction and energy of the photon. The energy of the electron is measured by the NaI-detector. If the scattered photon is not also detected by the NaI-detector afterwards, it is highly likely detected by the surrounding BGO-detector. This causes a measured event in both the NaI-detector and the BGO-detector with the same timestamp. The final gamma spectrum can then be filtered from Compton scattering by setting an *anticoincidence* condition on both detectors. This means that if an event occurs in both detectors each with the same timestamp, then these events are ignored. See figure 3.5 for examples of the effect of using an anti-Compton shield on gamma spectra.

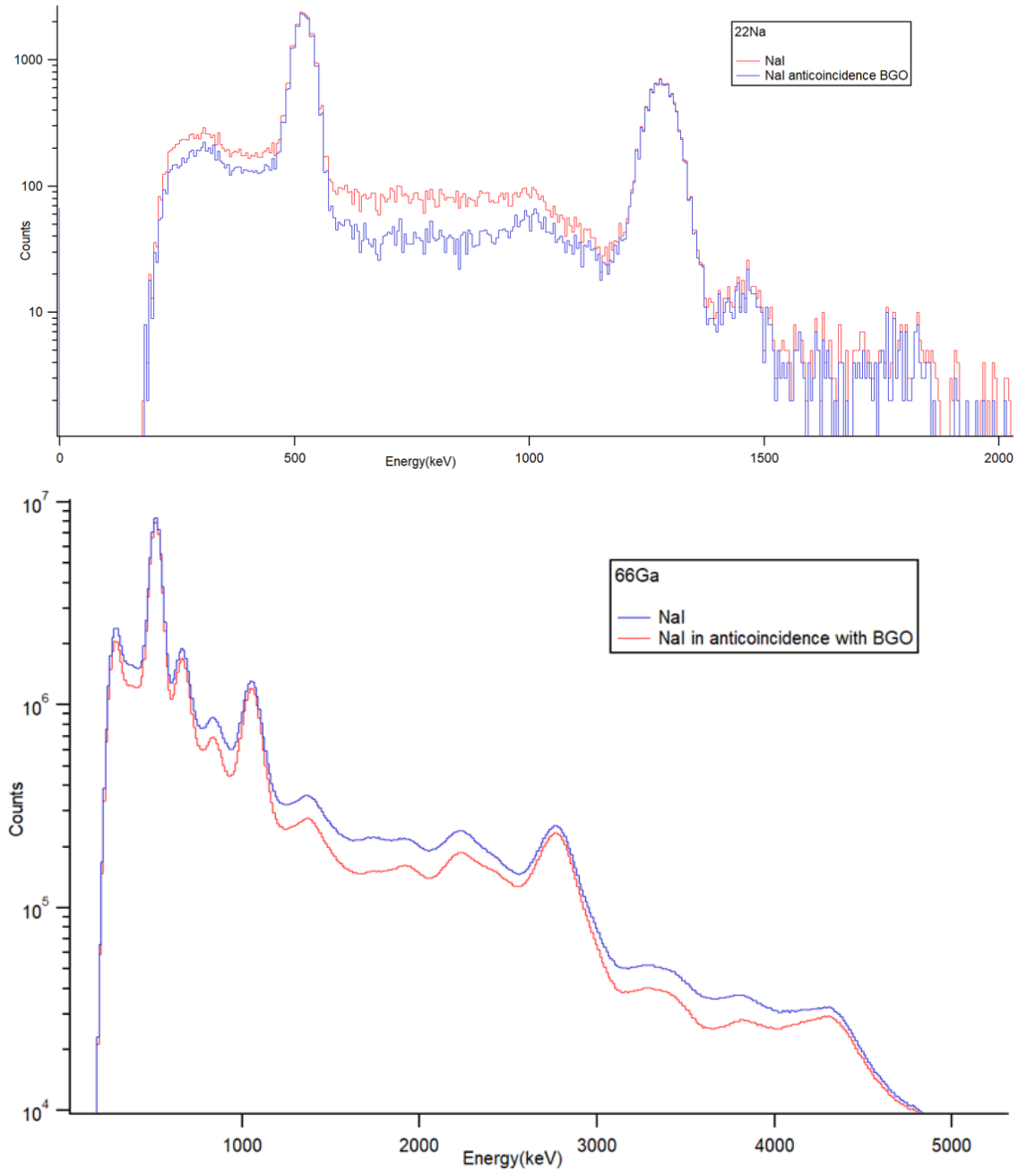

Figure 3.5: The gamma spectra of ^{22}Na and ^{66}Ga taken by the NaI-detector. The blue line is the spectrum taken by the NaI-detector. The red line is the spectrum taken by the NaI-detector in anticoincidence with the BGO-detector. If a gamma scatters through the Compton effect inside the NaI-detector, it can be picked up by the surrounding BGO-detector. If this happens, the event has the same timestamp and can be filtered out through the anticoincidence condition. This results in less background and larger peak-to-background ratio.

3.2 Gamma spectroscopy

3.2.1 Basic principle

The signals the detector obtains from measuring gammas are sorted on their energy by the DAQ software in its designated energy bracket. The collection of sorted measurement events results in a histogram which shows the amount of counts per energy bracket. This is the gamma spectrum. When a detector takes a gamma spectrum of a radioactive source, photopeaks will show up which indicates which radioactive nuclides are, or were, present in the source. The peaks will show up at the bracket location corresponding to the energy of the emitted gammas. For example, when ^{22}Na decays, it emits a positron, resulting in a 511 keV gamma and a prompt gamma of 1275 keV. The gamma spectrum will show two peaks which correspond to that location on the energy axis. See figure 3.6 for the decay scheme of ^{22}Na and see figure 3.7 for the gamma spectrum of ^{22}Na taken. A fit, often a Gaussian, is applied of these peaks to determine their intensities. The peak intensities, divided by the measurement time, give the count rate of a certain peak. The count rate can then be used to calculate the amount of a certain radioactive nuclide which is or was present during the measurement. A more detail explanation about calculating this amount is given in 3.4.

3.2.2 Background

When taking a gamma spectrum, certain phenomena show up on the spectrum as background. These phenomena can result in distortion of Gaussian fits upon peaks or be naively mistaken as peaks themselves. The source of spectrum background can be from radiation from the environment or from interactions of the radiation of the measured source. Radiation from the environment originates from the materials surrounding the detector and from cosmic rays. Concrete, ground and air are all notorious for containing enough radioactive nuclides such that their radiation gets picked up by the detector. Special mention is given to measurements in rooms where particle beams such as a proton beam take place. Various objects in such beam rooms can become radioactive during experiments and can distort future measurements. As

such environmental background radiation is ever-present, it is standard to perform a measurement without any radiation source in order to obtain a background spectrum. If the radiation from the environment is deemed to be too high, lead blocks can be used to shield the detector as much as possible.

The radiation from the measured source can cause primarily two phenomena which will give additional background on the gamma spectrum.

- The *Compton edge* or *Compton bump* is where the gamma inside the scintillator of the detector undergoes Compton scattering and the scattered gamma flies out of the detector. The scattering ensures that the gamma deposits only part of part its energy into the scintillator resulting in a wide bump in an energy domain lower than the full energy peak. The size of the detector influences the ratio between the size of the Compton bump and the full energy peak. The smaller the detector, the larger the bump is relative to the full energy peak. The full energy peak can even be barely visible next to a sizeable Compton bump if the detector is sufficiently small.

- *Double & single escape peaks* are peaks that can occur respectively 2×511 keV or 1×511 keV lower than a full energy peak. This will result in three peaks which all three appear to originate from the radiation source, but only the peak with the highest energy actually represents radiation from the source. Escape peaks can occur when the source emits gammas with energy higher than 1022 keV. Gammas above this threshold can undergo pair-production, resulting in the creation of an electron and a positron. The positron annihilates and produces two gammas of 511 keV. If one 511 keV gamma escapes without being detected, then the detector adds a count at the energy of the original gamma minus 511 keV. If both 511 keV gammas escape without being detected, the detector adds a count at the energy of the original gamma minus 2×511 keV.

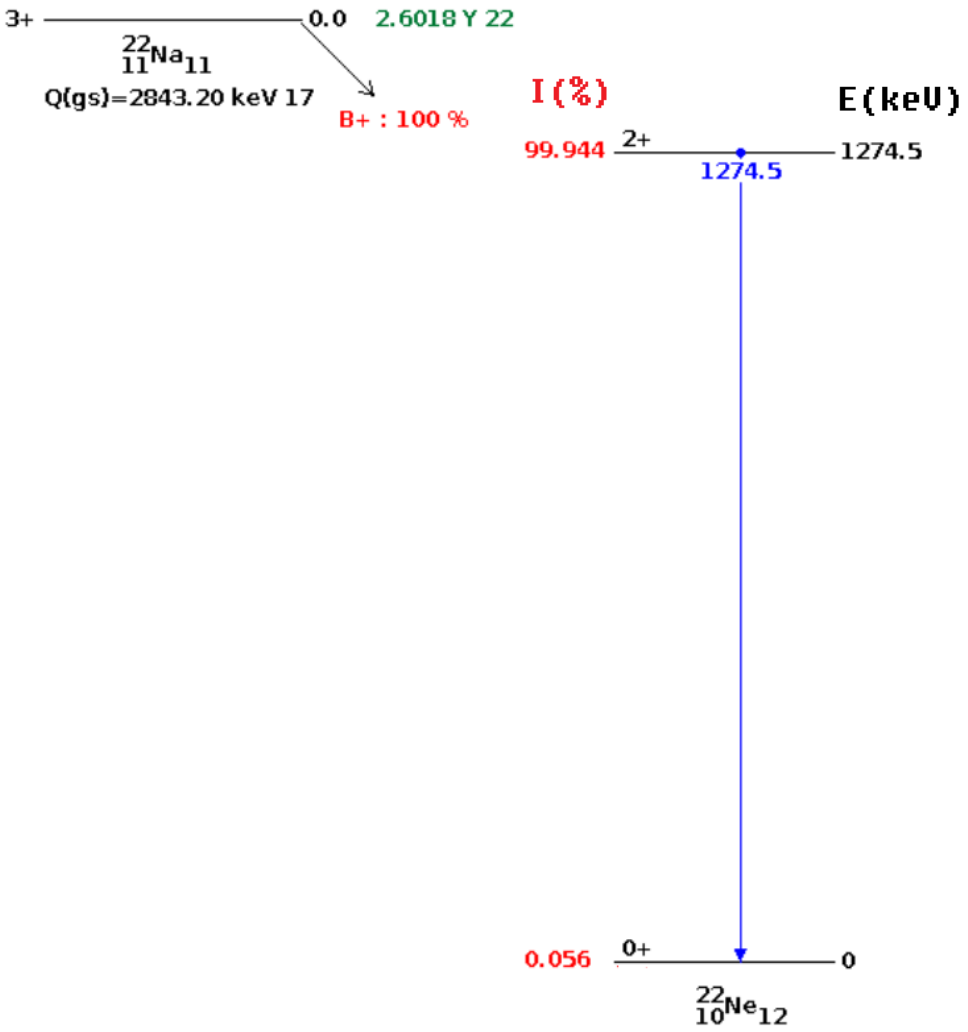

Figure 3.6: Decay scheme of ^{22}Na from the NNDC.(modified) The gamma spectrum of this decay scheme is 3.7.

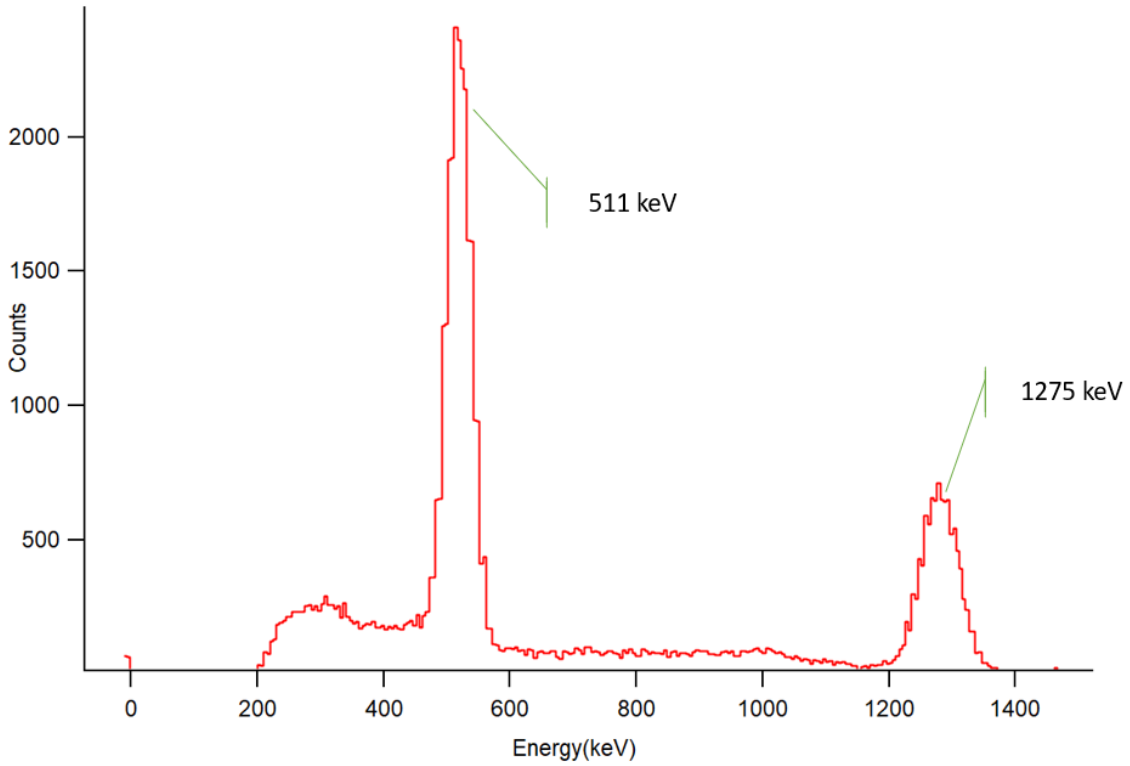

Figure 3.7: Gamma spectrum of ^{22}Na taken for 1 minute.

3.2.3 Calibration

The data acquisition device of the detector produces an output signal naively scaled to the signal input from the PMT. This results in an undetermined energy scaling of the horizontal axis. To obtain a spectrum with correct energy scaling, the spectrum needs to be manually calibrated. Calibration is done by taking a radioactive source whose energy peaks are already known. In this thesis, ^{66}Ga is used as calibration source. ^{66}Ga emits gammas with a large diversity of energies between 833.5 keV and 4806 keV upon decay.[17] A source of ^{66}Ga is produced by irradiating a small plate of zinc with a proton beam. The details for producing a ^{66}Ga-source by irradiating zinc are found in the bachelor thesis by Adrian Sidhu.[18] A spectrum is taken of a ^{66}Ga-source which shows the various energy peaks which ^{66}Ga produces. See figures 5.4 for the energy spectrum of ^{66}Ga with the peaks labelled. These energy peaks are identified as to which peak belongs to which gamma energy of ^{66}Ga. The energy scaling of the horizontal axis is performed by taking a linear fit through the energy peaks of ^{66}Ga. The linear fit is performed by taking the original spectrum, identify which energy peak is at which channel, or position, on the horizontal axis and plotting a linear fit between the energies of the peaks and their locations. The two parameters from the fit, the offset and the slope, can then be implemented in the software to obtain a properly calibrated spectrum. However, it is important to note that the correct calibration parameters can shift. These shifts can, for example, be due to a linear fit no longer being a correct and a different fit has to be applied. The benefit of using ^{66}Ga over other radioactive sources such as ^{22}Na is that ^{66}Ga gives energy peaks in the higher energy range. Having peaks around the desired measured energy of 4.4 MeV ensures that the calibration is still accurate at these higher energies. Other causes of shifting calibration parameters can be due to flaws in the detector setup such as a fluctuating PMT.

3.2.4 Counting error

When a gamma spectrum is being produced, the amount of decays per energy bracket is being counted for each energy bracket. The proba-

bility of finding x counts in each energy bracket is described by the Poisson distribution, since the average amount of counts is known from a predetermined half-life and the counting events happen independently from each other. The Poisson distribution is:

$$P(x) = \frac{\overline{x}^x e^{-\overline{x}}}{x!} \tag{3.1}$$

whereby $P(x)$ is the probability of x counts occurring and $\overline{x}$ is the average amount of counts. The Poisson distribution can approximated by the Gaussian distribution when the amount of counts, x, exceeds about 100. Since the amount of counts per bracket vastly exceeds this threshold, the approximation from a Poisson distribution to a Gaussian distribution can be taken. The Gaussian distribution is:

$$P(x) = \frac{1}{\sqrt{2\pi\overline{x}}} e^{-\frac{(x-\overline{x})^2}{2\overline{x}}} \tag{3.2}$$

For a both distributions, the standard deviation σ is the square root of the average of the amount of counts:

$$\sigma = \sqrt{\overline{x}} \tag{3.3}$$

The average amount of counts is taken to be equal to the measured amount of counts, since only once measurement per energy bracket is performed, $\overline{x} = N$. Therefore, the error margin assigned to an amount of counts in an energy bracket is the square root of its amount of counts:

$$\text{Counts per bracket} = N \pm \sqrt{N} \tag{3.4}$$

This assigned error is then used by the analysing software to perform further investigation.

3.3 Proton beam pulsing and calibration

3.3.1 Proton beam pulsing

The proton beam and measurements are pulsed in cycles during experiments. The DAQ of the detector and the cyclotron are connected to a pulse generator which creates a cycle with an adjustable time period of the order of 50-100 ms. The clock of the DAQ used to provide the

timestamp of events resets itself after a cycle. Only during a small portion within the cycle, in this thesis 10%, the proton beam is on. Assuming the correct setup with graphite as target, protons from the beam will react with the carbon atoms inside the target graphite. The reactions will result in the production of radioactive nuclides in the graphite. The beam pulsing in cycles creates a wave-like pattern between the production of radioactive nuclides in a short period and a longer period where the produced nuclides decay. See figure 3.8 for a drawing of such a wave-like pattern. Note that during the irradiation of graphite by protons, the build-up of longer living radioactive nuclides occurs. The same graphite target cannot be used for too long as the radiation of those longer living radioactive nuclides will cause significant amount of radiation.

When the proton beam is on, the detector quickly becomes saturated and cannot measure properly anymore. Within a few milliseconds after the proton beam is off, the detector starts to count again. However, the calibration of the detector is shifted due to saturation and requires some time to recover. For experimental session 2, this recovery period took about 15 ms. The DAQ software *mvme* is commanded to show a gamma spectrum with measurement events that take place in the time cycle after recovery until the start of the next beam pulse. This is made possible by connecting the same pulse generator to both the detector and the cyclotron. This creates a three-part division within a time cycle between the beam-on, recovery and measurement periods. See figure 3.9 for a labelled drawing of these three period upon a beam time cycle and see figure 3.10 for a count per energy bin versus timestamp graph for an real example encountered during irradiation.

The long duration of recovery is a problem for the measurement of ^{12}N. ^{12}N´s short half-life of 11 ms means that about 60% of the ^{12}N that was present when the proton beam was turned off has already decayed when the measurement period starts. This is one of the difficulties with measuring ^{12}N in this thesis.

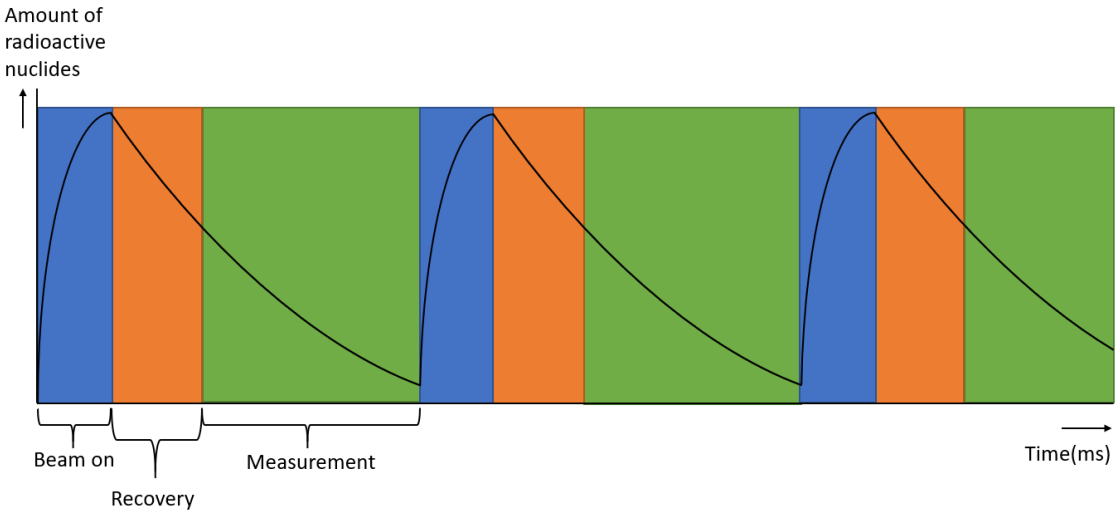

Figure 3.9: The graph of 3.8 whereby the cycles are split up into the three periods: beam-on, recovery and measurement. Ideally the period of recovery is shortened as much as possible in favour of the measurement period.

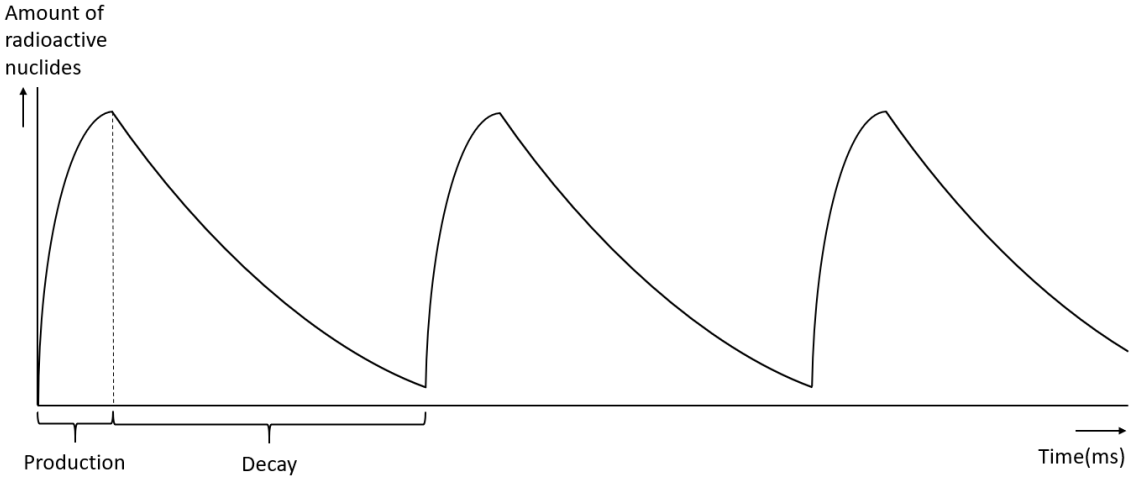

Figure 3.8: A sketched graph of the amount of radioactive nuclides over time in a pulsed beam cycles. The graph indicates three cycles starting with a beam pulse. This graph however does not include long-living isotopes.

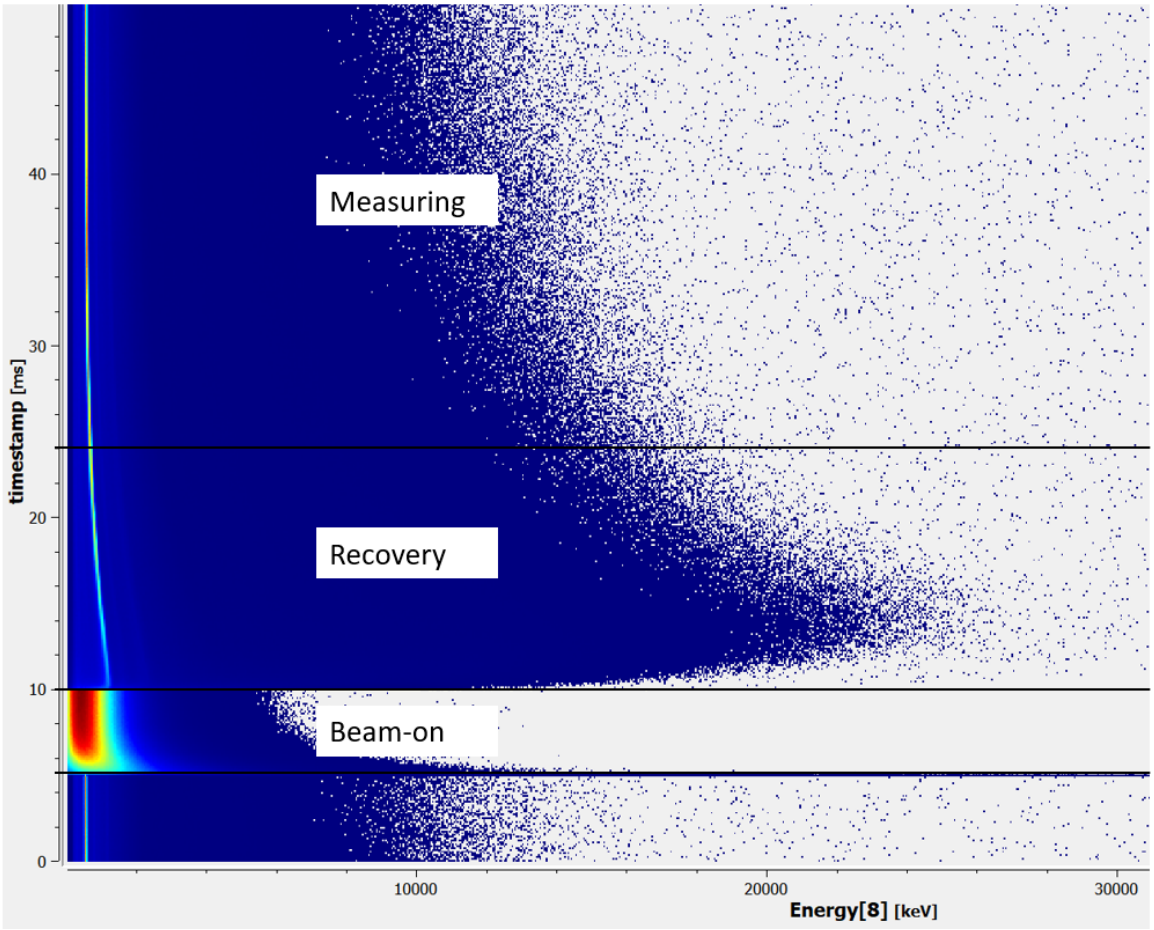

Figure 3.10: An example of a counts per energy interval versus timestamp graph as given by mvme. On the vertical timestamp axis, between 5 ms and 10 ms, the proton beam is on. The intense saturation makes the detector stop working properly. Right after the irradiation period of 5 ms, the detector has to recover. The recovery period for session 2 is the timestamp domain from 10 ms to 24 ms. This recovery is visible by the bright line that moves back to its original position. This line is the positron annihilation peak of 511 keV, which shifts due to the high count rate. A proper gamma spectrum for this session is taken by only considering the measuring period therefore ignoring the beam-on and recovery period between 5 ms and 24 ms.

3.3.2 Proton beam calibration

The proton radiation is performed at the PARTREC accelerator facility in Groningen, The Netherlands. Before the start of any of the radiation experiment sessions, the produced proton beam has to be calibrated to obtain the amount of protons for each radiation take. The proton beam is sent through an ionisation chamber and aimed upon a scintillator which is connected to a PMT. The ionisation chamber is put on a high voltage, which results in a current signal when the proton beam passes through it. This signal is linearly proportional to the amount of protons that pass through the chamber. The signal is converted such that it is expressed in *Monitor Units*, MU. The scintillator with PMT on which the proton beam is aimed at, counts the amount of protons in the beam. By doing a series of six measurements, a linear fit between the amount of Monitor Units and actual amount of protons can be produced. This will result in a set value for protons per Monitor Unit(p/MU), which will be used to determine the amount of protons used per measurement take.

3.4 Predicted amount ^{12}N measurement

The amount of ^{12}N produced during an experiment can be predicted. In short, this is done by multiplying the cross-section of reaction 2.9 which turns the ^{12}C into ^{12}N with the amount of carbon atoms in the graphite target and protons from the beam hitting the graphite target. However, the cross-section of this reaction depends on kinetic energy of the protons travelling through the graphite. The kinetic energy decreases as it travels through the graphite, so the cross-section also changes throughout the graphite. Therefore, for the calculation of the amount of produced ^{12}N, the kinetic energy of the protons in each spot throughout the thickness of the graphite has to be calculated. This is done by numerically iterating over the Bethe formula.

3.4.1 Bethe formula

The Bethe formula calculates the mean energy loss per unit length of a charged particle travelling through a medium. There are various

different forms of the formula all depending on how many corrections due to relativistic and nuclear effects are needed. Taken from the book by Krane[13], the Bethe formula used in this thesis is:

$$-\left\langle \frac{dE}{dx} \right\rangle = 2\pi N_{Av} r_e^2 m_e c^2 \rho_t Z_p^2 \frac{Z_t}{A_t} \frac{1}{\beta_p^2} [\ln(\frac{2m_e c^2 \beta_p^2}{I^2(1-\beta_p^2)}) - 2\beta_p^2] \qquad (3.5)$$

where

- N_{Av} is Avogadro's number.
- r_e is the radius of the electron.
- m_e is the mass of the electron.
- c is the speed of light.
- ρ_t is the mass density of the target medium.
- Z_p is the atomic number of the travelling particle.
- Z_t is the atomic number of the target medium.
- A_t is the mass number of the target medium.
- β_p is the ratio between the speed of the travelling particle and the speed of light($\beta_p = \frac{v}{c}$).
- I is the mean excitation energy of the target medium.

Since only the irradiation of graphite by protons is considered, all variables except β_p can already be filled out. The density and mean excitation energy of graphite are 1.7 g/cm^3 and 78 eV respectively.[16] This leads to a simplified version of equation 3.5:

$$-\left\langle \frac{dE}{dx} \right\rangle = 0.13 MeV/cm \times \frac{1}{\beta_p^2} [\ln(13 \times 10^3 \frac{\beta_p^2}{1-\beta_p^2}) - 2\beta_p^2] \qquad (3.6)$$

Here the energy decrease per unit length is reduced to be solely dependant on the relativistic speed of the travelling protons.

3.4.2 Production of ^{12}N

In order to calculate the amount of produced ^{12}N, the cross-section at each point in path length of the proton beam through the graphite needs to be determined. For this, the kinetic energy of the protons at each point has to be calculated first. The kinetic energy of the protons at each point in the beam path is determined by a numerical procedure. The thickness of the graphite is divided in thin layers. As always with numerical calculation, the more and thinner layers, the more accurate the result is. For each layer, the following points are looped over:

- The β_p^2 of the entering protons is calculated. Since for this thesis the kinetic energy of the protons is low enough such that the classical formula for kinetic energy still holds:

$$E_{kin} = \frac{1}{2}mv^2 \tag{3.7}$$

  Rewriting this gives:

$$\beta_p^2 = \frac{v^2}{c^2} = \frac{2E_{kin}}{m_e c^2} \tag{3.8}$$

  Which is used to calculate the relativistic speed of the protons when the kinetic energy is known.

- The energy loss per layer is calculated by filling in the obtained β_p of the layer into the Bethe formula. The outcome of the Bethe formula is then multiplied by the layer thickness which results in the change in kinetic energy after the proton travels through the layer.

- The kinetic energy of the protons is then calculated by deducting this determined change in energy. This gives the kinetic energy of the protons in the next layer.

When the kinetic energy of the protons at each layer is determined, the cross-section can be found at each layer using a predetermined trend-line between kinetic proton energy and cross-section of the desired reaction. This thesis uses the results of Rimmer & Fisher [12]. With the cross-section of the production of ^{12}N per layer known, the production

of ^{12}N per unit length and thus in total can be calculated. The general formula for any nuclear reaction to occur in a homogeneous material per centimeter per incoming particle is

$$P_l = \sigma(E_{kin})\frac{\rho_t}{m_t}N_{av} \tag{3.9}$$

where

- $\sigma(E_{kin})$ is the cross-section corresponding to the kinetic energy of the incoming particle.
- ρ_t is the mass density of the target material in g/cm^3.
- m_t is the atomic mass of the target material in u.

The total production of ^{12}N in graphite is then calculated by plugging in the correct density and atomic mass into equation 3.9 and multiplying the result with the thickness of the graphite and the amount of protons sent into the graphite. When all these calculations have been performed, the total amount of ^{12}N that will be produced in an experiment can be determined. However, only a part of this total amount will be detected. Additional calculations have to be made in order to obtain a prediction for the amount of measured ^{12}N decays leading to a 4.4 MeV gamma.

3.4.3 Prediction count rate 4.4 MeV gammas

In order to predict the amount of 4.4 MeV gammas which the detector will measure, first the amount of ^{12}N nuclei which has not yet decayed when the detector starts measuring has to be determined. During the period when the proton beam is on, part of the produced isotopes already decays. For ^{12}N this is especially the case, since it has a very short lifetime related to the beam pulse duration. Therefore, the total amount of ^{12}N at the end of the beam period is lower than the total amount of produced ^{12}N. The amount of ^{12}N at the end of the beam period can be numerically determined by dividing up the beam period into small time domains of Δt. The production in each time domain in the beam period remains the same as long as there are no fluctuations in the proton beam intensity. The amount of ^{12}N in the n^{th} time domain

is a summation of the amount of ^{12}N produced in the time domains before the n^{th} time domain multiplied with their corresponding decay factor of how many time domains before the n^{th} time domain. This gives a product-summation of

$$N_n = P_0 e^{-\lambda n \Delta t} + P_1 e^{-\lambda (n-1) \Delta t} + \cdots + P_{n-1} e^{-\lambda \Delta t} + P_n \tag{3.10}$$

which can be shortend as

$$N_n = \sum_{k=0}^{n} P_k e^{-\lambda (n-k) \Delta t} \tag{3.11}$$

where P_k is the amount of ^{12}N produced in the k^{th} time domain. However, since the assumption is that this production per time domain is constant, P_k is the same for every k. Therefore, P_k can be denoted as just P, which will be the total amount of ^{12}N produced divided by the amount of time domains. Since the number of time domains is the total beam time, t_{beam}, divided by the size of the time domain, Δt, this gives

$$P = \frac{P_{total}}{\frac{t_{beam}}{\Delta t}} = \frac{P_{total}}{t_{beam}} \Delta t \tag{3.12}$$

so that the amount of ^{12}N in the n^{th} time domain is

$$N_n = P \sum_{k=0}^{n} e^{-\lambda k \Delta t} \tag{3.13}$$

Although the summation is already implementable in any script, it can also be evaluated as a geometric series. Recall that a finite geometric series is written as

$$\sum_{n=0}^{N} r^n = \frac{1 - r^{N+1}}{1 - r} \tag{3.14}$$

By noting that

$$e^{-\lambda k \Delta t} = (e^{-\lambda \Delta t})^k \tag{3.15}$$

equation 3.13 can be written as

$$N_n = P \sum_{k=0}^{n} (e^{-\lambda \Delta t})^k \tag{3.16}$$

Using the substitution

$$r = e^{-\lambda \Delta t} \tag{3.17}$$

the geometric series can be applied to obtain an expression for the amount of ^{12}N in the n^{th} time domain during the beam period

$$N_n = P \frac{1 - e^{-\lambda(n+1)\Delta t}}{1 - e^{-\lambda \Delta t}} \tag{3.18}$$

The amount of ^{12}N at the end of the beam period can then be calculated by filling in the last time domain l for n.

The amount of ^{12}N at the end of the beam period can also be analytically calculated. The analytical approach is obtained when turning the product-summation 3.11 into an integral. Fully written out, this product-summation is

$$N_n = \sum_{k=0}^{n} \frac{P_{total}}{t_{beam}} e^{-\lambda(n-k)\Delta t} \Delta t \tag{3.19}$$

by taking the limit $\Delta t \to 0$ and noting that $(n - k)\Delta t = t$ in the continuous limit, the following integral is obtained

$$N_{t_n} = \frac{P_{total}}{t_{beam}} \int_0^{t_n} e^{-\lambda t} dt \tag{3.20}$$

which gives the amount of ^{12}N at time t_n within the beam period. The amount of ^{12}N at the end of the beam period is calculated by plugging in t_{beam} as t_n. This results into the final analytical expression of the amount of ^{12}N at the end of the beam period.

$$N_{t_{beam}} = \frac{P_{total}}{\lambda t_{beam}} (1 - e^{-\lambda t_{beam}}) \tag{3.21}$$

Here equation 3.21 is also the outcome of equation 3.18 when Δt is taken to zero and filling in l for n.

$N_{t_{beam}}$ denotes the amount of ^{12}N after the beam is switched off. In the situation where the detector is not pulsed in synchronisation with switching off the proton beam, the detector will be measuring during the beam period. This will result in the detector being saturated such that the detector needs a few milliseconds to recover. This is the situation for the two experimental sessions. Within this recovery period $t_{recovery}$, the decay of ^{12}N will also have to be considered. The detector will start to provide data of good quality after recovery. The amount of ^{12}N after recovery, and thus the amount of ^{12}N at the moment where the detector starts measuring, is

$$N_{after\ recovery} = N_{t_{beam}} e^{-\lambda t_{recovery}} \tag{3.22}$$

The last two steps are calculating how much ^{12}N decays during the time period where the detector is measuring and how many of those decays result in measurements. The amount of decays during the entire time period of measuring, t_m, is the difference between the amount of isotopes at the start and the end of the time period.

$$\Delta N_m = N(t = 0) - N(t = t_m) \tag{3.23}$$

Since

$$N(t_m) = N(0)e^{-\lambda t_m} \tag{3.24}$$

equation 3.23 becomes

$$\Delta N_m = N(0)(1 - e^{-\lambda t_m}) \tag{3.25}$$

where for this situation, $N(0)$ is the amount of ^{12}N left over after the recovery period, $N_{after\ recovery}$. This results in the amount of ^{12}N decays during the time period of measuring.

However, not all ^{12}N decays will result in a measurable 4.4 MeV gamma and not all 4.4 MeV gammas will be measured. To obtain the final result of how many 4.4 MeV gammas will be measured, the amount of ^{12}N decays during the measuring time will have to be multiplied with two factors:

- The branching ratio, B, since only a small fraction of the ^{12}N decays will result in a 4.4 MeV gamma. The branching ratio for decays resulting into 4.4 MeV gammas is $B = 0.019$.

- The effective effiency of the detector, ϵ. The 4.4 MeV gammas will be emitted in every direction, so only a small fraction of all emitted 4.4 MeV gammas will hit the detector. This is determined by the size and the distance of the detector from the target. Additionally, also the fact that some of the 4.4 MeV gammas that do hit the detector will not be measured due to inherent inefficiency of the detector itself has be taken into consideration.

So the detected amount of 4.4 MeV gammas from the decay of ^{12}N, N_γ, is

$$N_\gamma = B\epsilon\Delta N_m \tag{3.26}$$

Tracing back all these steps and putting them in one expression gives

$$N_\gamma = B\epsilon\frac{P_{total}}{t_b}e^{-\lambda t_r}(1-e^{-\lambda t_b})(1-e^{-\lambda t_m}) \tag{3.27}$$

where t_r, t_b and t_m are the time for recovery, beam-on and measurement respectively. This gives a prediction for the amount of measured 4.4 MeV gammas disregarding any uncertainties. In the opposite situation, where the amount of 4.4 MeV gammas is measured and the total amount of produced ^{12}N during the experiment needs to be determined, equation 3.27 can be inverted to obtain

$$P_{total} = \frac{N_\gamma}{B\epsilon}\frac{e^{\lambda t_r}}{(1-e^{-\lambda t_b})(1-e^{-\lambda t_m})}t_b \tag{3.28}$$

Chapter 4

Materials & Methods

4.1 Detector setup specifications

The detector setup, or detector in general, has a common setup for the two experimental sessions. A NaI-detector encased in a BGO-detector which functions as an anti-Compton shield.

4.1.1 NaI-detector

The NaI-detector consist of a 91 mm x 91 mm x 150 mm block of a NaI crystal, enveloped in aluminium of 1 mm thick, connected to a PMT. The official name of the NaI-detector is the *Scintillation Detector Type V91A150/3M-E1* by Scionix. See figure 4.1 for a picture and figure 4.2 for the technical drawing of the NaI-detector.

4.1.2 BGO-detector/anti-Compton shield

The NaI-detector is inserted in an aluminium case. The aluminium case contains four BGO-detectors per side, totalling up to sixteen detectors. These sixteen BGO-detectors inside the aluminium case are connected to a voltage divider, which is carefully configured such that the sixteen detectors are synchronised in calibration. The sixteen detectors are connected to each other so it gives one collective signal to the DAQ, turning the sixteen detectors in one larger BGO-detector. The aluminium case together with the BGO-detector is the anti-Compton shield. Part of the case is sloped towards a tungsten collimator. This collimator is to prevent direct radiation upon the BGO-detector from

the source. This is the front of the detector facing the graphite target. See figures 4.3 and 4.4 for pictures of the BGO-detector and 4.5 for its technical drawing.

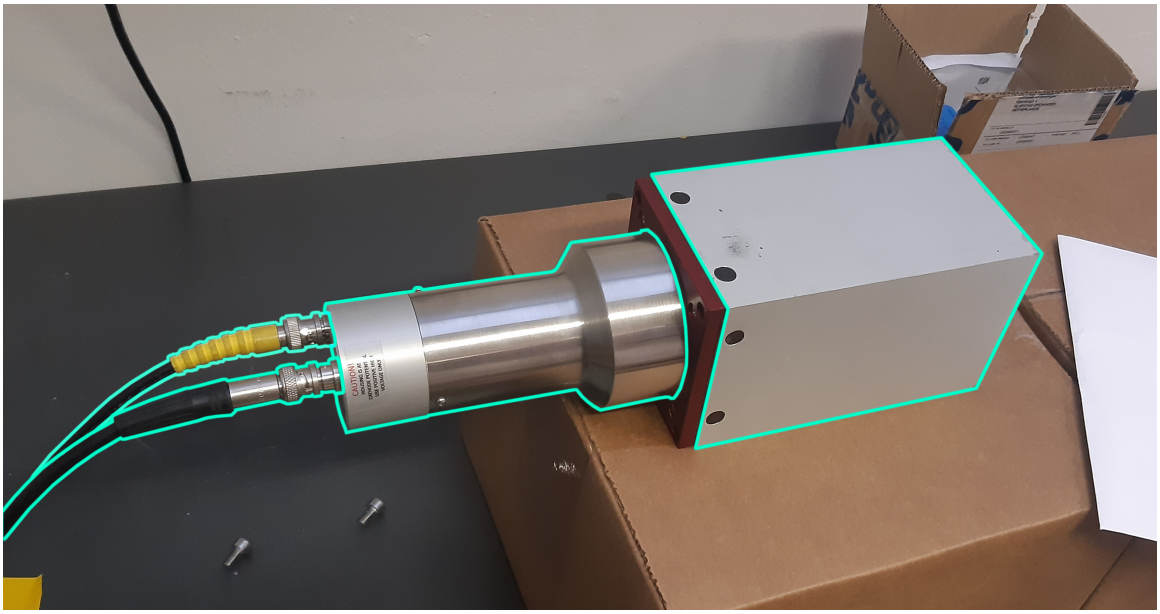

Figure 4.1: Picture of the NaI-detector with the components outlined. During the first two sessions, this NaI-detector was inserted in the anti-Compton shield.

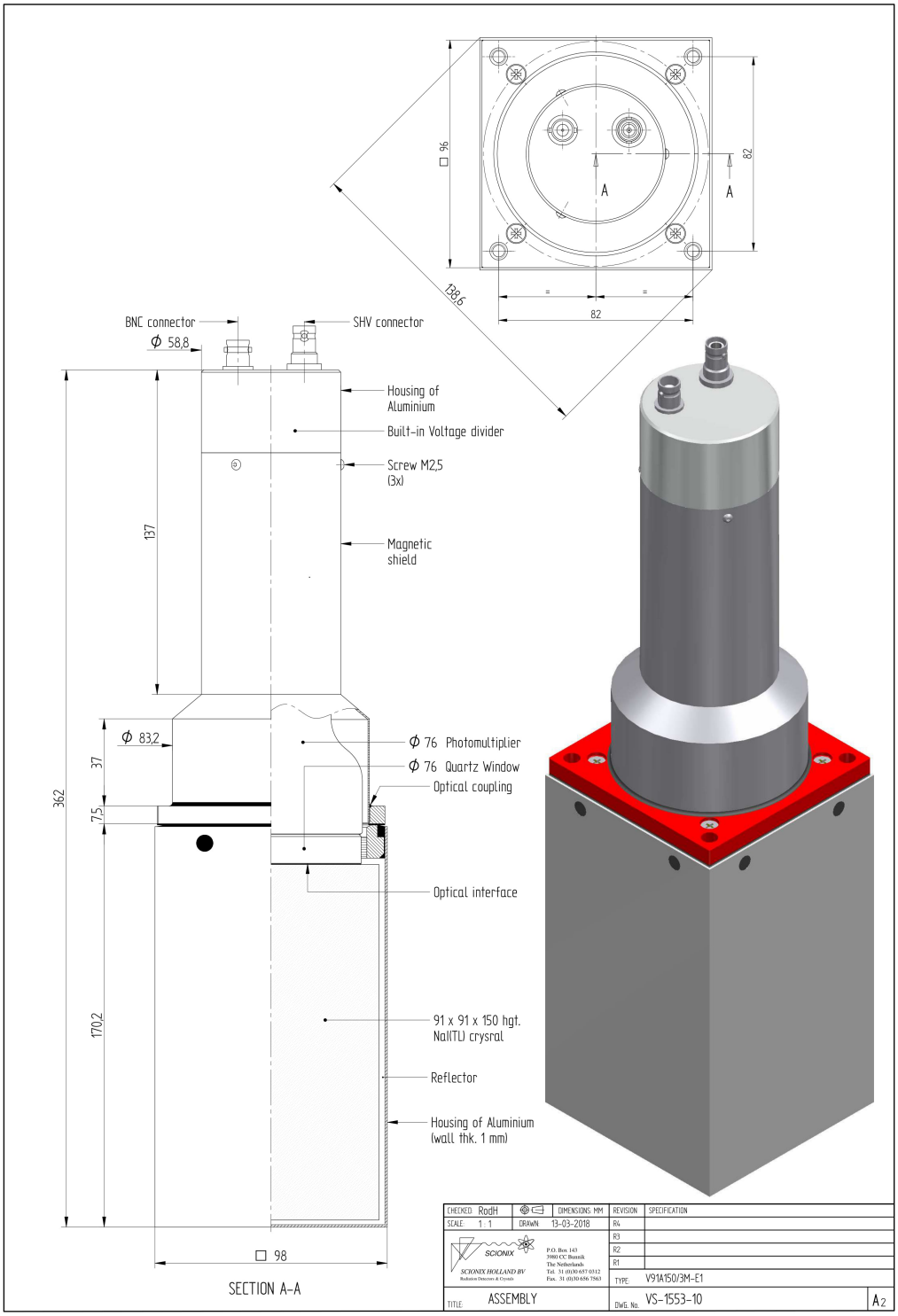

Figure 4.2: Technical drawing of the NaI-detector used in the first two sessions.

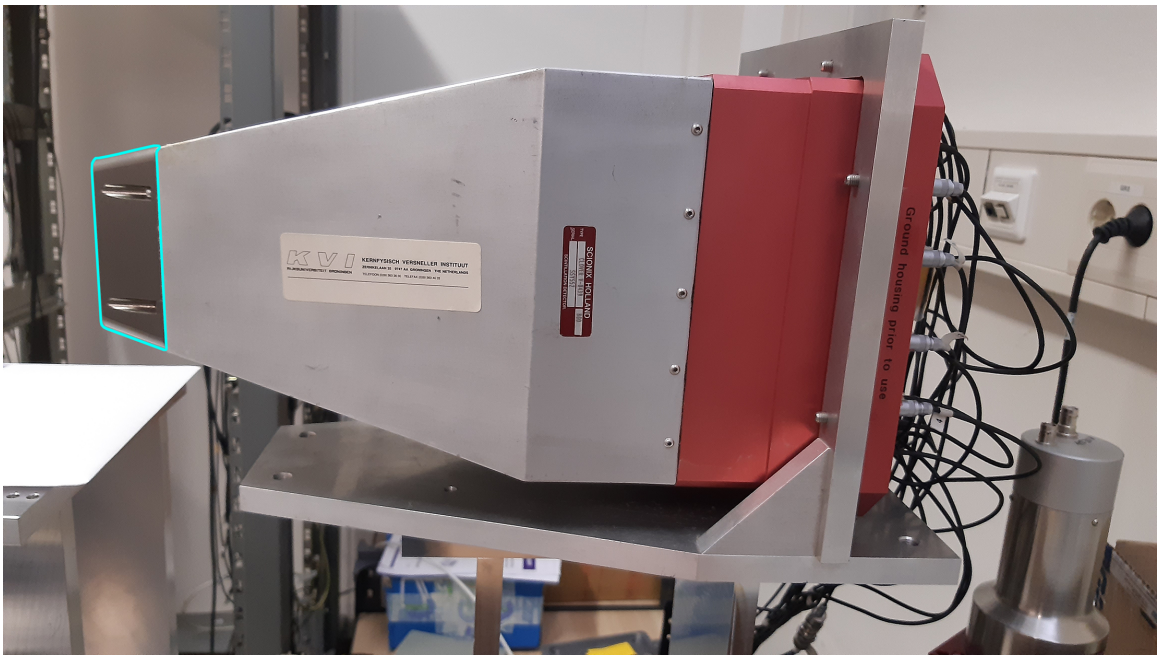

Figure 4.3: Side view picture of the anti-Compton shield with the tungsten collimator highlighted.

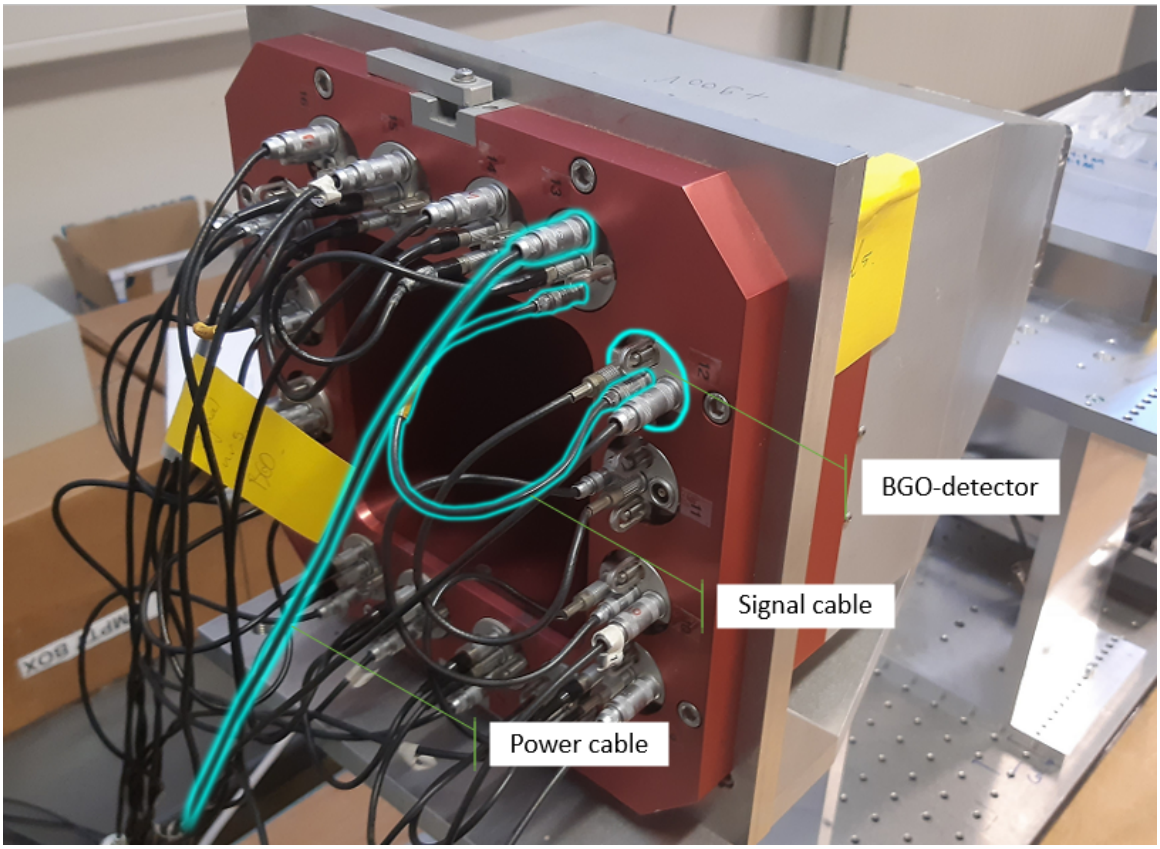

Figure 4.4: Back view picture of the anti-Compton shield.

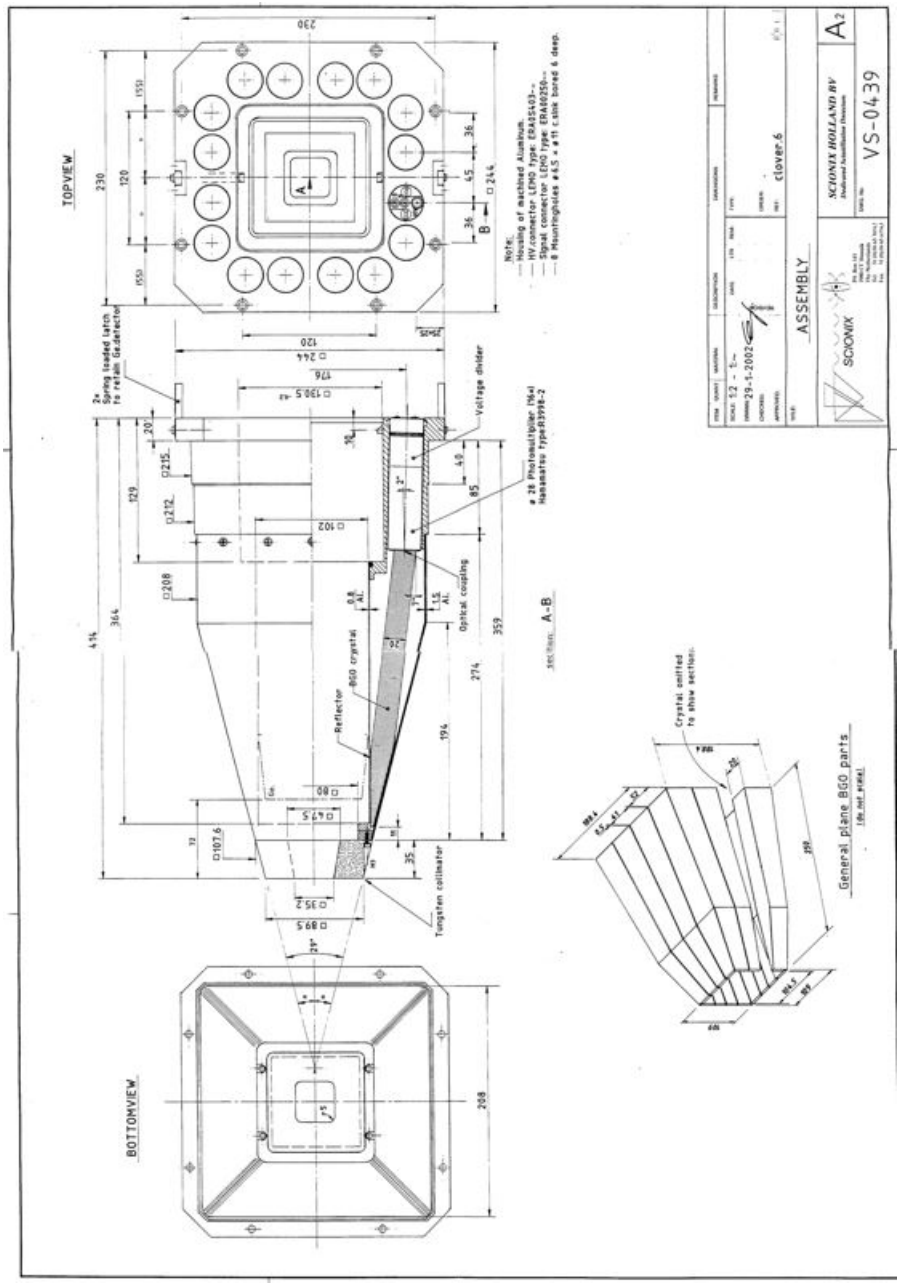

Figure 4.5: Technical drawing of the anti-Compton shield which houses the BGO-detector used in the first two sessions.

4.1.3 Data acquisition

The signals given by both the NaI- and BGO-detector are collected by a data acquisition system(DAQ) which consists of a MDPP-16 device. This device analyses and converts the recieved signals from the detectors into a digital signal sent to the computer of the user. These digital signals are then processed by the software *mvme*. Both the MDPP-16 and mvme is from the company *mesytech*.[19] When mvme obtains a signal from an event, it first checks if it meets the conditions for being valid. Such a condition can be meeting a certain energy threshold. When an event is obtained by mvme, the following three properties of the event are noted:

- From which detector the events comes.
- At what time the event arrives according to the given clock. This arrival time is noted as the *timestamp* of the event.
- What energy the event is according to the given calibration parameters.

The timestamp of an event depends on the given clock. Without a given clock, this timestamp becomes the so called wall time, the time at the laboratory. A given, custom clock is used during the experimental sessions as the proton beams are pulsed in a beam time cycle of 10% on/90% off. During the sessions, the DAQ is connected to a pulse generator which creates these beam time cycles. The timestamp then becomes the time within the 50ms beam time cycles. mvme provides possibilities of setting conditions upon the listmodes of events which create useful data. There are numerous conditions and combinations thereof used in this thesis, whereby the most essential are:

- The condition that an event that is measured in both the NaI-detector and the BGO-detector with almost the same timestamp will be removed. This is because a gamma that is measured by both detectors at the same time is highly likely to be Compton scattered.
- The condition of only noting events after a certain time mark. This is used for looking at events within the beam time cycle that are

from after either the beam on period or the recovery period. This filters out the events taken during these periods, giving a clearer gamma spectrum.

4.2 Source measurements

In preparation to the experiments where graphite is irradiated by the cyclotron, it is important to first observe the behaviour of the detector itself. These preparational measurements are performed using a radioactive ^{22}Na- and ^{68}Ge-source, see figure 4.6. ^{22}Na emits gammas of 511 keV and 1275 keV as shown in spectrum . ^{68}Ge is purely a positron emitter and thus only produces gammas of 511 keV. Besides preparational measurements using long-living sources, a zinc plate was irradiated in order to produce a ^{66}Ga-source for high energy calibration.

Figure 4.6: ^{22}Na-source and ^{68}Ge-source used for this thesis with coin for scale.

4.2.1 Translational movement

Ideally the detector target is perfectly in front of the detector. However, it is important to see if a deviation on the axis orthogonal to the line-of-sight of the detector impacts the radiation detection. If a small deviation already severely impacts the detection quality, then this has to be taken into consideration when reconstructing the detector setup in the radiation room. To test how sensitive the detection efficiency is to translational deviation, an energy spectrum of the ^{22}Na-source is taken for one minute multiple times. The first measurement is taken when the ^{22}Na-source is placed on this orthogonal axis, 50 mm starboard side of the detector, considering the direction of the detector the fore. See figure 4.7 for a drawing of the setup. The ^{22}Na-source is moved in steps of 5 mm towards the port side after each measurement until it is 50 mm on the other side.

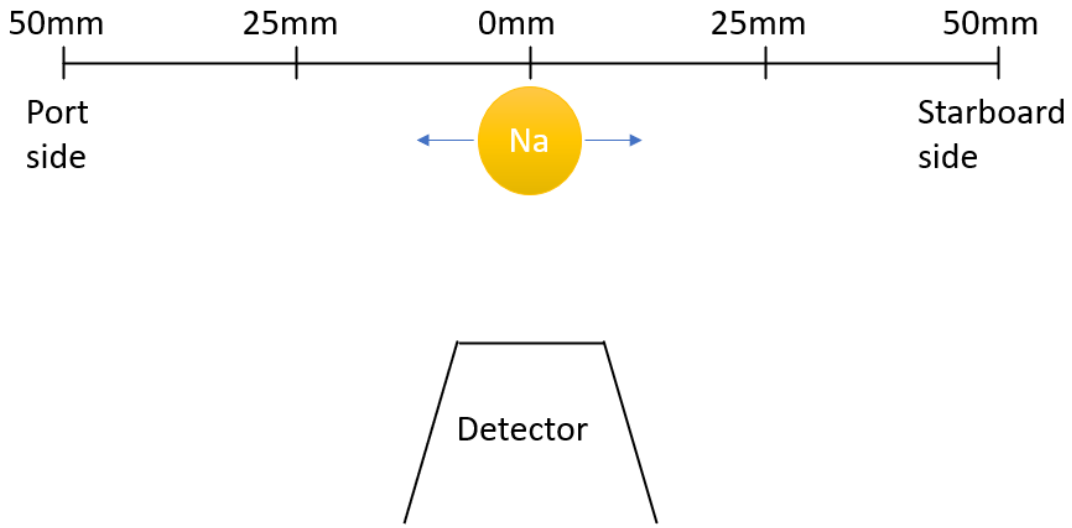

Figure 4.7: Drawing of the translational movement test. The ^{22}Na-source is moved to both sides in steps of 5 mm and the loss in counts is noted.

4.2.2 Dead time & summing

When a detector obtains a measurement event, it requires some time to be ready to process another event as a separate event. This amount of time a detector needs is called the *dead time* of a detector. The detector can miss events during dead time due to the random nature of radioactive decay. The dead time of the NaI-detector for example is of the order of a few microseconds. Another related phenomenon which can occur is *summing*. Summing happens when two, or unlikely more, gammas enter the scintillator at around the same time. The detector cannot discriminate between these two measurements and notes them as one event, summing their energies. For example, two 511 keV gammas from positron emitters can be measured at the same time, resulting in a peak at 1022 keV in the gamma spectrum. To test whether these phenomena significantly affects the detector, both the ^{22}Na- and ^{68}Ge-sources are placed in front of the detector. The ^{22}Na-source is placed at a fixed distance from the detector while the ^{68}Ge-source is moved at various distances from the detector. For every different location of ^{68}Ge-source, a gamma spectrum is taken for one minute. See figure 4.8 for a drawing of the setup. The focus is on the 1275 keV peak produced by the ^{22}Na-source. As the ^{68}Ge-source moves closer, the detector would be in a dead time state more often due to a higher intensity of 511 keV counts. This would then cause the detector to lose 1275 keV counts. Another focus is on the occurrence of peaks caused by summing. These peaks are 1022 keV(2$\times$ 511 keV) and 1786 keV(1275 keV + 511 keV).

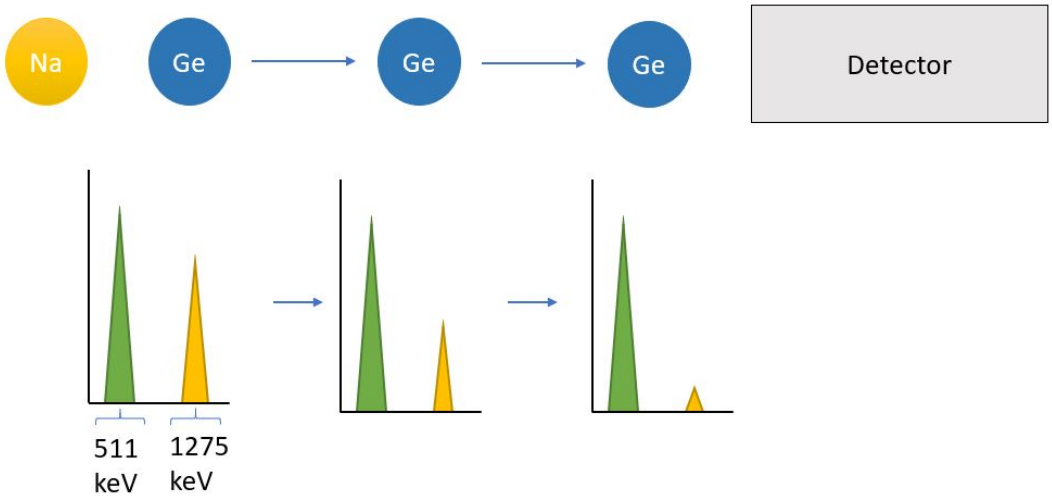

Figure 4.8: Schematic drawing of testing on dead time. As the ^{68}Ge-source moves closer, the 1275 keV peak will decrease in intensity relative to the 511 keV peak. A significantly severe drop in the 1275 keV intensity indicates an intensity limit of the NaI-detector.

4.3 Proton radiation experimental sessions

For this thesis, two experiment sessions are performed where graphite is irradiated by a proton beam and an attempt is made to measure the produced ^{12}N. Both sessions have a very similar experimental setup and settings, with some alterations to the target for session 2. During each session, a zinc plate was irradiated with the proton beam in order to produce a ^{66}Ga-source for calibration.

4.3.1 Experimental session 1

The kinetic energy of the proton beam is set at 90 MeV. The cyclotron is calibrated at 1992 p/MU. The beam time cycle is set at 10 ms beam on, 90 ms beam off. A target consisting of two graphite plates of 0.5 mm, so together 1mm, is held in a water basin. The water is held in a plastic bag to accommodate the replacement of water. The detector is pointed towards the target with a distance of 17 cm between the target and the tungsten collimator. The window of the water basin facing the

proton beam has a thickness of 2.1 mm. The water basin and graphite holder are both connected to movable stages. This setup is such that the amount of water between the target and the water basin entrance side can be increased and decreased. In addition, the movement of the water basin in direction is compensated by movement of the graphite holder in the other direction. The displacements in opposite direction results in the graphite target always being in front of the The changing of the path length the beam takes in water makes it possible to change the proton energy hitting the target during the experiment. Here the water acts as a degrader. A series of six measurements are taken during the irradiation of the water basin setup. Long-living isotopes are also produced in the water during irradiation. These are ^{15}O($\tau_{\frac{1}{2}}$ =2 min) and ^{11}C($\tau_{\frac{1}{2}}$ =20 min). To prevent distorting by these isotopes, the water is refreshed twice for the last two measurements. See table 4.1 for a summary of the irradiation takes.

Table 4.1: Irradiation time, MU and proton counts of proton radiation of experiment session 1 upon 1 mm graphite target in water basin.

Nr.	Irradiation time(s)	MU	Proton count	Remarks
1	50	3.48E+06	6.93E+09	Proton intensity too high for the detector
2	300	7.64E+04	1.52E+08	
3	60	2.23E+05	4.44E+08	
4	600	1.73E+06	3.45E+09	
5	300	2.25E+06	4.48E+09	Beam turns off for a moment after 1.5 minutes
6	420	2.86E+06	5.70E+09	

4.3.2 Experimental session 2

The kinetic energy of the proton beam is set at 90 MeV. The cyclotron is calibrated at 1973.3 p/MU. The beam time cycle is set at 5 ms beam on, 45 ms beam off. The goal of session 2 is to focus on the detection of ^{12}N in general. This means no changes in path length of the proton beam through the degrading material. The target in session 2 is a 5.2 mm thick graphite block. The target is not held in water, but suspended in air. A series of four proton irradiations are performed upon the target. The target is refreshed for each irradiation. As a degrader, a 50 mm thick polystyrene (PS) block is used. One irradiation is performed without a degrader. The details are listed in table 4.2. During the session, it became quickly noticeable that the thermal neutrons produced by the proton beam activates the material of the detector itself, heavily contributing to background radiation. A more detailed discussion of the detector material activation is in section5.3

Compared to session 1, the target is thicker and the beam on period is halved in session 2. This is to maximise the production and measurement of ^{12}N as session 1 did not show any production of ^{12}N.

Table 4.2: Experiment 2, measurement times and proton counts of proton radiation upon 5.2 mm graphite target with PS degrader.

Nr.	Measurement time(s)	MU	Proton Count	Remarks
1	1800	5.27E+07	1.04E+11	No degrader
2	1800	4.91E+07	9.69E+10	Some break due to RF problems
3	1800	4.98E+07	9.82E+10	BGO turned off
4	1800	1.79E+07	3.53E+10	Intensity set at 1/3 of previous intensity

Chapter 5

Results

5.1 Source measurements

5.1.1 Translational movement test

The results show that there is almost no loss in counts if the source is within 35 mm of translation distance from the centre. See table 5.1 and figures 5.1 and 5.2 When the distance of the target source goes beyond 35 mm, then the count rate starts to drop. At the far ends of the measurements, 50 mm, the count rate becomes 90% of the count rate when the target source is in the centre. This shows that the original detector setup allows some translational deviation up to around 3 cm from the centre of the detector's line of sight without loss in counts. In addition, deviation up to 5 cm will not result in a measurable, but not severe loss in counts. The fact that the behaviour in loss of counts is the same in both directions also shows that there are no asymmetrical oddments in the detector.

Table 5.1: The peak intensities of the 511 keV and 1275 keV peaks at the centre and the far ends of the translational test.

511 keV peak 22Na position	Counts	Error	Relative to centre
50 mm starboard	9,44E+04	3,00E+02	87%
center	1,09E+05	3,00E+02	100%
50 mm port	9,11E+04	3,00E+02	84%
1275 keV peak **22Na position**	**Counts**	**Error 1275 keV**	**Relative to centre**
50 mm starboard	4,05E+04	2,00E+02	82%
center	4,92E+04	2,20E+02	100%
50 mm port	4,05E+04	2,00E+02	82%

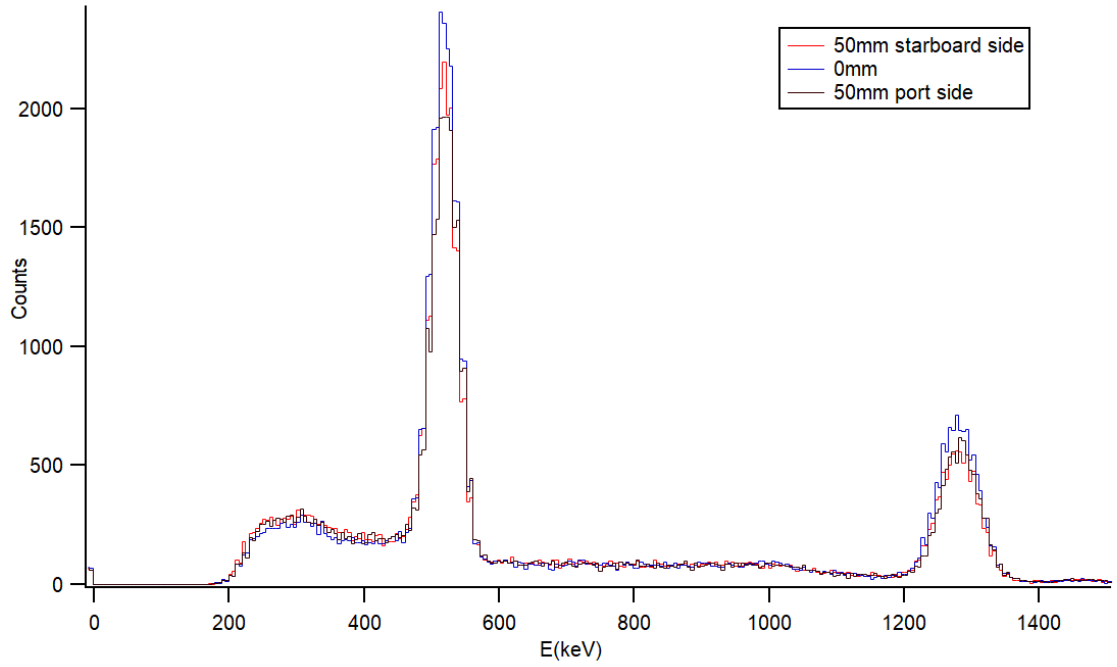

Figure 5.1: Three spectra where the ^{22}Na-source is right in front of the detector and on both translational ends of 50mm.

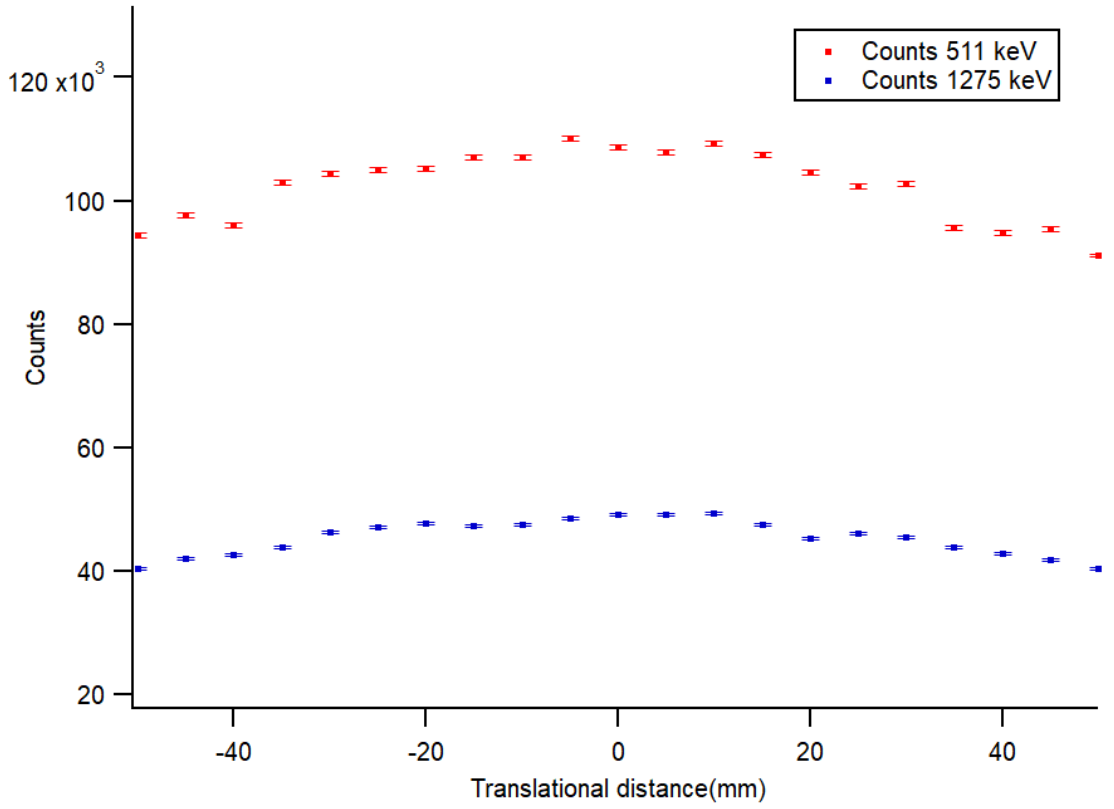

Figure 5.2: Graph of the translational distance from the centre versus the amount of counts of both 511 keV and 1275 keV peak. The negative distance corresponds with the port side direction. The graphs shows that after a deviation in distance of about 3cm, the amount of counts starts to drop measurably.

5.1.2 Dead time & summing

Seven spectra were taken whereby the ^{68}Ge-source is moved closer to the detector while the ^{22}Na-source remains at a fixed location. One of spectra was taken without a ^{68}Ge-source. See figure 5.3 for the gamma spectra. The ^{68}Ge-source was inside the collimator for the measurement at distance 0cm and 2.5cm. The highest count rate achieved was when the ^{68}Ge-source is against the detector with a count rate of circa 100 000 events per second.

The influence of dead time becomes noticable at the 1275 keV peak. A perfect detector with zero dead time would not lose 1275 keV counts as the count rate increases. However, the 1275 keV peak decreases in intensity as the ^{68}Ge-source moves closer. The intensity of the 1275 keV decreases with about 5% when the ^{68}Ge-source is outside the collimator and drops with 10% of the original intensity as the ^{68}Ge-source moves inside the collimator. This shows dead time interfering with the measurement. The 1022 keV and 1786 keV summing peaks prominently occur in the spectra. The 1022 keV peak increases from 1.3% of the amount of corresponding 511 keV counts to 2.4% as the ^{68}Ge-source is moved from 13cm to 0cm from the detector. Similarly for 1786 keV, the ratio between 1786 keV counts to 511 keV counts goes from 0.08% to 0.12% as the ^{68}Ge-source moves closer. The consequences of both dead time and summing are noticeable as the ^{68}Ge-source is moved closer to the detector. At the highest count rate of 100 000 counts per second, a loss due to dead time occurs of about 10%. Nevertheless, the losses in counts are still small enough to warrant proper quality gamma spectrum measurements up to an count rate of 100 000 counts per second.

An unexpected photopeak starts to rise in the gamma spectra in figure 5.3 as the ^{68}Ge-source is close or inside the collimator within the energy domain of 660-760 keV. A possible explanation for this peak is that is caused by summing a regularly emitted 511 keV gamma with a 511 keV gamma which is Compton-scattered into the direction of the detector. A 511 keV gamma which is 180 degrees backscattered has, according to equation 2.10, 170 keV. The energy of a scattered 511 keV gamma

can also be more if the scattering angle is less. The summation is then $511 + 170 = 681$ keV, which corresponds with this peak.

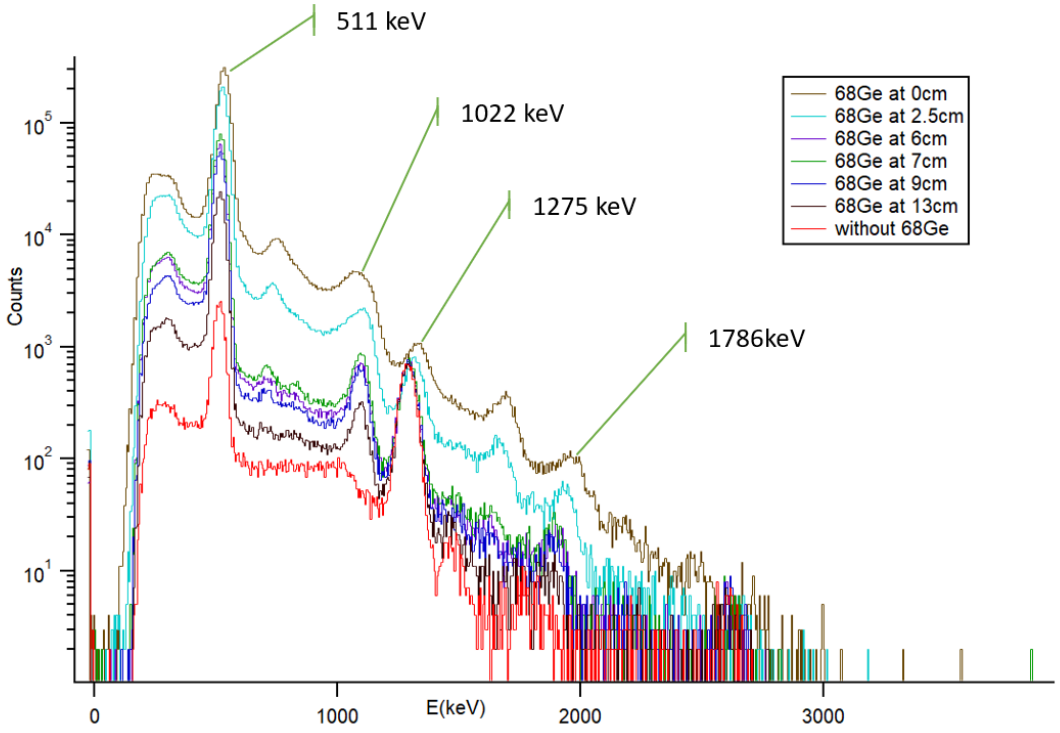

Figure 5.3: Gamma spectra of the ^{22}Na- and ^{68}Ge-sources whereby the ^{68}Ge-source is moved closer. Distances with respect to the NaI-detector.

5.1.3 ^{66}Ga

During each session, a zinc plate was irradiated to produce a temporary ^{66}Ga-source. A calibration usable for high energies gamma spectroscopy is made using the six energy peaks with the highest relative intensities, listed in table 5.2. The resulting gamma spectrum is show in figure 5.4

Table 5.2: The gamma energy peaks of ^{66}Ga with the highest relative intensity. These values are used to identify the peaks in the spectrum of ^{66}Ga in order to obtain a high-energy calibration.

Gamma energy(keV)	Relative intensity
833.5324	15.92
1039.22	100
2751.84	61.34
4085.85	3.455
4295.22	10.25
4806.01	5.04

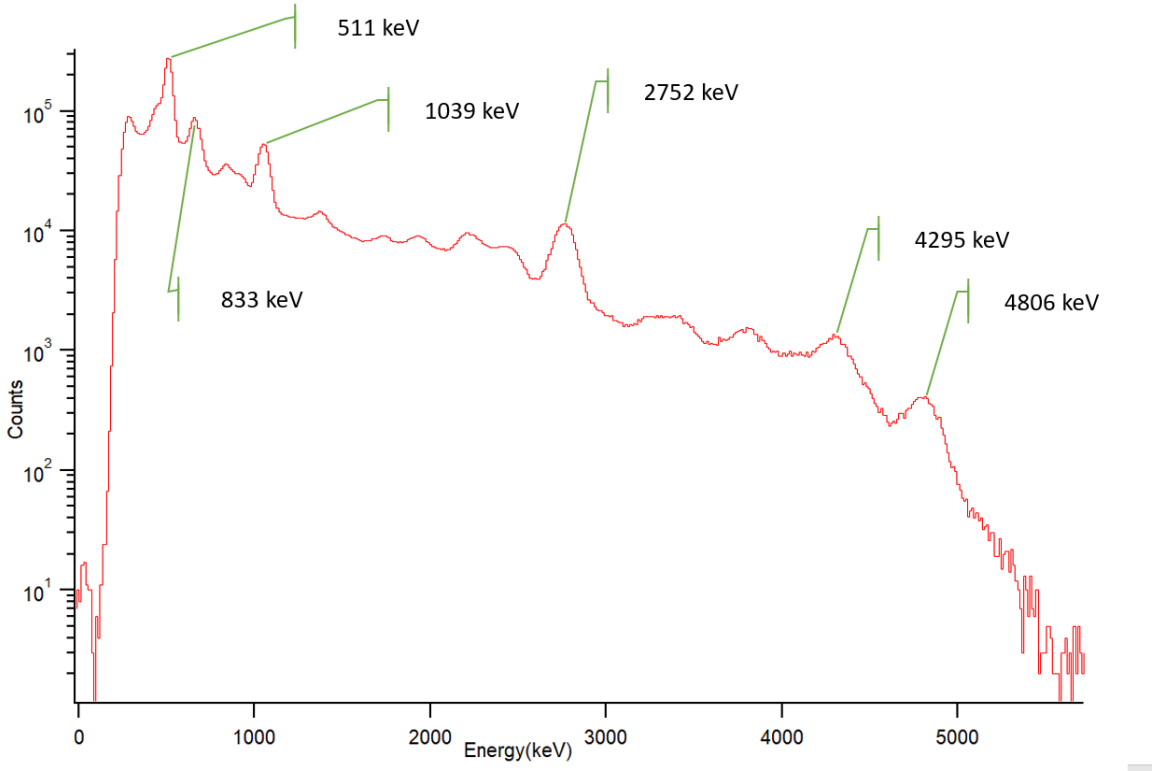

Figure 5.4: Gamma spectrum of ^{66} Ga with the six peaks as listed in table 5.2 labelled.

5.2 Proton irradiations

No evidence of the production of ^{12}N was found in the experimental session 1. During experimental session 2, whereby the graphite target was 5.2 mm instead of 1 mm, one proton irradiation showed signs of the production of ^{12}N. See figure 5.2 for the obtained spectrum and figure 5.6 for a bump in the spectrum which is suspected to come from ^{12}N. A condition was applied on the data such that, within a pulse, the beam-on and the recovery period are ignored. For session 2 with a period of 50 ms; 5 ms beam-on, 45 ms beam-off, this condition ensures that events between 5 ms to 25 ms are ignored. The recovery period is 14 ms long, which means $1 - \frac{1}{2}^{\frac{14}{11}} \approx 59\%$ of the ^{12}N since the end of the beam-on period has already decayed. A linear fit is applied on the region indicated by figure 5.6 with the points of the suspected bump to be ignored. The number of counts within this bump is determined by summing the counts above the fitted line. See figure 5.7 for a sketch about what is meant with a linear fit and counting the bump. This results in a determination of 2.0E+03 ± 5.4E+02 counts inside the bump.

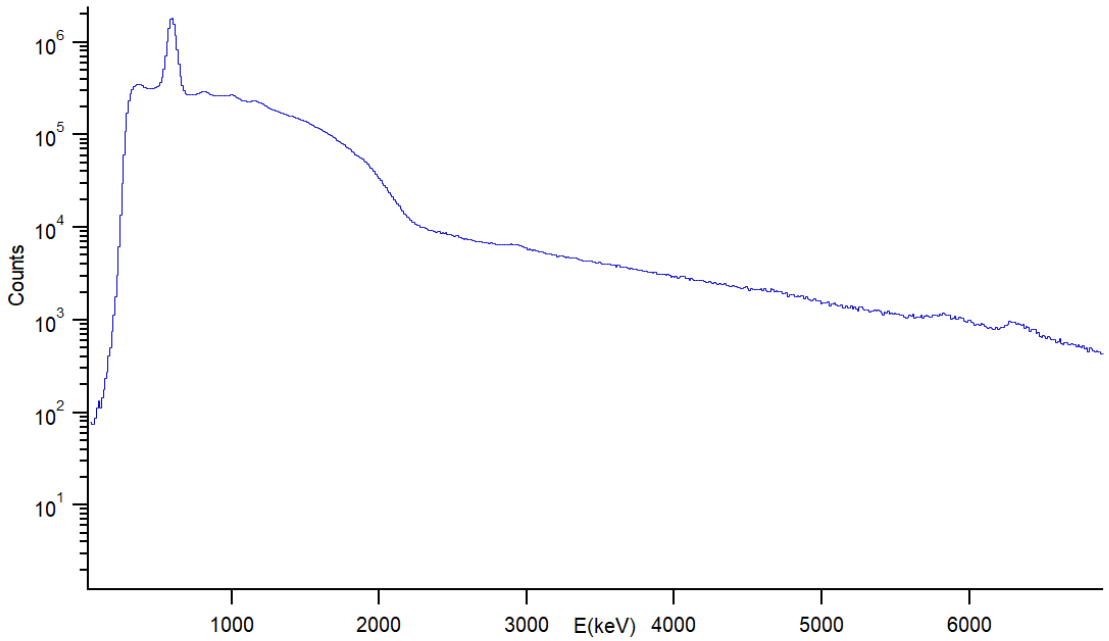

Figure 5.5: The gamma spectrum of the 5.2 mm thick irradiated graphite target with the condition that the events during the beam on and recovery period are ignored.

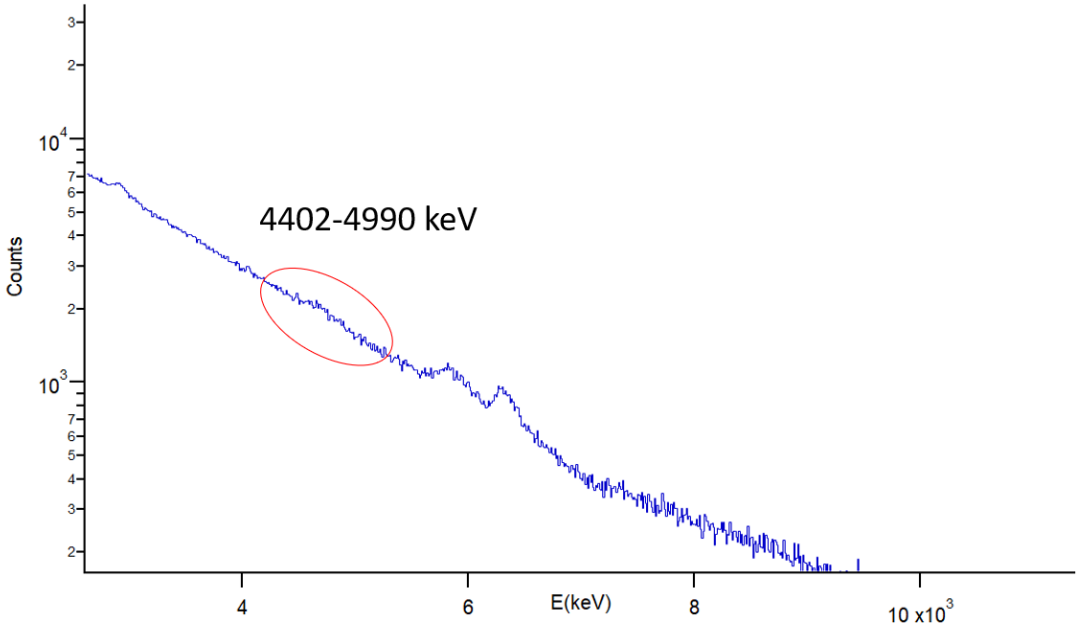

Figure 5.6: Zoomed in gamma spectrum of figure 5.2. A labelled bump appears in the spectrum in the energy domain of 4402-4990 keV which could be from 4.4 MeV gammas emitted from ^{12}N-decay.

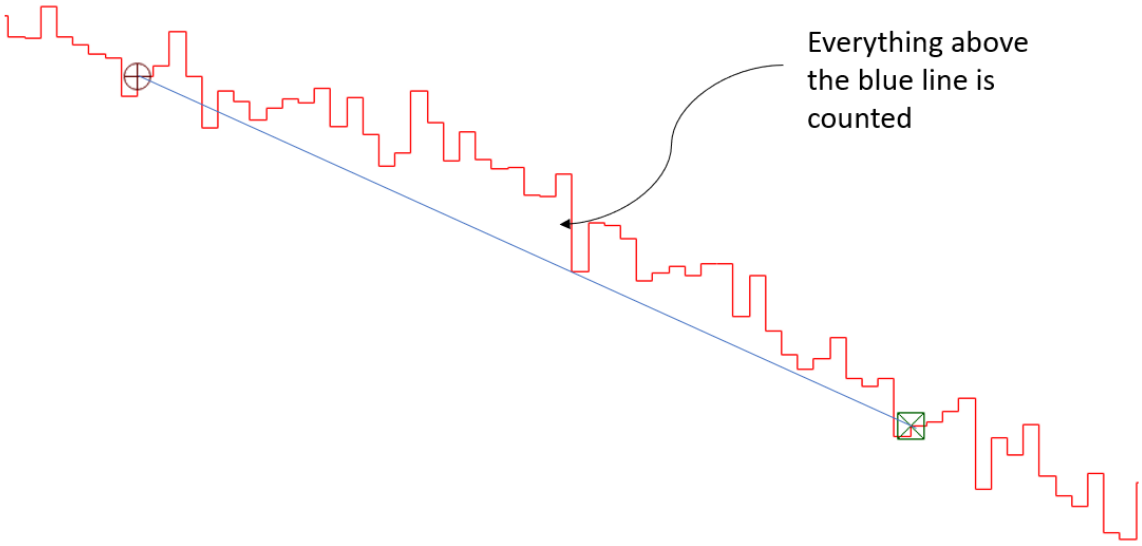

Figure 5.7: Drawing indicating the counting method applied on bumps in the gamma spectrum which is not describable with a Gaussian fit.

5.2.1 Energy correction

A method of implementing an energy correction which depends on the time within a single pulse has been developed. The context is that right after the beam-on period, the given calibration parameters do not correspond with the physical condition of the detector. During the recovery period, the detector converts back to its original state over time whereby the calibration parameters are valid again. The developed method is to implement a correction for the measured energy values to compensate this deviation. The parameters of this energy correction change with respect to time during the recovery period such that the value for energy is almost always correct for each moment in the beam-off period. See figures 5.8 and 5.9 for the energy-timestamp matrices before and after such a time-dependent energy calibration. The fit for the correction was found by multiplying the given value for energy with a scaling factor such that the lines on the energy-timestamp matrix becomes as straight as possible. The outcome would be the corrected value for energy. This results in:

$$E_{\text{after correction}} = \frac{E_{\text{before correction}}}{1 + Ae^{-Bt}} \times \frac{1}{1 + C(45 - t)} \tag{5.1}$$

whereby:

- t is the time of the timestamp in milliseconds.
- A, B & C are free parameters ad hoc adjusted such that the lines on the energy-timestamp matrix become straight.

For the discussed irradiation take, the found parameters A, B and C are 1.05, $\frac{1}{5}$ and 0.001 respectively, resulting in the following scaling factor:

$$\frac{1}{1 + 1.05e^{-\frac{t}{5}}} \times \frac{1}{1 + C(45 - t)} \tag{5.2}$$

Another notable implemented change is the shift in the beam-on period to the end of the matrix. Purely for read-out convenience, in figure 5.9 0 ms to 45 ms is when the beam is off in a single time cycle. The recovery period can now be reduced to 6 ms, as the data in those six milliseconds is too noisy to adjust. By pushing the recovery period

down to 6 ms, only $1 - \frac{1}{2}^{\frac{6}{11}} \approx 31\%$ of the amount of ^{12}N right after irradiation will have decayed. That is 28% more ^{12}N to be measured compared to no energy correction.

After the energy correction, three peaks over >4 MeV become apparent. These peaks appear in the spectrum in figure 5.10 and are labelled in figure 5.11 with the energy domain of each peak denoted. The energy domains of these peaks are:

- Peak 1: 4379 keV - 4679 keV
- Peak 2: 5513 keV - 5880 keV
- Peak 3: 6008 keV - 6386 keV

Peak 2 seems to be the escape peak of peak 3 as the peak 2 is 511 keV lower than peak 3.

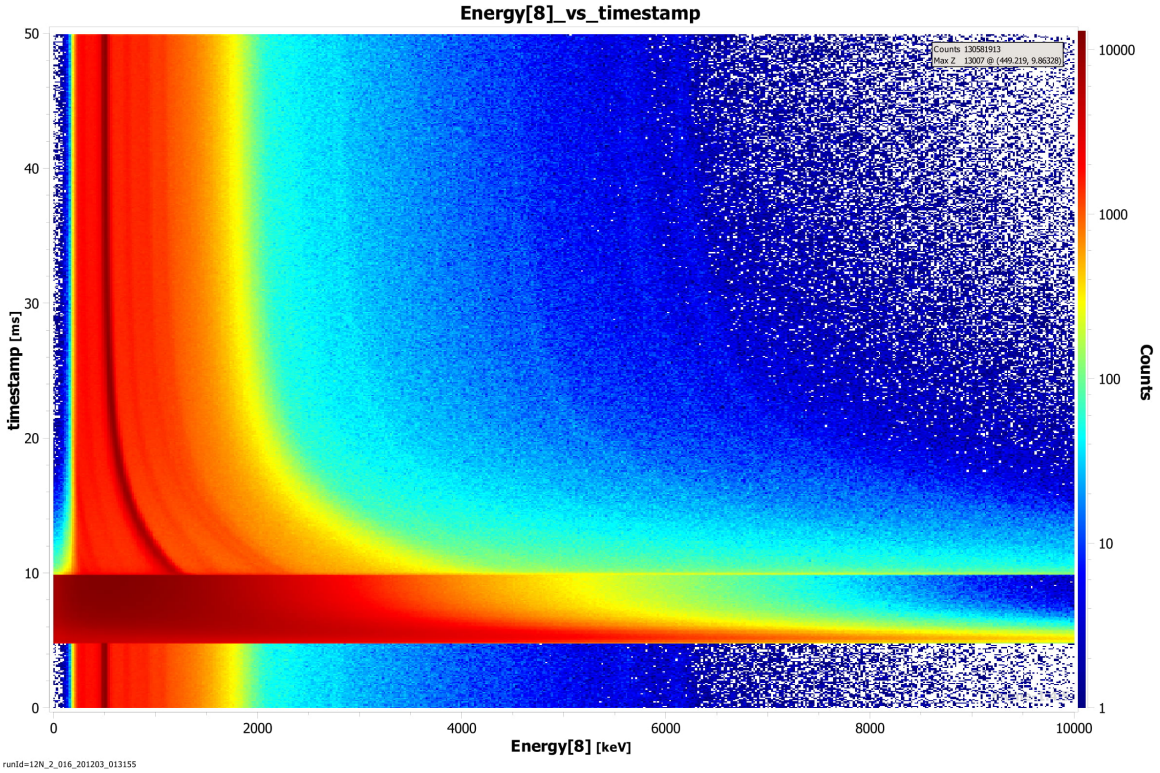

Figure 5.8: The energy-timestamp matrix before applying the time-dependent calibration.

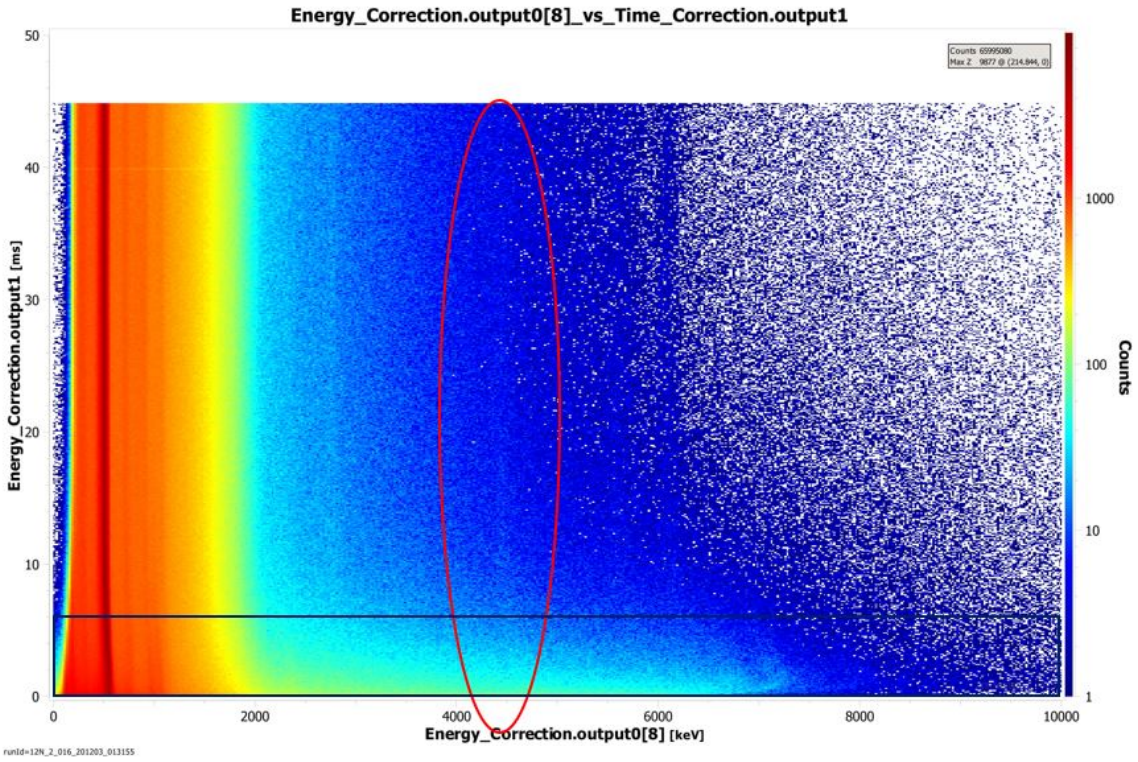

Figure 5.9: The energy-timestamp matrix after applying the energy correction. The red oval indicates the suspected photopeak of 4.4 MeV which disappears halfway in the time domain of the 45 ms. The black square indicates the 6 ms which are skipped over in the blue gamma spectrum of 5.10.

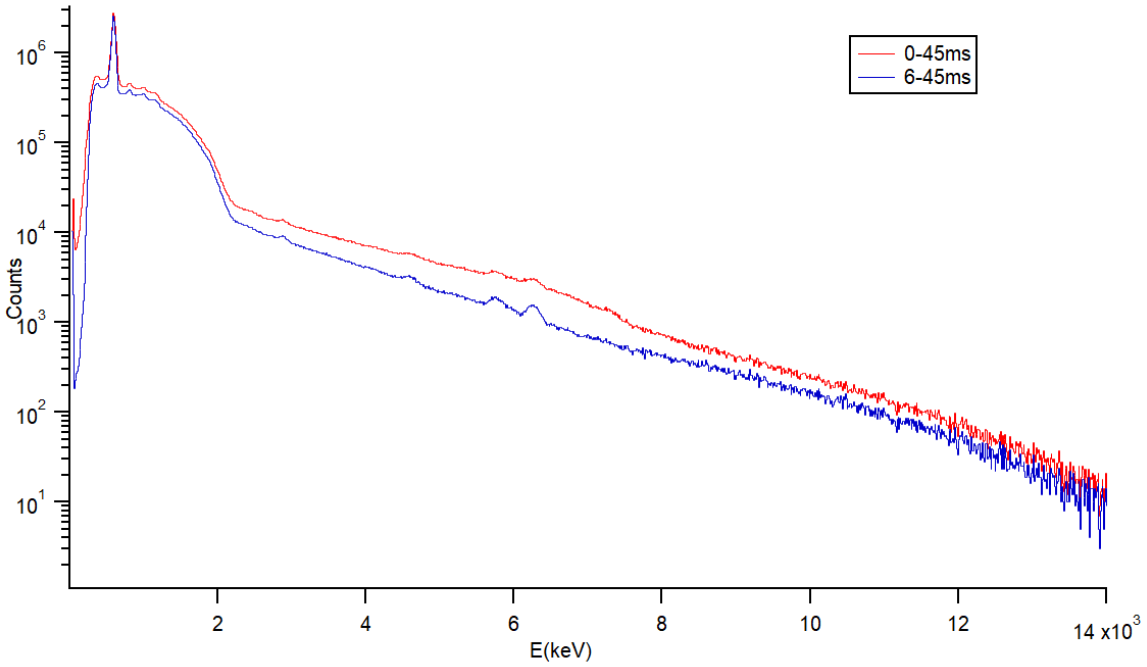

Figure 5.10: The gamma spectra of the discussed irradiation take after the energy correction. The red spectrum is of the entire time domain right after the proton beam is off. The blue spectrum skips the first 6 ms after the beam is off. Skipping the first 6 ms after radiation results in less counts, but significantly larger peak-to-background ratio for photopeaks.

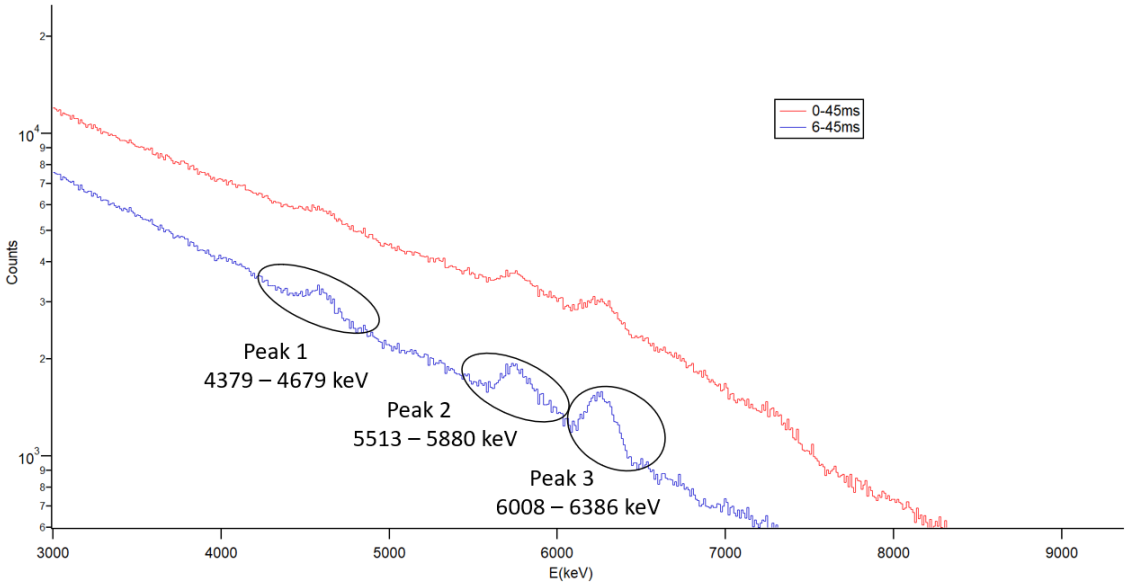

Figure 5.11: Gamma spectrum of 5.10 zoomed in with the three peaks labelled.

5.2.2 Timestamp spectra

Timestamp spectra are made from these three peaks. The amount of counts within these three energy domains over time is noted and multiple fits are applied upon them. See 5.12 for the three time spectra of the three peaks. These fits are a single exponential,

$$N = y_0 + Ae^{-\frac{t}{\tau}} \tag{5.3}$$

a double exponential

$$N = y_0 + A_1 e^{-\frac{t}{\tau_1}} + A_2 e^{-\frac{t}{\tau_2}} \tag{5.4}$$

and a double exponential with one exponential fixed to the half-life of ^{12}N, denoted as a fixed double exponential fit.

$$N = y_0 + A_1 e^{-\frac{t}{\tau_1}} + A_2 e^{-\frac{\ln 2}{11\text{ms}}t} \tag{5.5}$$

First these three fits are applied on a time domain from 0.59 ms to 45 ms. This is to avoid the extreme counts at the end of the beam-on period. See 5.13, 5.14 and 5.15 for the results of the three fits. The same fits are applied on a time domain from 6 ms to 45 ms as 6 ms was the recovery period after the energy correction. This results in fits 5.16, 5.17 and 5.18. The resulting values for half-life for each fit together with the χ^2 per measurement point-ratio of each fit is summarised in 5.3. Error weighting is taken into account when applying the fits. The resulting half-lifes and χ^2-points ratio for each fit are summarised in table 5.3.

Noticeable at first glance is that the χ^2 for the single exponential fits are relatively high, making a single exponential a significantly bad fit to describe the decay of the three peaks. Second noticeable results is the change in χ^2-point ratio between a double exponential fit and a fixed double exponential fit. For the time domain from 0.59 ms to 45 ms, the change in χ^2-point ratio when imposing a half-life of 11 ms on the double exponential fit is 2% for peak 1, 7% for peak 2 and 3% for peak 3. As peak 2 is highly likely the single escape peak of peak 3, so it has the same time evolution. Therefore, the combination of the increase in χ^2 after fixing the half-life to 11 ms for both peaks is significantly higher than the increase in χ^2 for peak 1. So of the three peaks, peak 1 is the most likely to have a half-life of 11 ms.

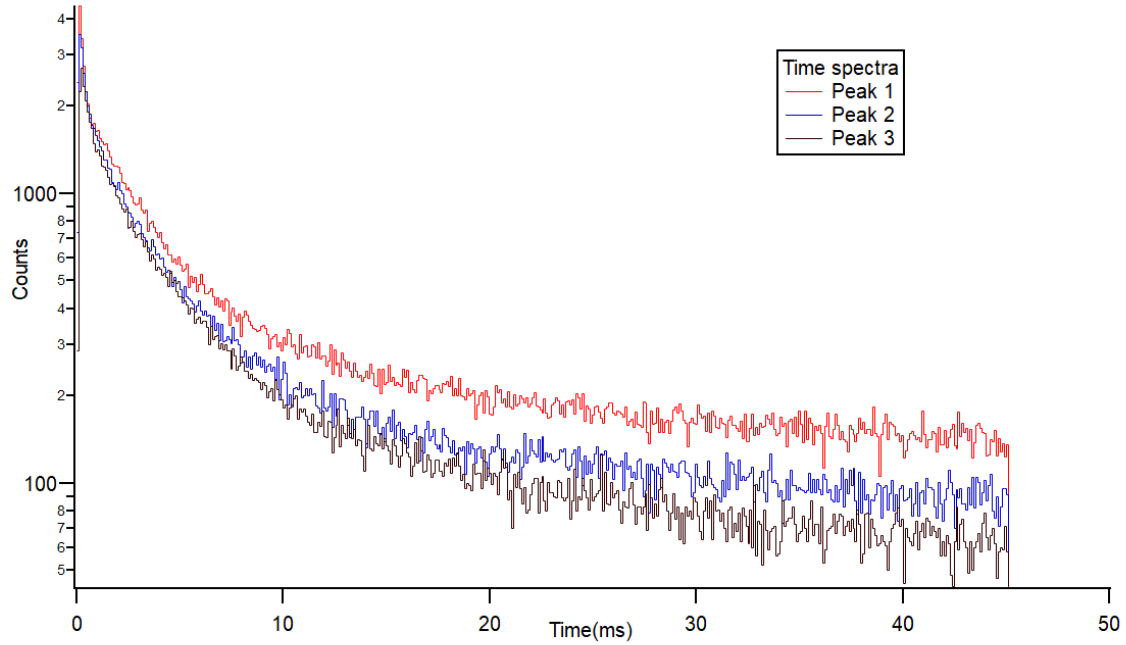

Figure 5.12: The time spectra of peak 1, peak 2 and peak 3. In this and the following graphs, the three spectra show the amount of counts between the defined energy domains of the three peaks over time.

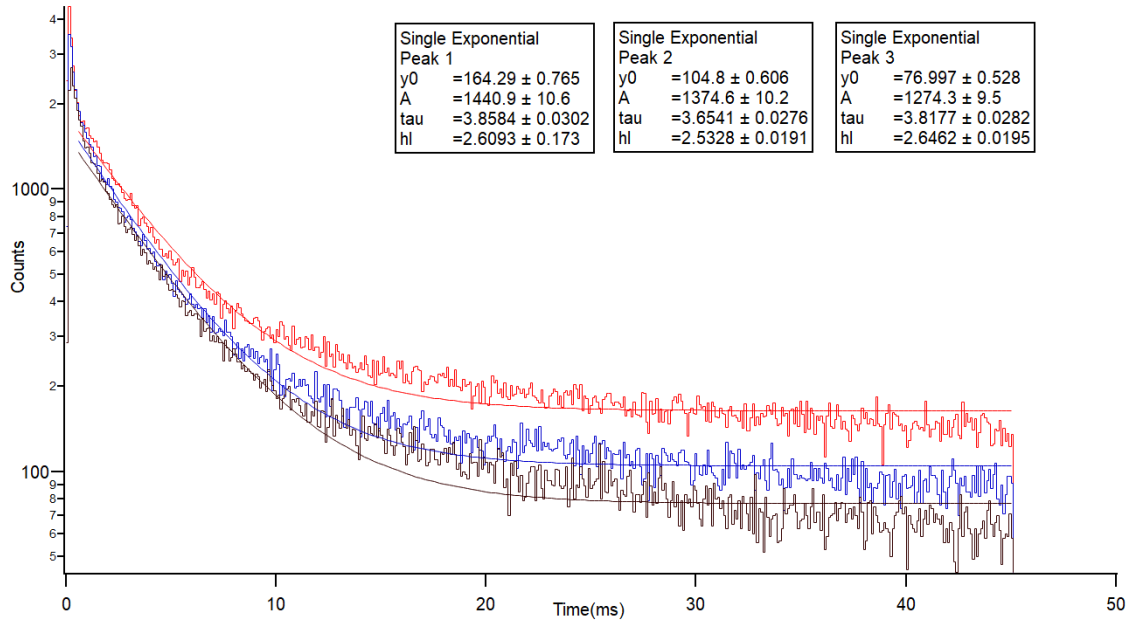

Figure 5.13: Time spectra of three peaks with a single exponential fit applied on them. Fitted time domain 0.59 ms to 45 ms.

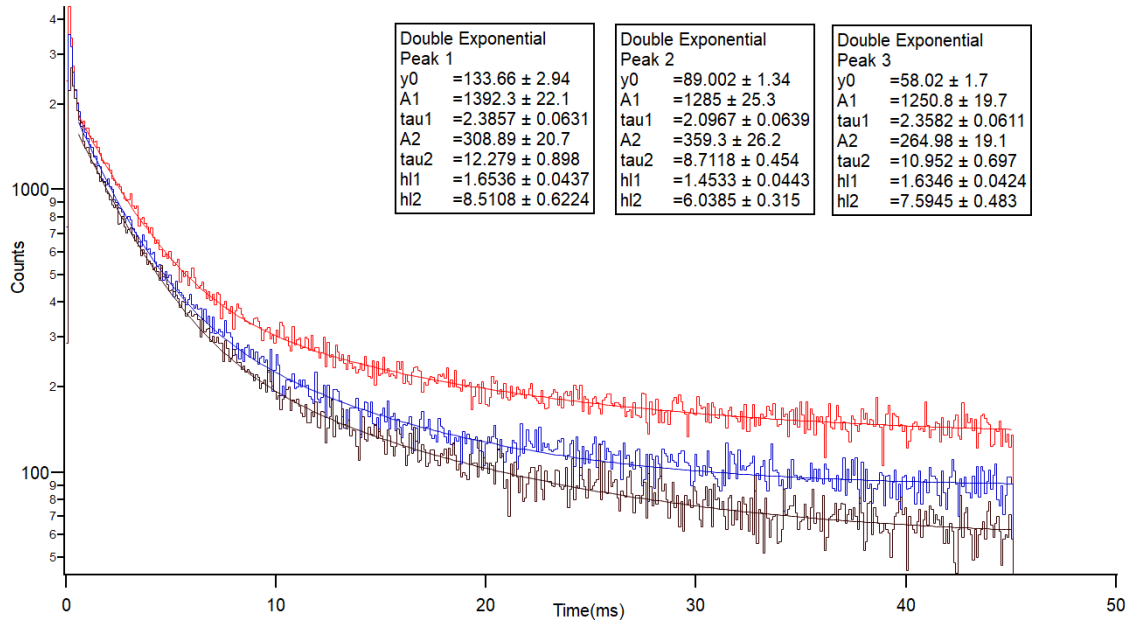

Figure 5.14: Time spectra of three peaks with a double exponential fit applied on them. Fitted time domain 0.59 ms to 45 ms.

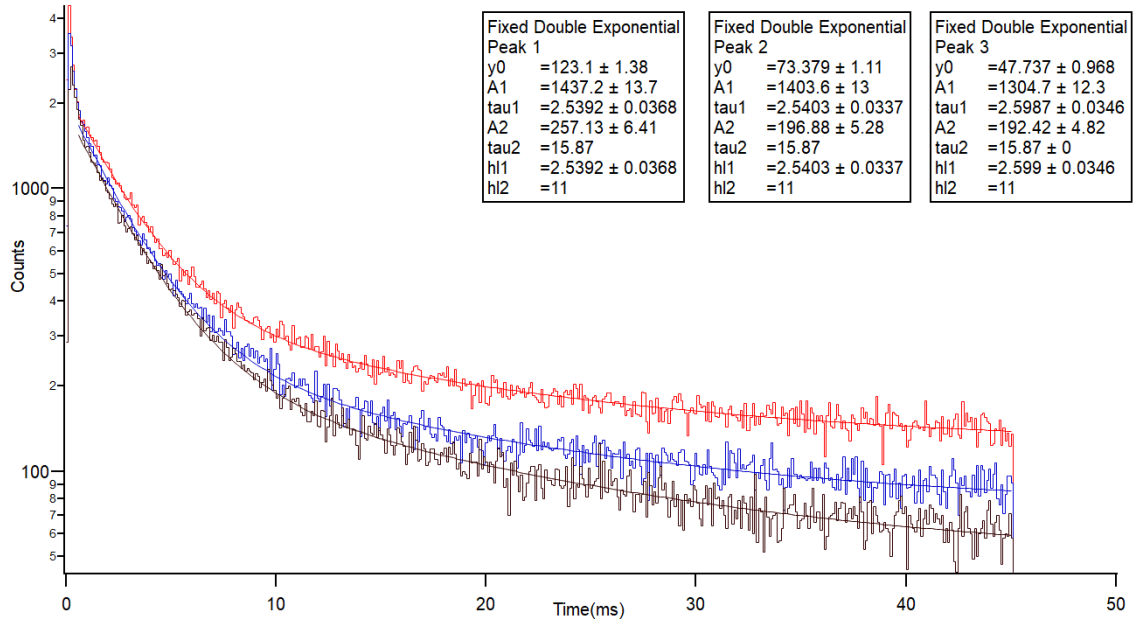

Figure 5.15: Time spectra of three peaks with a double exponential fit applied on them, whereby one exponential is fixed to the half-life of ^{12}N. Fitted time domain 0.59 ms to 45 ms.

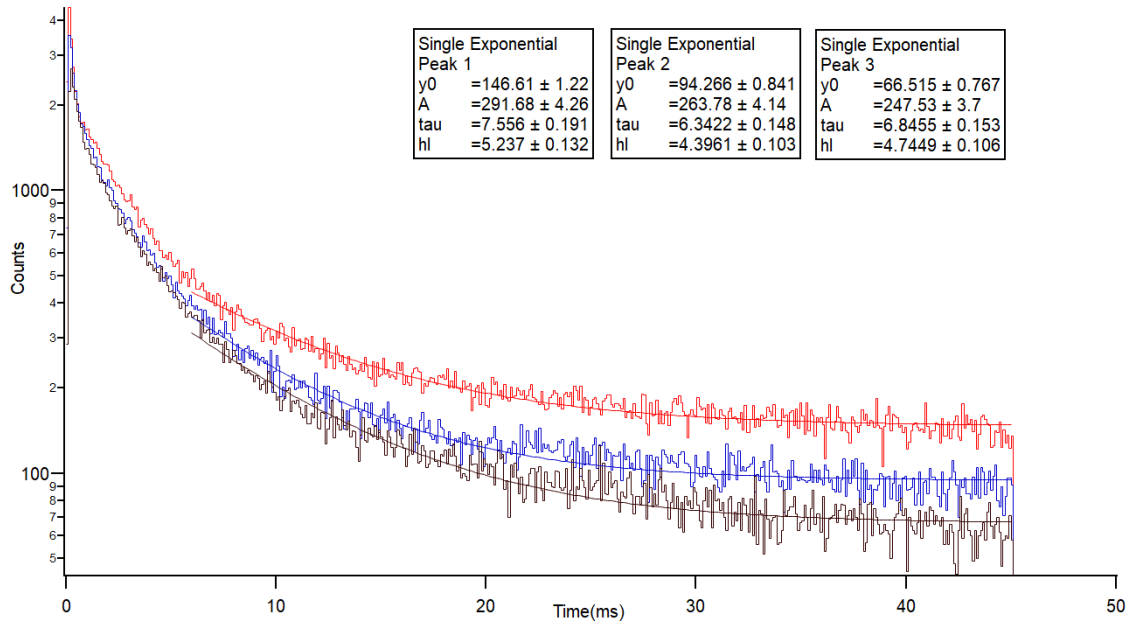

Figure 5.16: Time spectra of three peaks with a single exponential fit applied on them. Fitted time domain 6 ms to 45 ms.

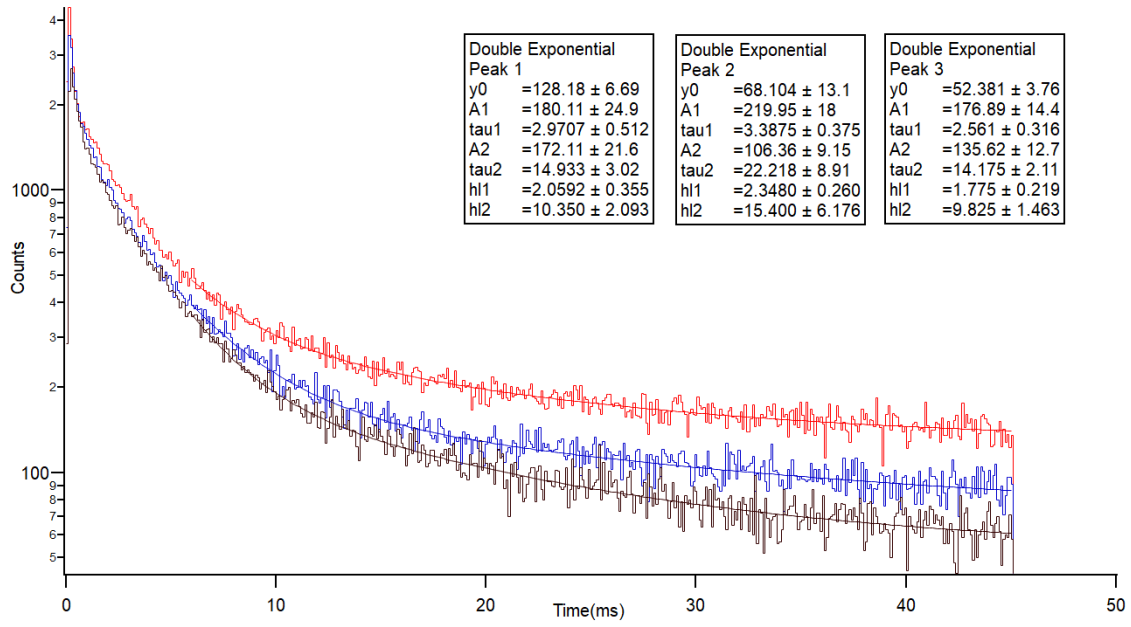

Figure 5.17: Time spectra of three peaks with a double exponential fit applied on them. Fitted time domain 6 ms to 45 ms.

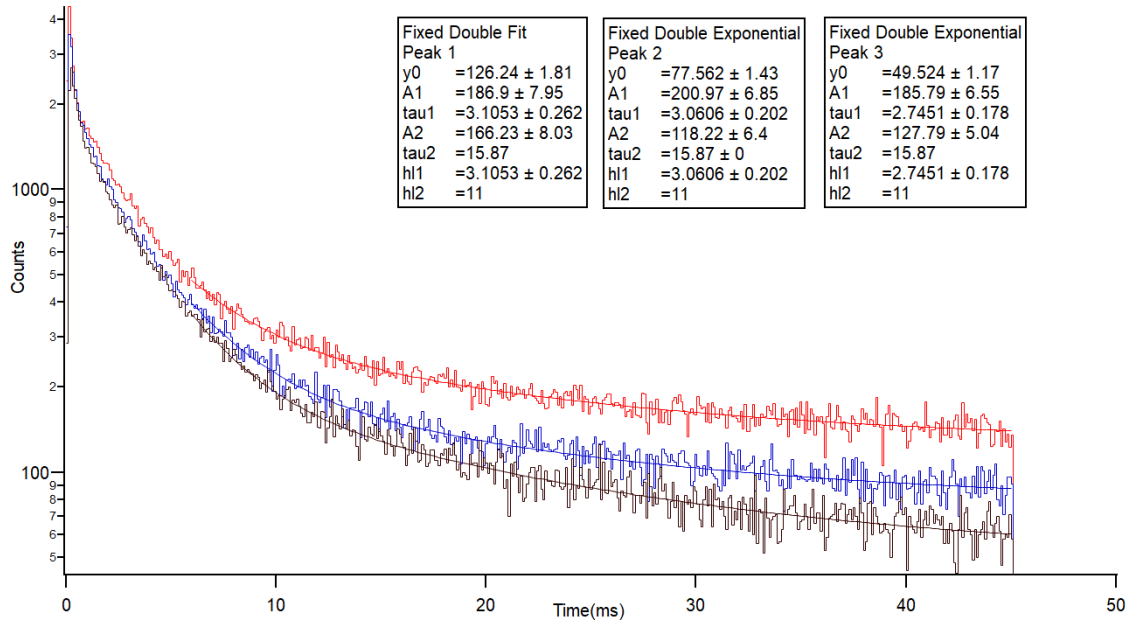

Figure 5.18: Time spectra of three peaks with a double exponential fit applied on them, whereby one exponential is fixed to the half-life of ^{12}N. Fitted time domain 6 ms to 45 ms.

Table 5.3: Fitted half-lives for each fit applied on each peak along with corresponding χ^2-point ratio. Time domains 0.59-45 ms and 6-45 ms.

peak single fit	half-life(ms) 0.59-45 ms	error	χ^2-point ratio	half-life(ms) 6-45 ms	error	χ^2-point ratio
1	2.674	0.021	3.78	5.24	0.13	1.21
2	2.533	0.019	3.73	4.40	0.10	1.34
3	2.646	0.020	4.00	4.74	0.11	1.43
double fit						
1	1.65	0.04	1.00	2.1	0.4	1.01
1	8.5	0.6		10.4	2.1	
2	1.45	0.04	1.17	2.35	0.26	0.93
2	6.0	0.3		15	6	
3	1.63	0.04	1.17	1.78	0.22	0.92
3	7.6	0.5		9.8	1.5	
fixed double						
1	1.760	0.026	1.02	2.15	0.18	0.88
2	1.761	0.023	1.26	2.12	0.14	0.93
3	1.801	0.024	1.21	1.90	0.12	0.93

5.2.3 Further discussion

During one irradiation take in the same situation as just described, the graphite target dropped by accident during beam time. This has resulted in an irradiation take where the proton beam was on, but there was no graphite target being irradiated. The gamma spectrum, similarly modified as in 5.2.1, shows peak 2 and peak 3, but no peak 1. This shows that peak 1 is from the graphite target. See 5.19 and 5.20 for a comparison between the gamma spectra with and without a graphite target. This gives rise to two questions about the source of peak 1 and the source of peak 2 and peak 3. To summarise, peak 1 has the following properties:

- 4.4 MeV is inside its energy domain.
- A double exponential fit with one exponential fixed to a half-life of 11 ms seems to fit well up on its decay over time as shown in table 5.3.
- Its source is from the graphite target as the peak is absent in the irradiation take where the graphite target dropped.

These properties strongly indicate the production of ^{12}N occurred during irradiation. However, peak 2 and peak 3 also have indication that they have a half-life component of about 2 ms and a half-life component which is four to five times larger. There is a possibility that the three peaks have the same source which causes the smaller and the larger components. Thermal neutrons, originating from high-energy neutrons produced by the proton beam which are later thermalised by the surrounding concrete, are suspected to be the source of all three peaks. In an attempt to reject the notion of the three peaks having the same source, each time spectra is fitted with a single and a double exponential fit in the time domain from 12 ms to 45 ms. The resulting fitted half lives are listed in table 5.4. If the 2 ms half-life component is true, then after 12 ms, this component will have decayed to $\frac{1}{2}^{\frac{12}{2}} = 1.6\%$ of its starting activity. The longer-lived component will have lost about half of its starting activity. The desired result would be that the emerging half-life from a single fit of peak 1 is significantly different from the half-lifes of peak 2 and peak 3. This would mean that peak 1 does not

have the same source as peak 2 and peak 3. A half-life of 11 ms would emerge from a single exponential fit upon peak 1 preferably. However, table 5.4 shows that the half lives from a single exponential fit has similar values for each peak and neither value has 11 ms within their error margin. The large error at the double fit gives reason to conclude that a double exponential fit is unsuitable for a fit on this time domain.

Furthermore, a time spectrum of peak 1 in anti-coincidence with the BGO is created. This is the same time spectrum of peak 1 as before, but the measurement events which occur in both the NaI-detector and the BGO-detector are omitted. The idea behind this is that peak 2 and peak 3 are suspected to be caused by the neutron activation of the oxygen, O, in the BGO-detector. The three fits are repeated on this peak 1 with the selected time domain being 0.59 ms-45 ms. A single exponential fit is also repeated for time domain 12 ms-45 ms. The resulting fitted half lives, listed in table 5.5, show similar results to previous fitted half lives found in tables 5.3 and 5.4. The χ^2-point ratio improves by 0.01 when a half-life of 11 ms is imposed compared to the double exponential fit.

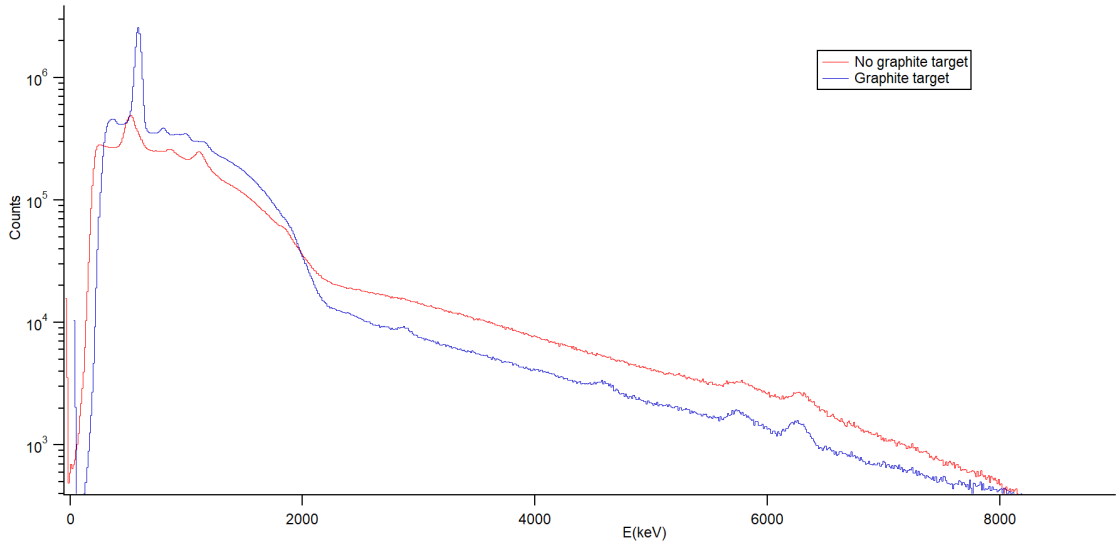

Figure 5.19: Gamma spectra of the irradiation takes with and without the graphite target. Time domain 6 ms-45 ms.

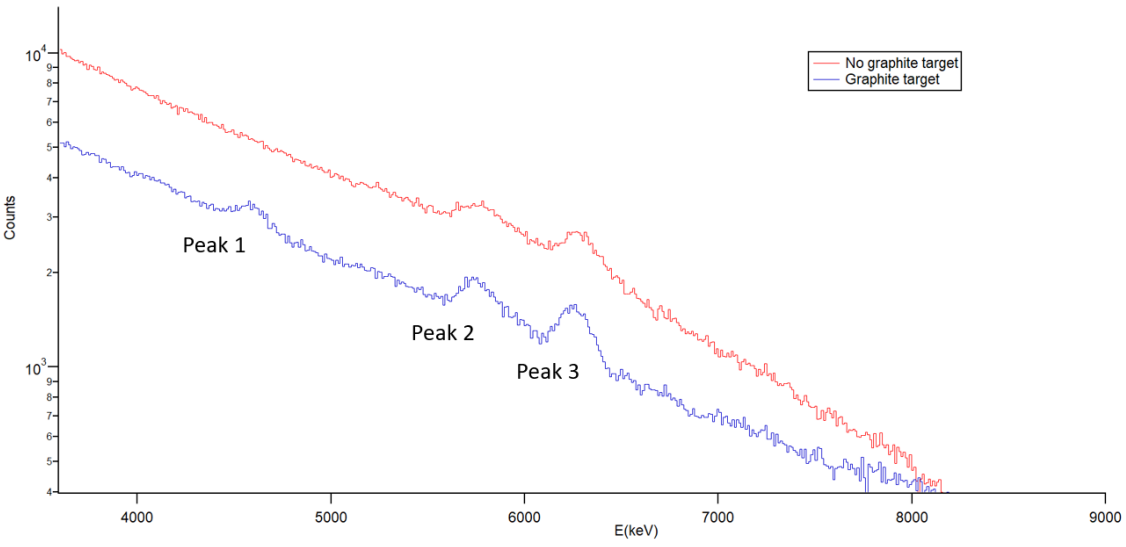

Figure 5.20: The two gamma spectra zoomed in at the three peaks. Peak 2 and peak 3 are present in the spectrum without graphite, but peak 1 is absent, indicating that peak 1 is from the graphite target.

Table 5.4: Fitted half-lives for each fit applied on each peak along with corresponding χ^2-point ratio, similair to 5.3. Time domain 12-45 ms.

peak single fit	half-life(ms)	error	χ^2-point ratio
1	8.3	0.6	1.01
2	7.9	0.6	1.06
3	8.0	0.5	1.13
double fit			
1	6	21	1.00
1	14	120	
2	1.6	1.6	1.03
2	12	8	
3	4	7	1.13
3	11	16	

Table 5.5: Half-lives of the three fits upon peak 1 whereby the measurement events are in anti-coincidence with the BGO-detector. The fits are performed on the time domain from 0.59 ms to 45 ms. The single exponential fit is repeated for the time domain 12-45 ms.

peak 1 single	half-life(ms)	error	χ^2-point ratio
	4.40	0.07	1.16
double fit			
	2.04 8.3	0.17 0.9	1.10
fixed double			
	2.25	0.09	1.09
single 12 ms- 45ms	8.3	0.7	1.10

5.3 Neutron activation

In experiment session 2, it is found that the proton beam produced a neutron gas. This neutron gas activated various materials surrounding the experimental setup, including the NaI-scintillator in the detector. The activation of the detector itself causes the detector to measure its own radiation, significantly increasing the measured background radiation. After the series of proton radiation experiments, the detector is removed from the radiation room. The detector is set to measure its own radiation for a period of 48 hours. The sodium in the NaI-scintillator consists of the only stable sodium isotope ^{23}Na. The presence of a neutron gas can induce neutron capture, producing ^{24}Na. ^{24}Na has a half-life time of very near 15 hours and decays by emitting a β^- and two gammas of 1368.626 keV and 2754.007 keV.[15]. Two analyses were performed in an attempt to fit the half-life time of 15 hours and therefore to confirm the presence of ^{24}Na.

5.3.1 2754 keV peak analysis

The collection of spectrum data is split up into time domains of half an hour. Each half hour is assigned a timestamp counting from the start of the measurement. For each half hour, a spectrum is plotted whereby a 2574 keV peak that decreases over time becomes apparent. See figure 5.21 for some of these half hour spectra. An attempt is made to see if these peaks corresponded with a half-life of 15 hours by counting the peak intensity. The determination of the peak intensities is performed by taking a linear fit between the ends of the peak and summing up all the counts above this line. A Gaussian fit proofs difficult due to asymmetry in the peaks and a not clear Gaussian behaviour for the peaks later in time. The peak intensity is determined for 33 spectra spanning 48 hours with a time break of about 20 hours. Three fits are applied to this result: a single exponential fit, a double exponential fit and a double exponential fit whereby the half-life of one of the exponentials is fixed to 15 hours. The resulting parameters of those fits are given by table 5.6. Graphs 5.22, 5.23 and 5.24 show the three different fits. An immediate result is that the double exponential fit can be discarded due its large relative error. Therefore there is no evidence for the presence

of two half-lives.

5.3.2 Energy binning

The collection of data is split up in time domains of two hours. This results in 13 spectra in time domains from hour 0 to hour 46 with a gap of 24 hour between hour 8 and hour 32. For each two-hour spectrum, the amount of counts between energy 1-2 Mev, 2-3 MeV, 3-4 MeV, 4-5 MeV and 5-6 MeV are noted. The analyses is performed for both the NaI-detector and the BGO-detector. However, the last domain of 5-6 MeV is omitted for the BGO-detector, as it contains very few counts. Graphs 5.25 and 5.26 respectively show the results for the NaI-detector and BGO-detector. An single exponential fit on the counts in domain 2-3 MeV, where the peak of 2754 keV resides, results in a fit of a half-life of 14.6±0.4 hours. This is in agreement with the half-life of ^{24}Na. See graph 5.27.

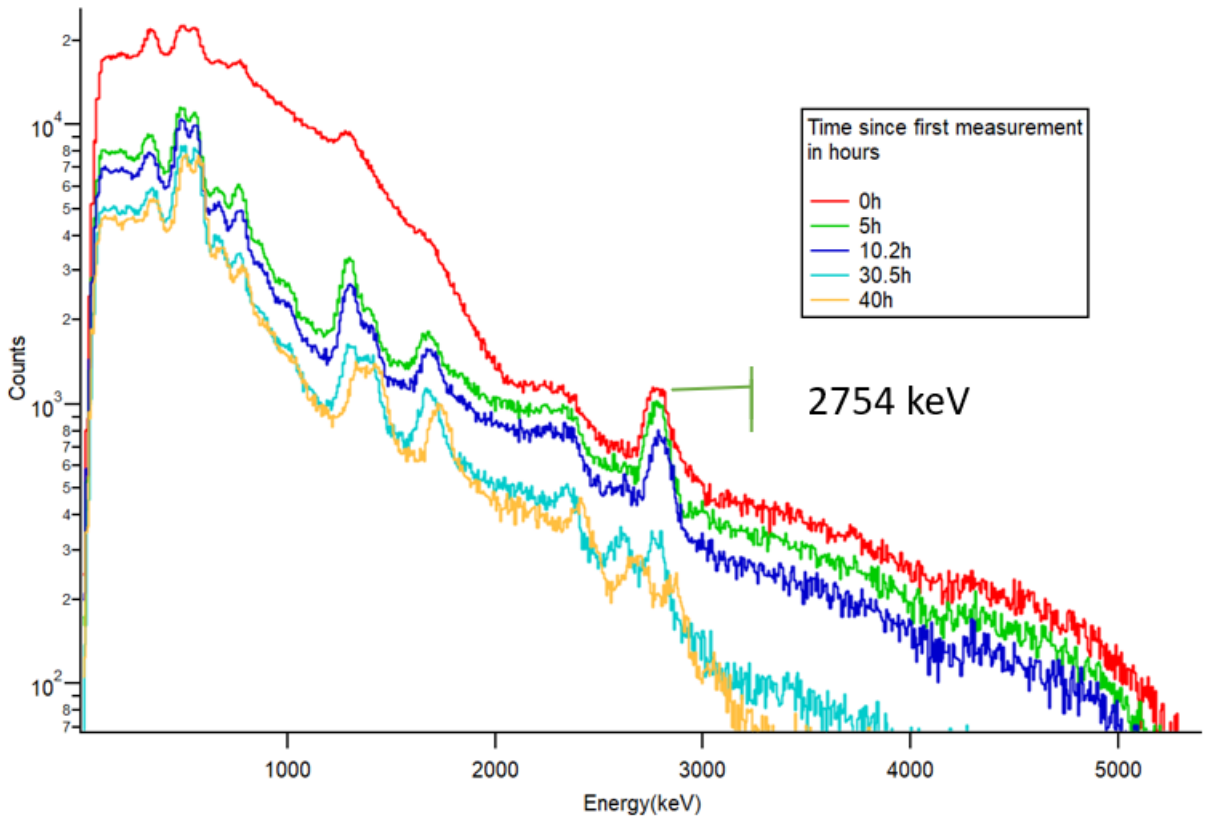

Figure 5.21: Gamma spectra of the NaI-detector measuring itself over time. The decay of the intensity peak at 2754 keV corresponds with the 15 hour half-life of 24Na-decay.

Table 5.6: The parameters acquired by fitting a single exponential, double exponential and double exponential with one fixed to a half-life of 15 hours upon the peak intensities of at 2754 keV. The offset is noted as y_0 and the starting value as A in the three fit equations 5.3, 5.4 and 5.5.

Single exponential fitted parameters	values parameters from fit	error
offset	-1.9E+02	1.3E+02
starting value	1.15E+04	1.1E+02
inverse decay constant	1.95E+01	8E-01
half-life(hours)	1.35E+01	6E-01
Double exponential fit		
offset	-2E+02	4.23E+03
starting value exponent 1	1E+04	14E+09
inverse decay constant 1	2E+01	4E+04
starting value exponent 2	2E+03	1.4E+09
inverse decay constant 2	2E+01	1.9E+05
half-life 1(hours)	1E+01	2.5E+04
half-life 2(hours)	1E+01	1.3E+05
Double exponential fit, fixed second exp.		
offset	-3E+02	5E+02
starting value exponent 1	7E+03	1.9E+04
inverse decay constant 1	1.6E+01	1.1E+01
starting value exponent 2	4E+03	2.0E+04
inverse decay constant 2	21.6E+01	
half-life 1(hours)	11.1	8
half-life 2(hours)	15	

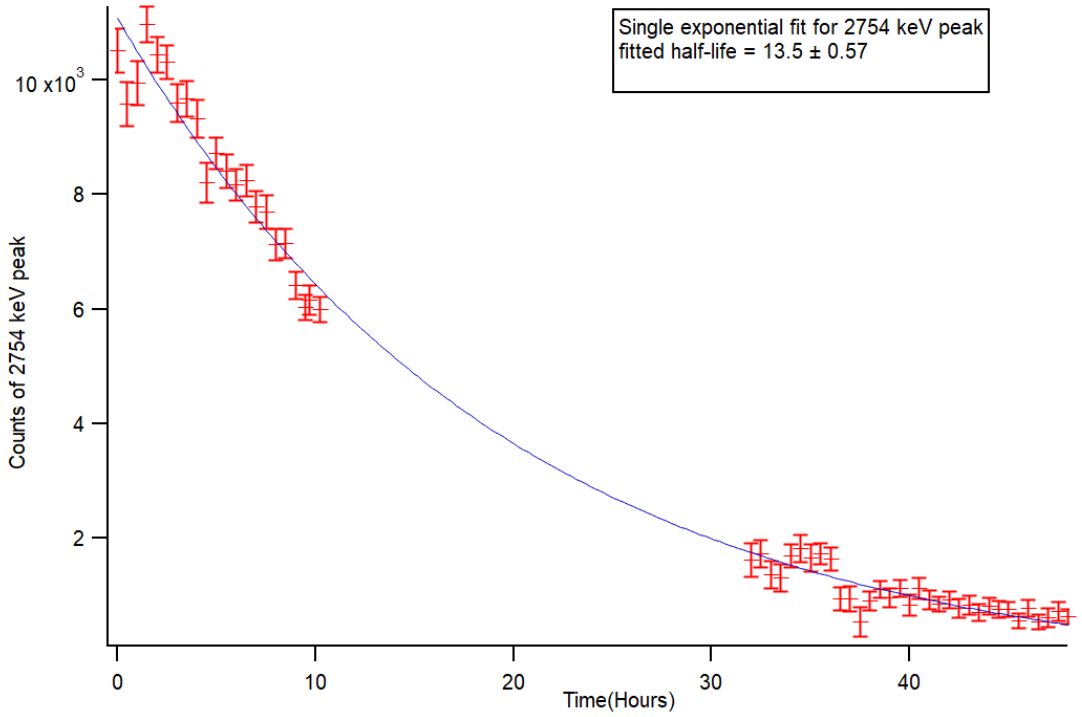

Figure 5.22: The counts in the peaks at 2754 keV versus time in hours with fitted single exponential function. Fitted half-life given in hours.

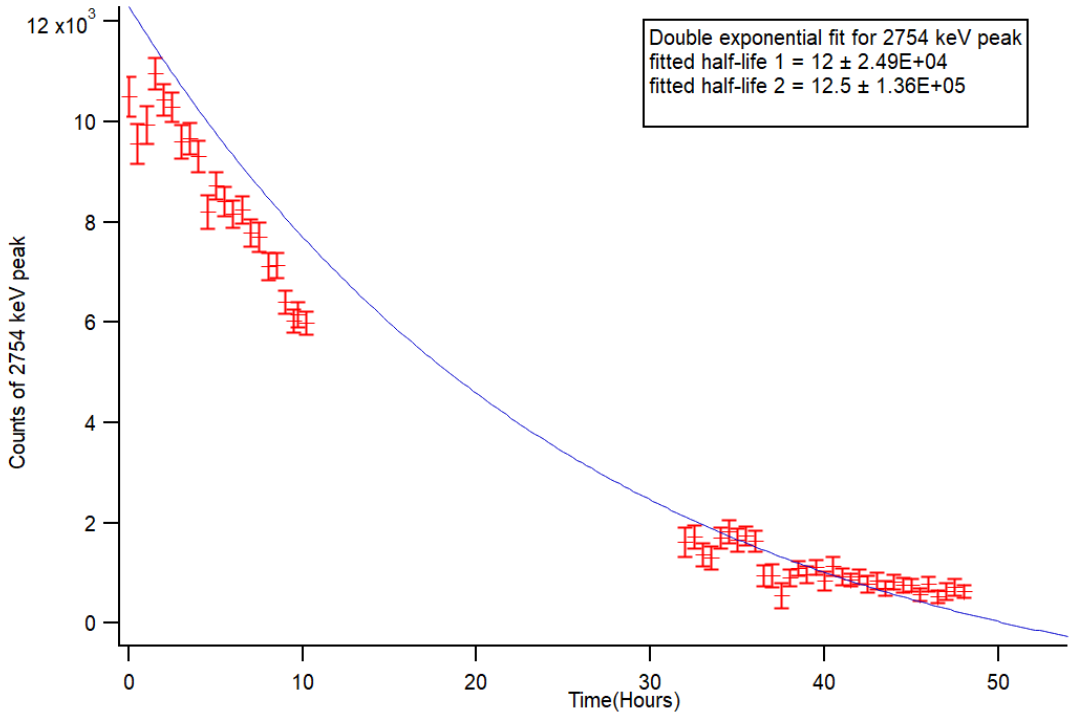

Figure 5.23: The counts in the peaks at 2754 keV versus time in hours with a double exponential fit. Fitted half-life given in hours.

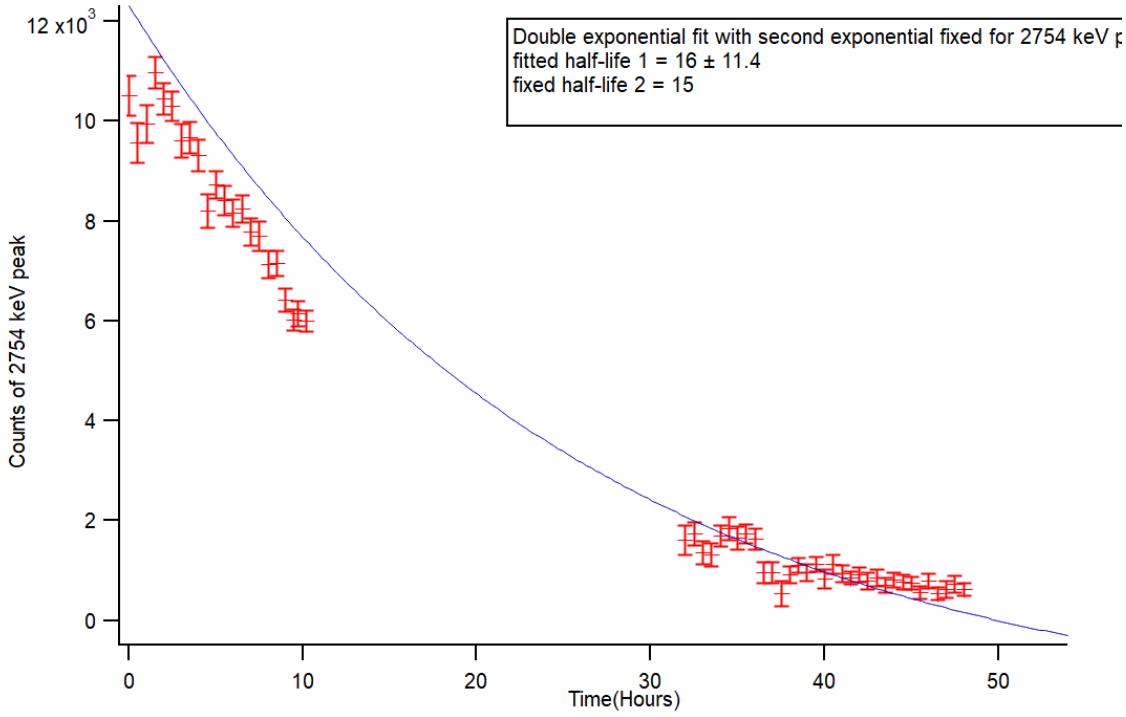

Figure 5.24: Graph of the counts in the peaks at 2754 keV versus time in hours with a double exponential fit whereby the half-life of the second exponential is fixed to 15 hours. Fitted half-life given in hours.

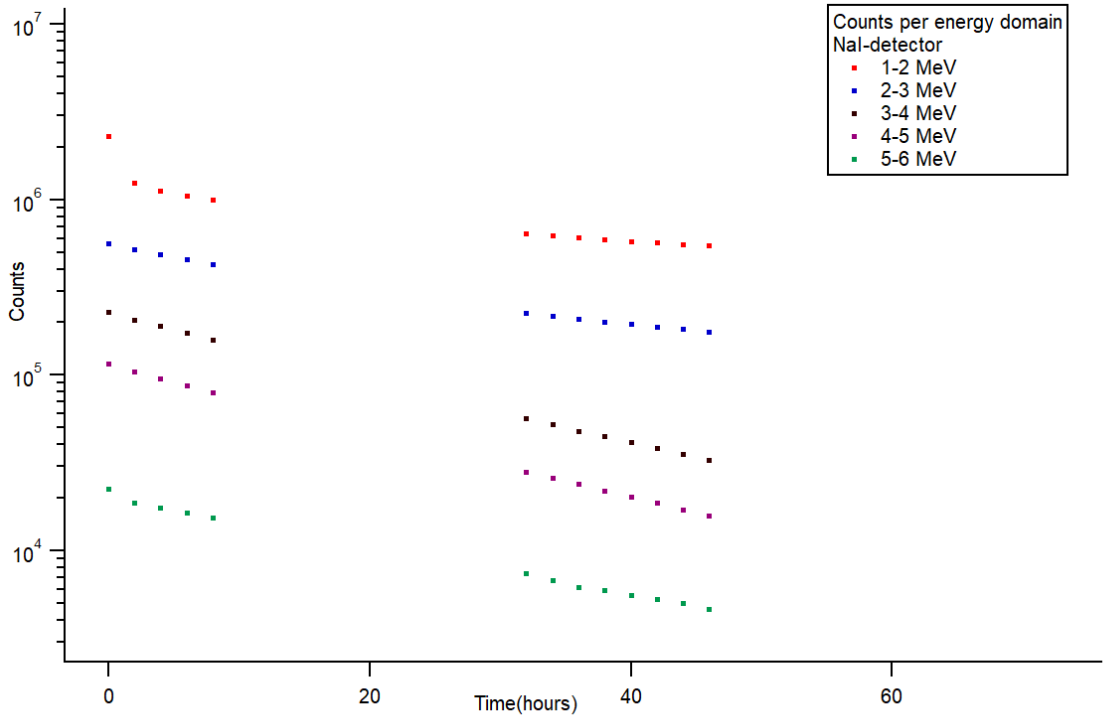

Figure 5.25: Graph of the amount of counts over time per 1 MeV bin of the NaI-detector.

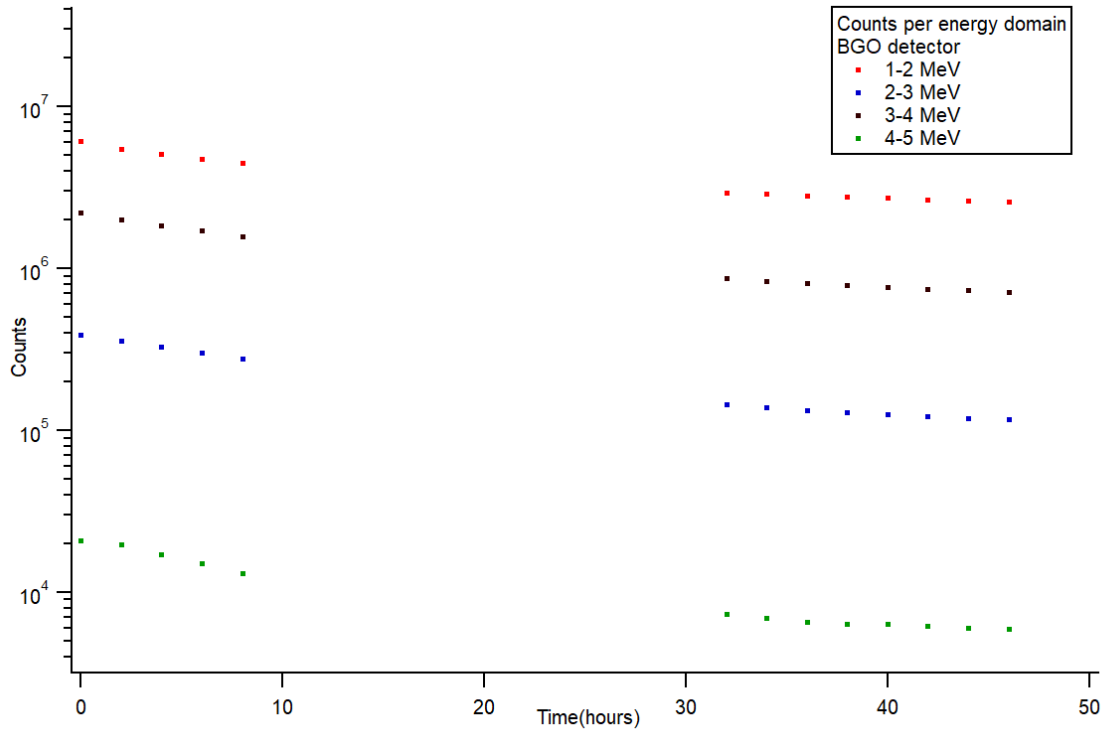

Figure 5.26: Graph of the amount of counts over time per 1 MeV bin of the BGO-detector.

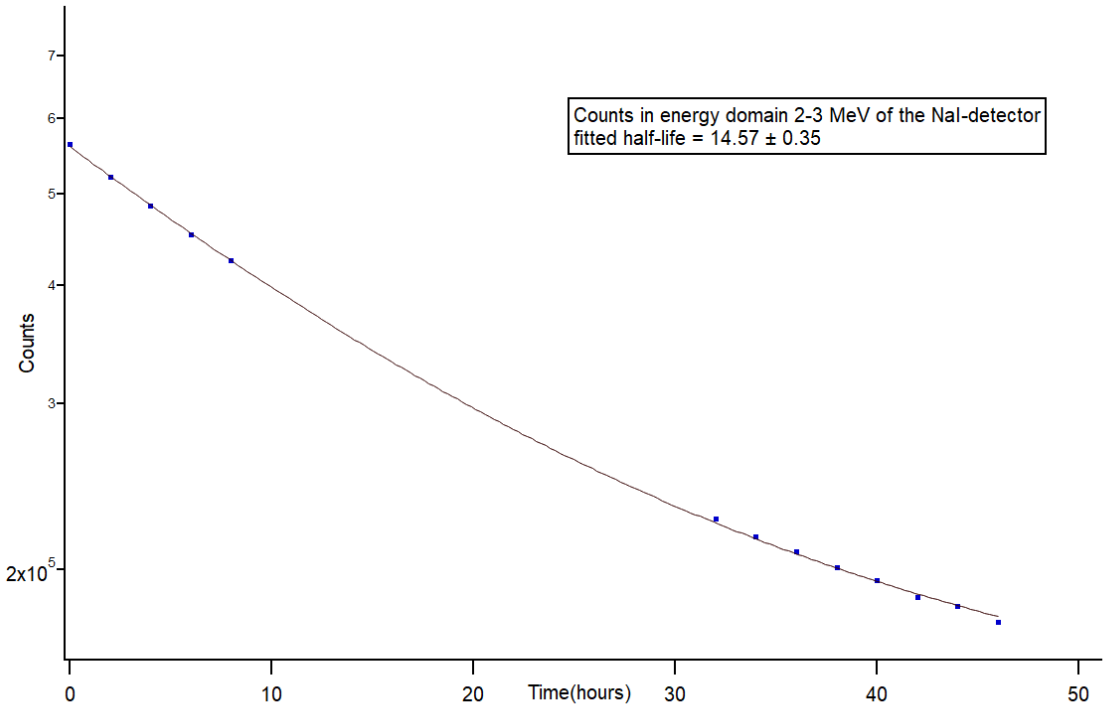

Figure 5.27: Single exponential fit over the 2-3 MeV energy domain counts of the NaI-detector. The fitted half-life is 14.6±0.4 hours.

Chapter 6

Discussion

6.1 Comparison detected and predicted ^{12}N

The detected amount of 4.4 MeV gammas originating from the decay of ^{12}N is compared to its predicted amount. The prediction follows the step as described in 3.4. The predicted amount of produced ^{12}N is calculated and from that a prediction for the amount of measured 4.4 MeV gammas is calculated using equation 3.27. For the measured amount of 4.4 MeV gammas, peak 1 from the results is assumed to come from the decay of ^{12}N, although this is not entirely confirmed. The measured amount of 4.4 MeV gammas is obtained by determining the intensity of peak 1. The parameters used and the results thereof are listed in table 6.1. The measured amount of 4.4 MeV gammas is 3.5 times larger than comes out of the prediction. It is possible that the estimated cross section of the production of ^{12}N on graphite from the extrapolation of the paper by Rimmer & Fisher[12] is not correct. The cross section at the higher proton energy of 90 MeV is still unknown, as the determination of this cross section at the higher energy was the original goal of this thesis.

Table 6.1: Parameters and results for the predicted and measured amount of 4.4 MeV gammas.

Proton count	9.69E+12
Total 12N produced	1.30E+08

Detector effiency	0.001
beam time	5 ms
recovery time	6 ms
measurement time	39 ms

Prediction measured 4.4 MeV gammas	1.32E+03
Measured 4.4 MeV gammas of peak 1	4.6E+03

6.2 Recommendations for future experiments

Improvements for the next experimental session to confirm the production of ^{12}N are already planned. However, due to technical difficulties regarding the cyclotron, a third session with improvements could not be performed within the time span of this thesis. These improvements can be summarised as:

- Implementing pulsed PMT.
- Covering the detector with cadmium.
- Omitting the BGO-detector.

Pulsed PMT

One of the main problems regarding the measurement of ^{12}N in the performed sessions is that the NaI-detector has to recover from oversaturation which happens when the proton beam is on. During the recovery of the detector, a large amount of ^{12}N has then already decayed. Data manipulation through an energy correction provides a makeshift solution to this, but a pulsed PMT could ensure a more proper measurement of the graphite right after the proton beam is turned off within a beam time cycle. Pulsing the PMT means turning off the PMT when the proton beam is on such that the detector will stop measuring while

the proton beam is active. When the proton beam is off within a beam time cycle, the PMT is actived again. The pulsing of the PMT is done by connecting the PMT with a voltage source. This voltage source is synchronised with the same pulse generator that controls the beam time cycle. This synchronisation is such that, when the proton beam is on, the PMT switches from its regular voltage source to second voltage source. When the beam is off, the PMT switches back. This second voltage source provides the photocathode of the PMT with a voltage of -5 V with respect to the first dynode. The negative voltage blocks the photoelectrons from escaping the cathode. This stops the NaI-detector from measuring during the time the beam is on and also clears the PMT from lingering electrons clouds inside. If the PMT would be turned off instead of switching to a second voltage, then the lingering electrons would disrupt the first instance of measurement right after the PMT is turned back on again. A different NaI-detector is obtained for this purpose, as the NaI-detector used for the performed measurements cannot be connected to such a voltage source as required. See 6.2 and 6.1 for pictures of this NaI-detector and voltage source.

Cadmium covering

As shown in 5.3, the NaI-detector becomes activated by thermal neutrons when the beam is on. The activation of the detector adds significant background counts which frustrate measurements. The half-life of ^{24}Na which is suspected to be produced by thermal neutrons in the NaI-detector is 15 hours. The 15 hour half-life ensures that it takes about three days for ^{24}Na to have decayed below 10% of its original amount. To prevent as much activation of the NaI-detector as possible by thermal neutrons, the detector is covered by cadmium. Cadmium has a large cross section for thermal neutron capture, therefore the cadmium covering would shield the detector from thermal neutrons, preventing activation.[21]

Omitting the BGO-detector

The purpose of the BGO-detector is to measure Compton-scattered gammas and filter out their measurement events. However, it is sus-

pected that the BGO-detector also becomes actived by thermal neutrons. Due to the BGO-detector's large and inconvenient shape, providing it with shielding is problematic. Therefore, the BGO-detector is omitted for future experiments. This would mean that measurement events from Compton-scattering will enter the data, but this is offset by the lack from measurement events from activated material surrounding the NaI-detector.

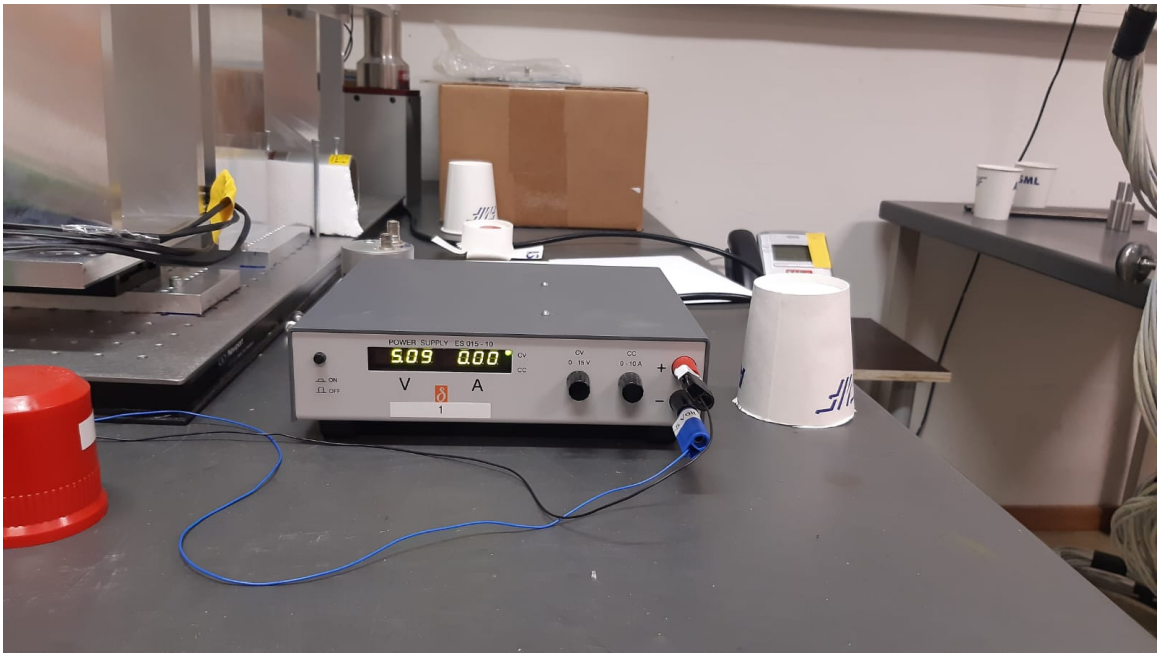

Figure 6.1: The voltage source connected to the PMT to which the PMT switches to when the beam is on.

Figure 6.2: The NaI-detector whose PMT can be pulsed by being connected to a pulsed voltage source. This NaI-detector will replace the NaI-detector used in this thesis in future sessions.

Chapter 7

Conclusion & Outlook

Evidence has been found that 4.4 MeV gammas from the decay of ^{12}N can be detected. This detection was during the second experimental session whereby the 5.2 mm thick graphite slab was irradiated with 90 MeV protons. A photopeak, peak 1 in the results, appears after data manipulation at the correct energy domain of around 4.4 MeV with an intensity that is close to prediction. The results also show that a half-life of 11 ms fits upon the timespectrum of the photopeak with a χ^2-point ratio close to 1. The irradiation take without the presence of the graphite target also shows that this peak originates from the graphite target. However, it is not fully established that the cause of this peak is due to the decay of ^{12}N and not via other effects, such as neutron activation. More experiments are needed to confirm the production of ^{12}N in the graphite target. These future experiments will include the listed improvements: a pulsed PMT, a cadmium covering and the absence of the BGO-detector. The pulsed PMT will make the detector able to start properly measuring right after proton irradiation without having to recover from overload caused by the proton beam. The cadmium covering along with omitting the BGO-detector will prevent disruptive activation by thermal neutrons. If the production of ^{12}N is confirmed, the experimental setup can then be adjusted such that the original goal of determining the cross section of ^{12}N-production at high proton energy is approached.

Bibliography

[1] J.C. Polf & K. Parodi, *Imaging particle beams for cancer treatment*, 2015

[2] Harald Paganetti, *Range uncertainties in proton therapy and the roleof Monte Carlo simulations*, 2012 Phys. Med. Biol.57 R99

[3] Edited by H.Paganetti, *Proton Therapy Physics*, 2012

[4] J. Krimmera, D. Dauvergneb, J.M. Létang, É. Testa, *Prompt-gamma monitoring in hadrontherapy: A review*, 2017

[5] Xuping Zhu, Georges El Fakhri, *Proton Therapy Verification with PET Imaging*, 2012

[6] Peter Dendooven *et al*, *Short-lived positron emitters in beam-on PET imaging during proton therapy*, Physics in medicine and biology vol. 60,23 (2015): 8923-47. doi:10.1088/0031-9155/60/23/8923

[7] Sebastian P. Nischwitz *et al*, *Clinical implementation and range evaluation of in vivo PET dosimetry for particle irradiation in patients with primary glioma*, 2015

[8] Christopher Kurz *et al*, Initial clinical evaluation of PET-based ion beam therapymonitoring under consideration of organ motion, 2016

[9] Veronica Ferrero *et al*, *Online proton therapy monitoring: clinical test of a Silicon-photodetector-based in-beam PET*, 2018

[10] *https://umcgresearch.org/w/partrec*

[11] Ikechi Samuel Ozoemelam *et al*, *Feasibility of quasi-prompt PET-based range verification in protontherapy*, 2020 Phys. Med. Biol.

[12] E.M. Rimmer and P.S. Fisher, *Resonances in the (p,n) reaction on ^{12}C*, 1967

[13] Krane, *Introductory Nuclear Physics*, 1988

[14] Glenn F. Knoll, *Radiation Detection and Measurement, third edition*, 2009

[15] *https://www.nndc.bnl.gov/nudat2/decaysearchdirect.jsp?nuc=24NA&unc=nds*

[16] *https://pdg.lbl.gov/2014/AtomicNuclearProperties/HTML/carbon_graphite_C.ht*

[17] C.M. Baglina, E. Browne, E.B. Norman, G.L. Molnár, T. Belgya, Zs. Révay, F. Szelecsényi, *^{66}Ga, a standard for high-energy calibration of Ge detectors*, 2001

[18] Adrian Parveet James Sidhu, *Investigation into the Production of ^{66}Ga from Natural Zinc for the Calibration of a NaI(Tl) Scintillation Detector*, 2020

[19] *https://www.mesytec.com/*

[20] Robley Evans, *The Atomic Nucleus*, 1955

[21] Brookhaven National Laboratory, *Thermal neutron capture cross sections resonance integrals and G-factors*, 2003, *https://www.osti.gov/etdeweb/servlets/purl/20332542*